ION HEATING IN THE ION CYCLOTRON RANGE OF FREQUENCIES IN THE WISCONSIN TOKAPOLE II

BY

ALAN PARDY BIDDLE

A thesis submitted in partial fulfillment of the requirements for the degree of

DOCTOR OF PHILOSOPHY

(PHYSICS)

at the

UNIVERSITY OF WISCONSIN-MADISON

1980

ABSTRACT

ION HEATING IN THE ION CYCLOTRON RANGE OF FREQUENCIES IN THE WISCONSIN TOKAPOLE II

ALAN PARDY BIDDLE

Under the supervision of Professor J. C. Sprott

Ion temperatures of 75 eV, a doubling of the ohmic heating temperature in a normal discharge, have been achieved using the fast magnetosonic wave heating at the second, third, and fourth harmonics of the cyclotron frequency in a single component hydrogen plasma. The wave launching structure is a single turn, shielded, insulated loop which constitutes the inductor of the rf source tank circuit. Power levels of 800 kW have been applied to the plasma for periods of up to 1.1 milliseconds. Good agreement has been found between theory and experiment for loading and wave propagation in the plasma for m = 0 and m = +1 modes. Eigenmodes have been observed by peaking of both the rf wave amplitude and the loading of the oscillator, as well as by oscillator frequency shifts imposed by their passage.

Enhanced neutral density caused by poor ion confinement and edge heating resulting from the limited number of modes accessible has been observed. Significant improvement was achieved by the use of a Faraday shield over the Macor antenna insulator. The use of a self excited oscillator has resulted in a limited passive mode tracking capability with improvements in power deposition of about 40% over a constant frequency source. Plasma density increases about 20% with the application of rf with a resulting termination of the discharge approximately 10% earlier than without rf. Spectroscopic data indicates that hoop bombardment causing a 15 fold increase in copper radiation may be a primary source of the density increase as well as an important energy loss channel. Charge exchange has been found to be the dominant loss mechanism in the intermediate temperature region with gyroradius effects being the limiting factors at the highest temperature.

J. C. Sprott

ACKNOWLEDGEMENTS

Throughout the years of this research, I have had the honor of working under the patient and understanding supervision and constant motivation of Professor J. C. Sprott during the various phases of this experiment. However, I owe a great debt to the many others who helped me, including T. Lovell for his invaluable fatherly advice and assistance in designing the various pieces of equipment used. B. Kolner showed that equipment can be fabricated with form as well as function in mind. The Physics Department Instrument Shop performed miracles of fabrication routinely. R. Vallem and his merry band of hourlies gave yeoman service in the maintainance of this equipment and Tokapole II. J. Twichell and M. Zarnstorff provided much consultation on computational matters, and C. Kieras developed a single particle code for the theoretical particle confinement scaling. D. Shepard also assisted with the ohmic heating voltage measurements.

Several faculty members, notably Professors R. Dexter and S. Prager provided hours of stimulating conversation and constructive criticism.

Financial support was provided by the United States Department of Energy.

TABLE OF CONTENTS

I. INTRODUCTION

Current thinking on the design of first generation tokamak reactors is that some form of supplemental heating beyond that provided by the ohmic input will be required to raise the plasma to the 10 keV ignition temperature required for the proposed deuterium-tritium mixture[1]. Several schemes have been developed, each with its own weaknesses and exploitable strengths. The most widely researched system in the United States is neutral beam injection (NBI). However, despite the impressive efficiency of the deposition of the beam's energy in the plasma and the simplicity of the physics involved, the future of the technology needed to produce these beams appears dim. Practical sources will require beam energies upwards of 200 keV. The neutralization efficiency of positive ion sources and the generation efficiency of negative ion sources are quite low at this energy, ~ 25%. Radio frequency heating suffers from no such efficiency limitations, but the physics and engineering of the coupling are extremely complicated. Nevertheless, there are many attractive features which commend the various radio frequency schemes. Perhaps most interesting are the lower hybrid wave techniques which promise to enable the construction of a steady state tokamak reactor, and the

fast magnetosonic wave techniques in the ion cyclotron range of frequencies (ICRF) which can both heat ions and modify the electron temperature profile.

Here I shall concentrate on the fast magnetosonic wave heating in a pure hydrogen plasma at the fundamental and the first four ion cyclotron harmonics. This avoids many of the complications of multi-species plasmas such as ion-ion hybrid resonances and mode conversion. The presence of the internal rings and the unusual plasma profile dictates the approach to be taken. First the unbounded dispersion relation is solved using cold plasma theory. Since the machine size and density are large enough to support multiple modes, measurements are made of the rf field structures under eigenmode resonance conditions. These results are used to guide a theoretical development of the bounded plasma case closely paralleling that of Stix[2]. A semi-quantitative model of the impedance imposed by the plasma is developed and compared with the frequency shift imposed on the rf source. The desirability and usefulness of using the reactive component of the plasma loading for passive mode tracking are considered. Power absorption at harmonics other than the second are also compared with theory. The lack of detailed energy and particle transport codes limit the ability to account for the input energy in detail,

however, the principle loss mechanisms can be described qualitatively.

Unless otherwise specified, all equations will be in MKS units, though other commonly used terms such as eV and density in number per cm^3 will be used in the text.

II. APPARATUS

A. Tokapole II

The substantive phase of these experiments occurred in the Tokapole II machine. This device and its design philosophy have been described in detail elsewhere[3,4], so only the most relevant parameters will be discussed here. The vacuum vessel consists of an aluminum toroidal chamber of 44 cm square cross section with a 50 cm major radius. Four toroidal copper rings of 5 cm minor diameter which generate the non-plasma produced poloidal field are supported within the tank (figure 2-1). These rings are inductively driven by a 7.2 mf 5 kV capacitor bank through an iron core transformer. The 40:1 turns ratio gives a sinusoidal current in the rings with a half period of 5.6 ms. The peak total ring current at the normal operating field levels is approximately 200 kA. The poloidal field duration may be extended by either passively crowbarring by shorting the primary windings with a diode as they pass through zero volts, or actively crowbarring by using a large capacity low voltage capacitor bank to supply energy to overcome the ohmic losses in the windings and hoops. The normal initial gap voltage is 55 V, with half this value appearing on the minor axis in the absence of plasma. Additionally, a toroidal magnetic field is

Figure 2-1.

Tokapole II cross section.

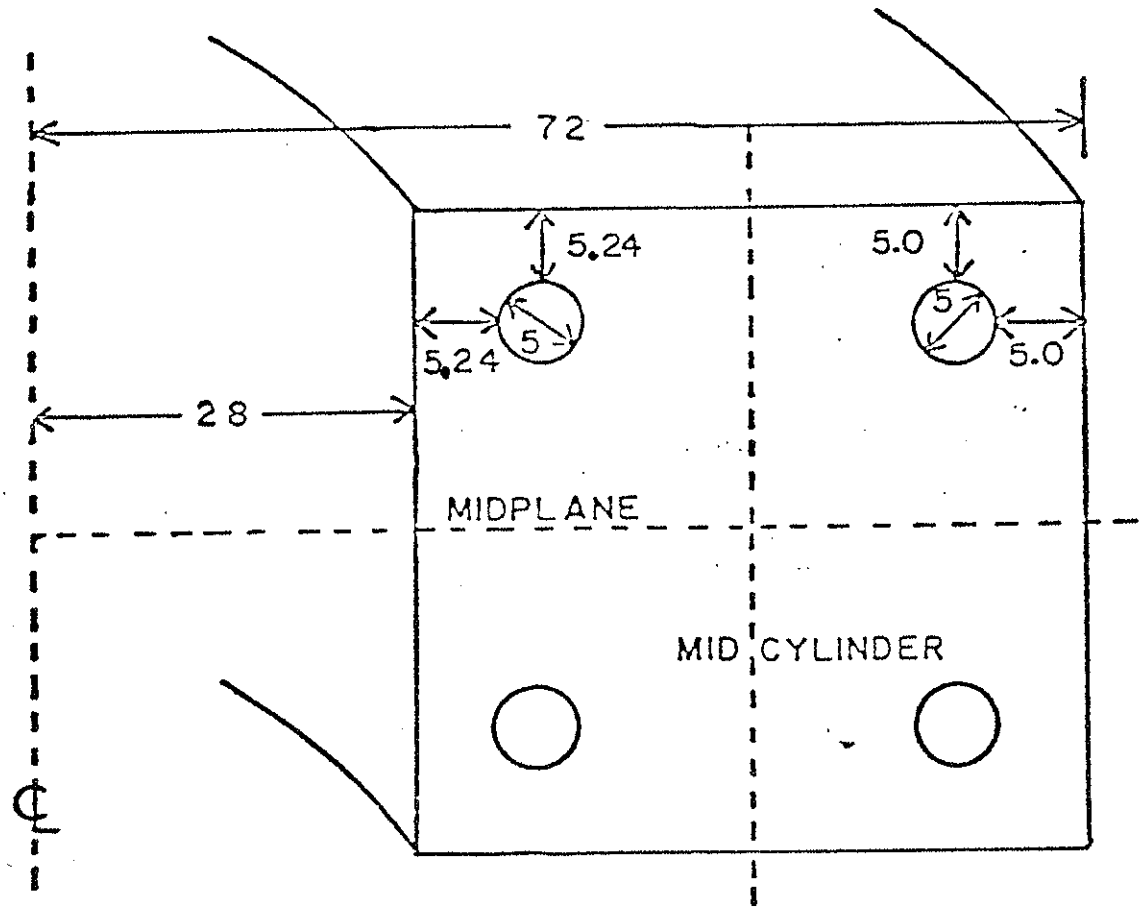

DIMENSIONS IN cm

produced by a 96 turn poloidal winding driven by a 32.24 mf 5 kV capacitor bank. The quarter period of the field is 5.4 msec, and it may be passively crowbarred. The crowbarred field varies by less than 5% during the experiment. Normally this field is adjusted to produce a 4 kG field on the minor axis.

The aluminum walls are of 3 cm thickness. A base vacuum of approximately 10^{-7} torr is maintained by a 1200 l/s turbopump and a 10 degree Kelvin 1000 l/s liquid helium cryogenic pump. The mounting adapters, in the case of the turbopump, a partially transparent copper plug whose purpose is to provide a net conductivity similar to that of a solid aluminimum wall to reduce field errors, reduce both pumping speeds by approximately 50%.

Plasma is produced by first filling the chamber with the working gas, usually hydrogen, through a fast puff valve. While a plasma can be produced as in a conventional tokamak by means of the toroidal ohmic heating electric field alone, it has been found advantageous to use microwave pre-ionization at the electron cyclotron frequency to reduce impurities[5] and provide better shot-to-shot reproducibility. Typical filling pressures are $\simeq 10^{-4}$ torr. The microwave plasmas are cold, T_i, $T_e \leq 3$eV, and the density is $\simeq 10^{10}$ cm^{-3}. Careful adjustment of the microwave supply timing also

reduces the x rays produced by runaway electrons. These interfere with certain diagnostics. Several sources have been used, including a continuous 100 W S-band (2.45 GHz), a 10 kW X-band (9 GHz), and a 5 kW K-band (16.5 GHz) magnetron. The latter two have 1 msec pulse lengths.

B. Radio Frequency Source

The rf source is an improved version of the single tube oscillator first constructed by J. Barter[6]. It may be conveniently divided into three components: the antenna, the oscillator, and the power supply.

The oscillator and the antenna must be considered somewhat together since the antenna is an integral part of the tank circuit. The oscillator (figure 2-2) is a modified two tube (Machlett #ML 8777) tuned plate tuned grid circuit in which the interelectrode Miller capacitance is resonated with an external inductor to a frequency above that of the tank circuit to provide feedback in the correct phase. The grid leak bias level is adjusted for maximum efficiency under load. This places the oscillator in the deep class C region with relatively narrow conduction angles. At power levels above 1.5 MW, the drive current spikes are truncated due to cathode emission limitation.

Figure 2-2.

ICRF generation system block diagram.

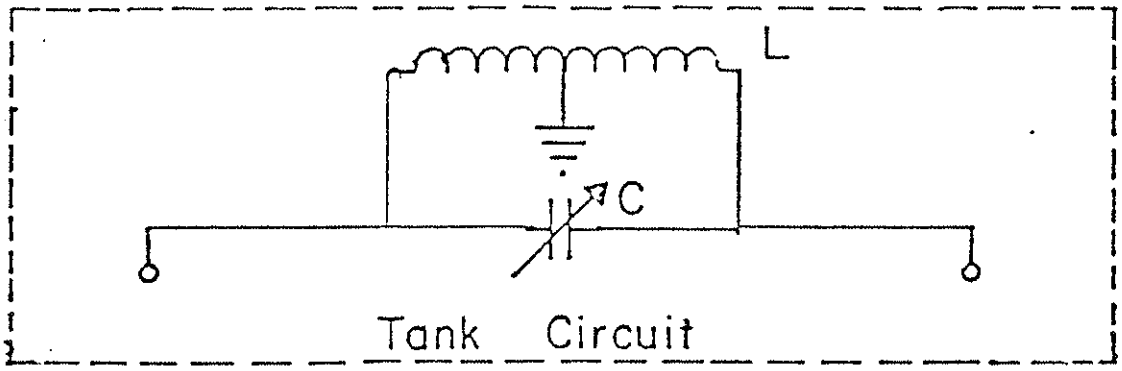
L
C
Tank Circuit

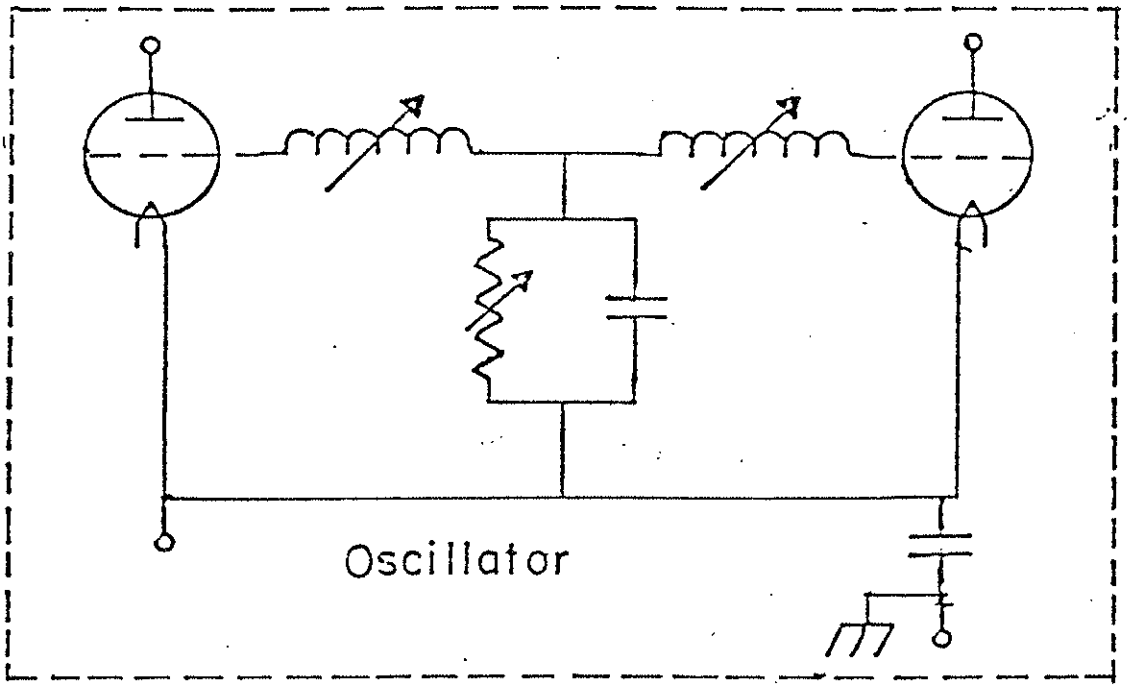
Oscillator

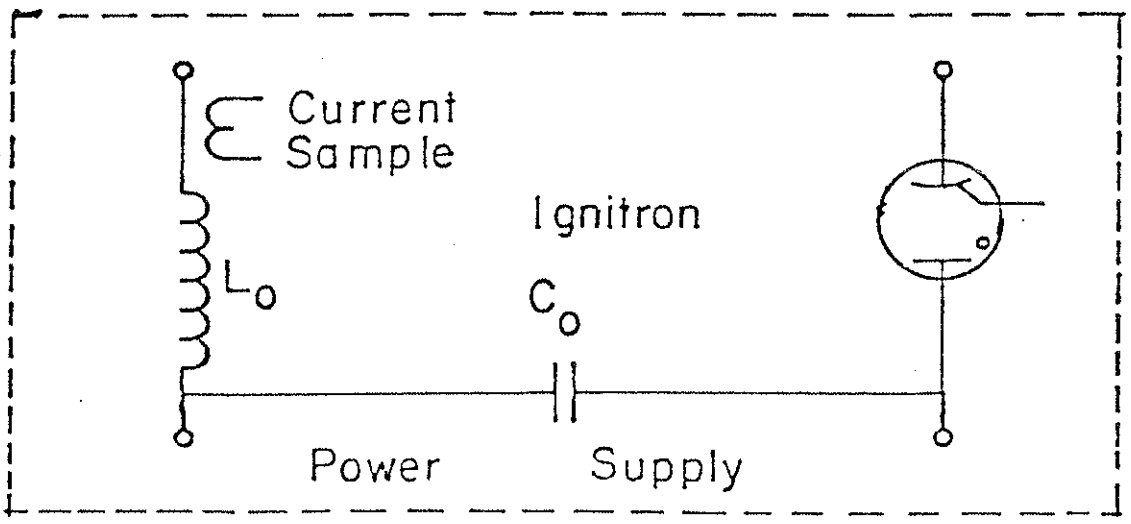
Current
Sample
Ignitron
L_o
C_o
Power
Supply

The center tapped tank circuit inductor also serves as the antenna. This arrangement has the advantage of eliminating the losses attendant to a matching network working into a rapidly changing load, and allows any reactance from the plasma to be coupled directly to the frequency determining element, thereby insuring the rf source is always "on frequency." Since the waves being excited are driven inductively, the inductance of the antenna and the joint resistance of the tank circuit were minimized to maximize the circulating current. The unloaded Q is ≃ 120. Rather than have the antenna operate at a high positive dc voltage in the plasma environment, the circuit is operated with the plates of the tubes at dc ground, and the cathodes are driven negative.

The antenna has existed in two basic forms. The Mark I (figure 2-3), did not extend into the plasma, but merely viewed it through a 15 cm diameter, 1.27 cm thick Macor window mounted in the bottom of the machine. The antenna itself consisted of a 2.54 cm wide, 0.6 cm thick copper bar which connected directly to the vacuum variable tank capacitor. This antenna coupled poorly, but did allow substantial wave propagation study.

The Mark IIa antenna (figure 2-4a) was constructed to satisfy several requirements. Coupling to the plasma is enhanced by maximizing both the area and the circulating

current in the antenna. To first order, these two are mutually contradictory, so a rectangle was used to allow the closest approach to the plasma current channel while minimizing its obstruction. The antenna had to be completely retractable from the machine under vacuum when not in use as well as be rotatable. Macor insulation was used, both to insulate the antenna from the plasma, and to shield materials such as teflon from plasma impact. While performing satisfactorily in most respects, the lack of a Faraday screen resulted in "parasitic loading" due to particles being accelerated by the electrostatic field near the antenna into the insulator. In addition to wasting power, significant impurities were introduced.

The Mark IIb antenna (figure 2-4b) was the Mark II with a Ø.Ø15 cm stainless steel grounded Faraday shield mounted over the Macor insulation. Since the shield is several skin depths thick, it was constructed with many slots to reduce eddy current losses. A partially transparent copper plug protects the lower part of the antenna, as well as reduces errors in the confining field.

The power supply[7] for the oscillator is a pulse forming network consisting of 1Ø discrete, inductively coupled, independently switchable LC sections (figure 2-2). This lumped-constant analog of a long transmission line has a characteristic impedance

Figure 2-3.

Mark I antenna and Tokapole II flux plot with plasma.

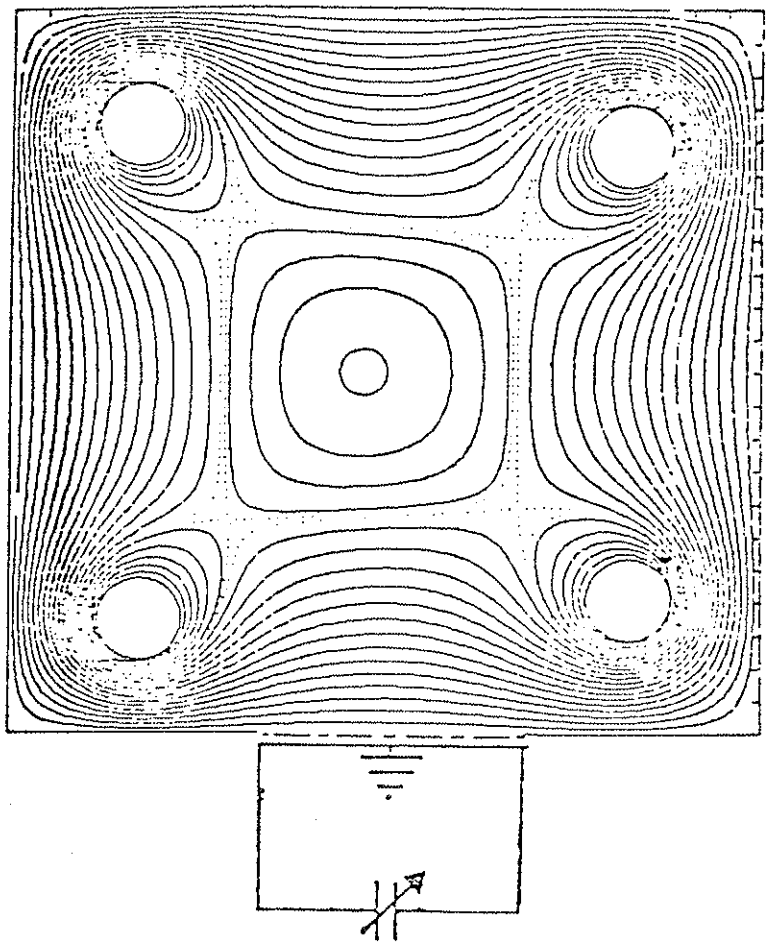

– – – Macor insulation

——— Copper antenna

Figure 2-4.

Mark II antennae and Tokapole II flux plot with plasma.

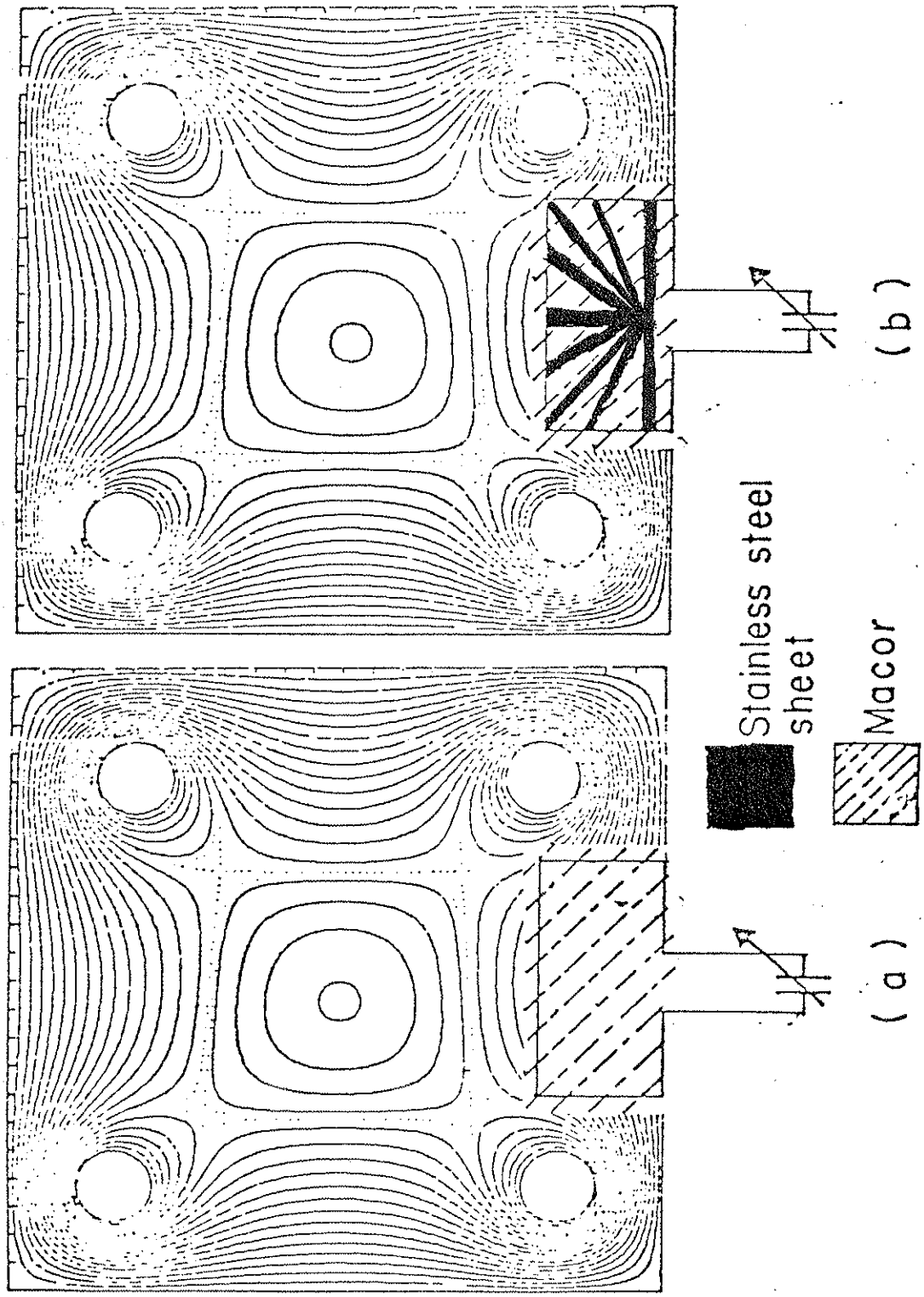
Stainless steel sheet
Macor
(a)
(b)

$R_o=(L_o/C_o)^{0.5}$, and when charged to a voltage V_o delivers $V=V_oR_1/(R_o+R_1)$ at a current $V_o/(R_1+R_o)$ to a resistive load R_1. Maximum power transfer occurs at $R_1=R_o$, but as will be shown in Section V, maximum power transfer to the plasma occurs at the highest V_{rf}^2 and hence the largest V_{dc}. Practical engineering dictates that R_1 be somewhat larger than R_o to allow the oscillator to function at its rated dc drive voltage. The mismatched line then produces multiple upright pulses of equal duration but decreasing amplitude. The parameters are: V_o=40 kV, R_o=100 ohms, primary pulse length=1.1 msec, and the total stored energy @ 40 kV is 4 kJ.

III. DIAGNOSTICS

A. Dynamic Frequency Measurement

Because the launching structure is an integral part of the frequency controlling elements in the oscillator, it is important to determine the frequency shift imposed by the reactive component of the plasma. Too large a shift would move the oscillator far enough from its optimum operating point to invalidate the loading measurement data calibration as well as decrease the oscillator efficiency. It also should be possible to detect the frequency shift caused by passage through an eigenmode.

The 1 msec pulse length precludes conventional frequency measurement techniques, but the new phase locked loop (PLL) integrated circuits produced by Signetics proved ideal for the purpose. A minimum of external parts was required (figure 3-1), and the input limiting (20dB) negated the possibility of changes in the output signal due to fluctuating loading of the oscillator. The error signal of the PLL is available and puts out a dc signal proportional to the difference between the PLL center (free-running) frequency and the input sample. This proved to be ~0.5 MHz per volt. In operation, the center

Figure 3-1.

Phase locked loop dynamic frequency meter.

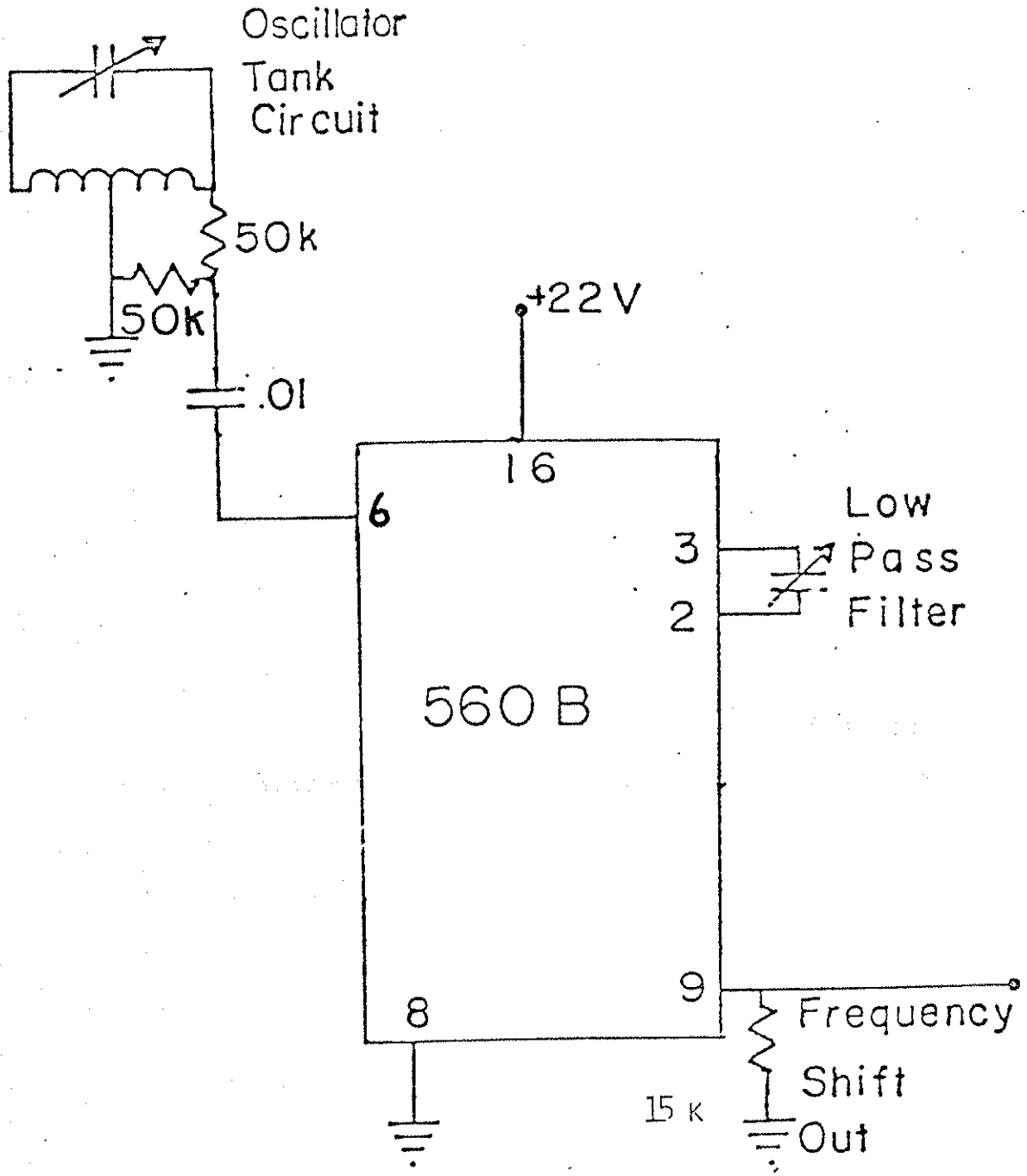
Oscillator
Tank
Circuit
50k
50k
.01
+22V
16
6
3
2
Low
Pass
Filter
560 B
9
8
Frequency
Shift
Out
15 K

frequency was chosen to be approximately that of the unloaded oscillator, though this was not critical.

For such a circuit there is an initial period before phase lock is achieved that depends weakly on the amplitude of the input signal and its difference from the center frequency, as well as other circuit parameters. The probability of lock[8] is nearly unity after 35 cycles, which here represents 3 μsec. In view of the 50 microsecond rise time of the pulse forming network power supply, this delay was not a factor. Observed lock always occurred before the dc drive voltage reached its maximum value.

B. Radio Frequency Probe

Because of the current interest in fast wave eigenmodes, it is necessary to be able to probe the radio frequency wave structures in the plasma. Figure 3-2 shows the design of this conceptually simple probe. Because of the highly destructive 100 eV plasma, the probe body had to be made of 0.64 cm diameter stainless steel tubing. Since the 0.041 cm wall represented many skin depths at 12 MHz, a protective tip of Macor ceramic was needed to protect the 4 turn search coil as well as to provide a gap to allow the rf field to penetrate the probe. Blocking capacitors were used to protect the probe electronics from the floating potential. A small rf transformer was used

Figure 3-2.

RF field probe system.

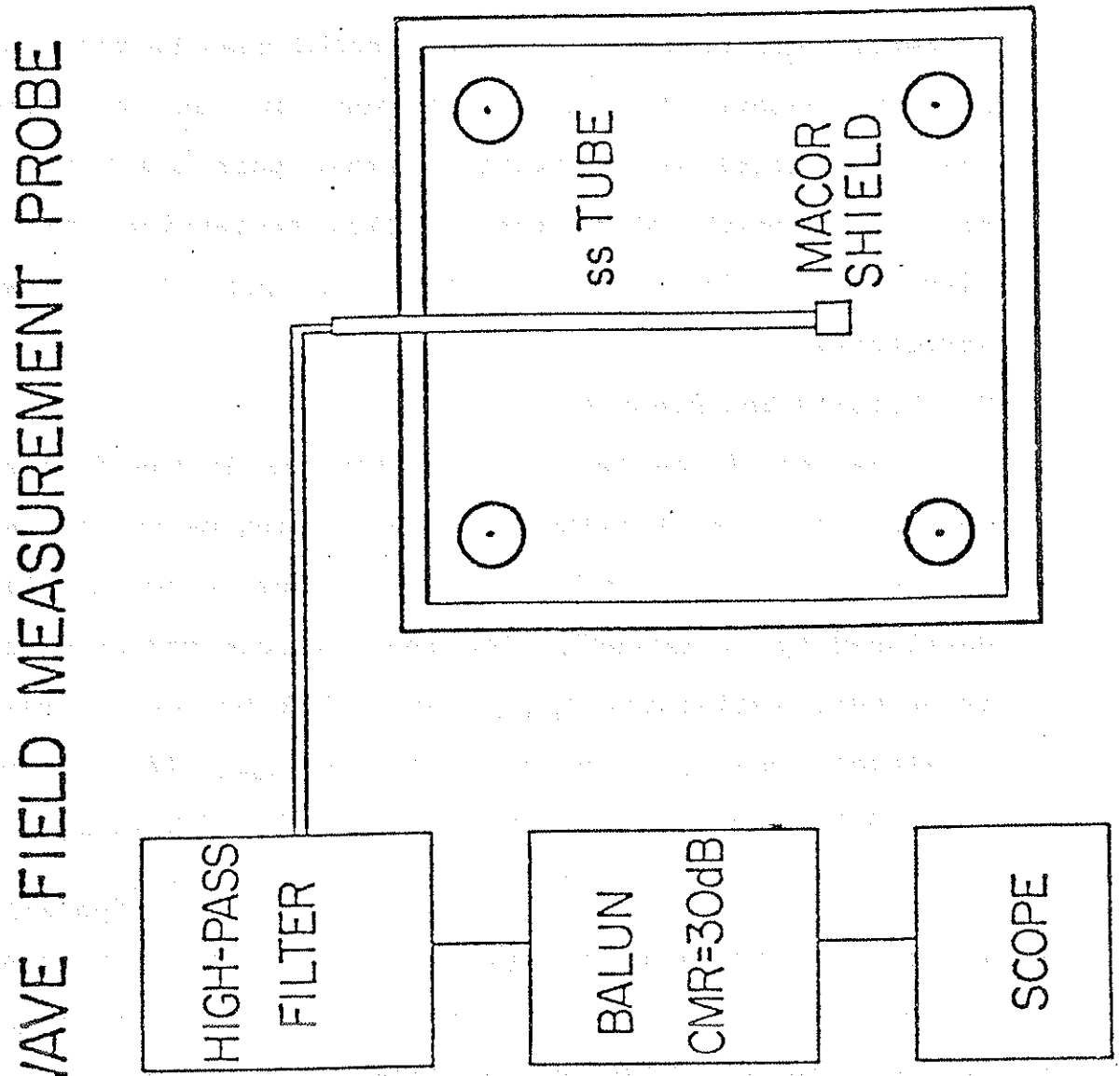
WAVE FIELD MEASUREMENT PROBE
ss TUBE
MACOR SHIELD
HIGH-PASS FILTER
BALUN CMR=30dB
SCOPE

to achieve a common mode rejection of ~30 dB . Calibration of the probe was done using a small cylindrical coil driven by an rf generator at known current. The rf field structure could then be plotted on a shot-by-shot basis. Insertion of an additional stainless steel rod at various other port positions did not significantly alter the results, suggesting that the first probe did not significantly perturb the wave structure.

C. Loading Measurement

The use of the tank circuit antenna as the frequency controlling element allowed plasma loading measurements to be made using a simplified version of a method first developed by J. Barter[6]. The tank circuit may be modeled as a pure resistance R_{tank} paralleled by an equivalent resistance R_{plasma} and reactance X_{plasma} (figure 3-3). Power delivered to the plasma is then $V^2_{rf_{op}}/2R_{plasma}$. The more commonly quoted R_{series} is given by $X^2/R_{parallel}$, where X is the reactance of one of the tank components, and is here ~45 ohms @ 12 MHz. The reactance X_{plasma} serves only to shift the oscillator to a new resonant frequency where the effective tank circuit is again purely resistive. Since dynamic frequency measurements have shown a negligible frequency shift, $\triangle f/f_o \sim 5 \times 10^{-3}$ in the presence of a plasma, calibrations done with lumped

Figure 3-3.

Oscillator tank circuit equivalence.

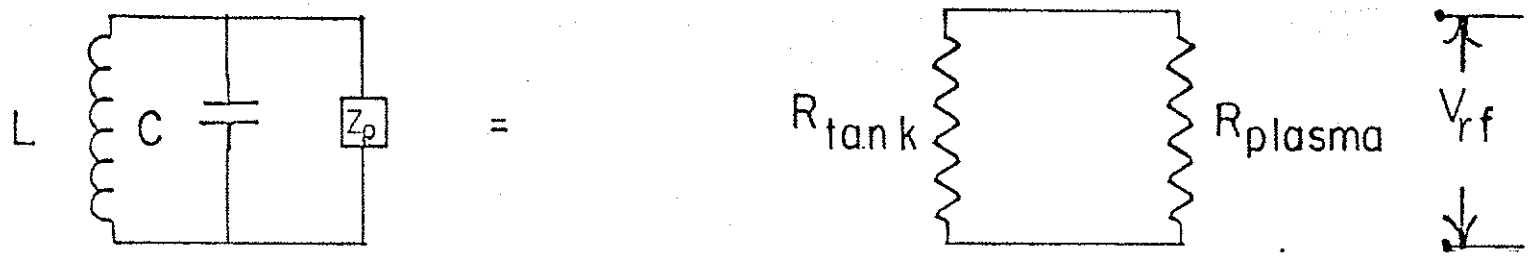

AT RESONANCE

resistive components are evidently valid. This calibration was accomplished by bridging the tank circuit capacitor with a string of non-inductive carbon resistors. The dc drive current was then monitored, and calibration curves evolved for various loading and power levels. It was sufficient to use the pulse forming network current diagnostic for even short lived eigenmode measurements, as this diagnostic sees the oscillator drive current through an effective RC time constant of only 6 μsec. Data were obtained by either acquisition through an on line PDP-11/20 or by oscillograph.

D. Ion Temperature Measurement-Doppler Broadening

One of the two most common ways to measure the ion temperature is by observation of the Doppler broadening of the spectral lines. In the absence of other broadening effects such as those caused by pressure, Stark, or Zeeman effects, the motion of thermal particles causes a broadening of the emission line which has a Gaussian shape (figure 3-4) given by[9]:

$$I_d = \left(\frac{m_i c^2}{2\,kT_i \lambda_o^2}\right)^{0.5} \exp\left(\frac{m_i c^2}{2kT_i}\left(\frac{\Delta\lambda}{\lambda_o}\right)^2\right) \qquad (3\text{-}1)$$

where m_i is the mass of the radiating ion, c is the speed

Figure 3-4.

Doppler broadened CIII spectral line.

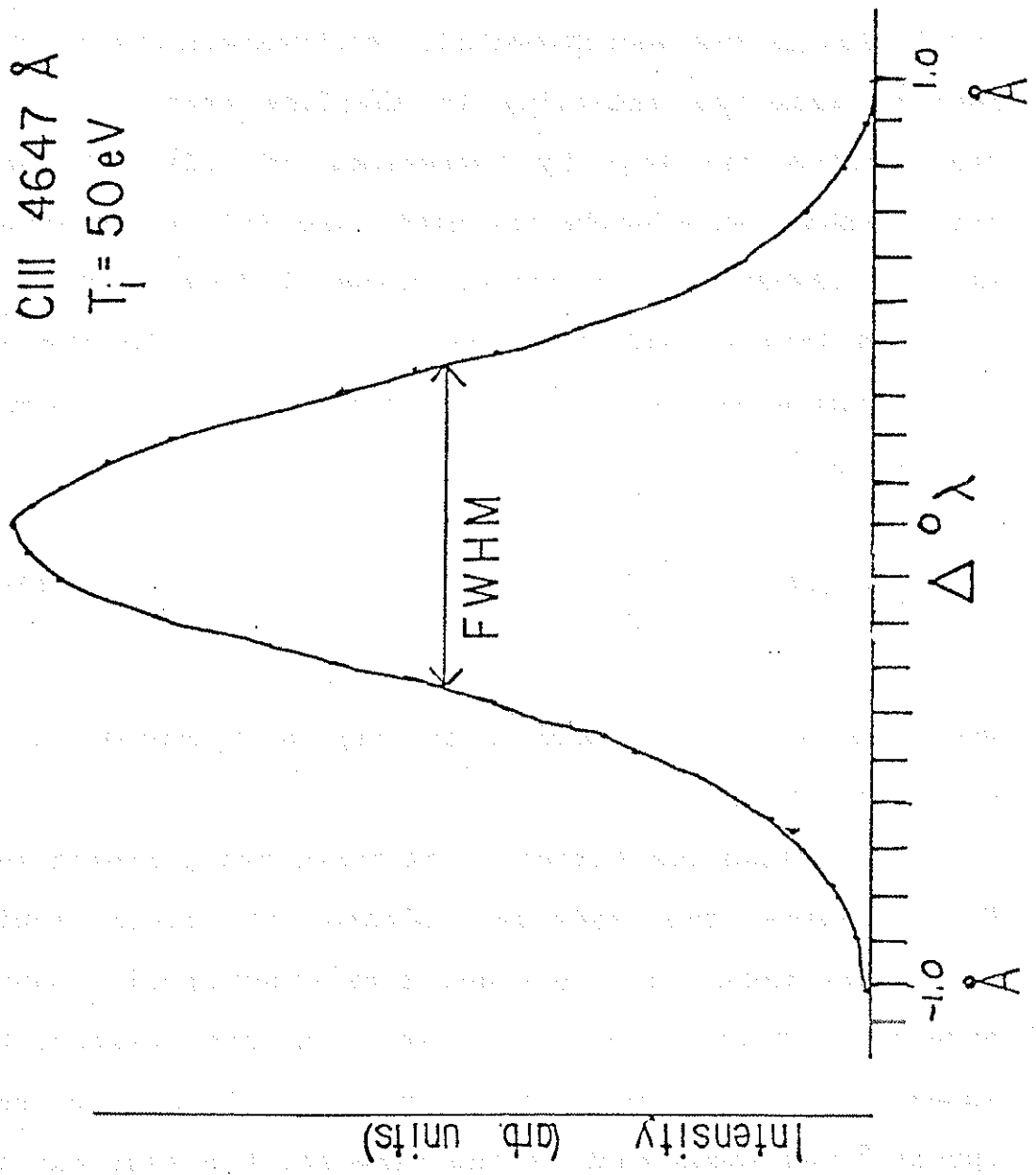
CIII 4647 Å
T_i = 50 eV
FWHM
Intensity (arb. units)
-1.0 Å
Δλ
1.0 Å

of light, k is Boltzmann's constant, λ_o is the line center, T_i is the ion temperature, $(\Delta\lambda)^2=(\lambda-\lambda_o)^2-(\Delta\lambda_i)^2$, and $\Delta\lambda_i$ is the instrumental width caused by the finite resolution of the monochrometer. Fortunately, one does not need to know the intensity in absolute terms. One can step across the line by increments of ~.1Å relying on shot-to-shot reproducibility until the full-width-at-half maximum (FWHM) can be either measured from a graph, or obtained from a best fit computer program. As the FWHM occurs where the exponential function has the value of 0.5, we get[9]:

$$T_i = 1.68 \times 10^8 \left(\frac{\Delta\lambda}{\lambda_o}\right)^2 A \qquad (3\text{-}2)$$

where T_i is in eV, and A is the mass number of the radiating atom.

This technique suffers from three basic limitations. First, since the hydrogen plasma is fully ionized everywhere except at the edge, some other species must be observed. This means either some impurity deliberately added, or preferably an impurity already present. Sprott[10] has shown that if the time for the test particle to equilibrate with the majority species is comparable to or greater than the confinement time for that species, the

impurity decouples and does not represent the majority temperature. Spitzer[11] shows that:

$$t_{eq} = \frac{7.34 \times 10^6 A A_b}{n_b Z^2 Z_b^2 \ln\Lambda} \left(\frac{T}{A} + \frac{T_b}{A_b}\right) 1.5 \qquad (3\text{-}3)$$

where t_{eq} is in seconds, A, A_b are the atomic number of the test and majority species respectively, Z is the impurity charge, Z_b is the background charge n_b is the density of the background species in cm^{-3}, T, T_b are the respective temperatures in eV, and $\ln\Lambda$ is the Coulomb logarithm, typically ~15. Hence one wishes to maximize Z^2/A of the impurity so that its thermalization behavior is as much like the background hydrogen as possible. In order for an impurity to be hydrogenic, it must be highly stripped. This is not generally possible in the T_e~100 eV plasma. CIII was normally used because it was the best line visible with our Jarrel-Ash monochrometer, but it is still a poor choice with Z^2/A~0.33. The second problem with Doppler techniques is a result of the strong dependence on T_e of the location of the radiating atoms. When this is known by means of radiometer measurements or other techniques, it is possible to calculate from the ionization rates the location of the radiating shell and

so derive a spatial ion temperature profile. Since this information is currently lacking in Tokapole II, it was impossible to be certain that the central temperature was being measured. Finally, at low impurity levels such as were finally achieved, the continuum radiation becomes a significant fraction of the line signal, resulting in poor signal to noise ratios. Nevertheless, this technique was useful in the initial phases of the experiment.

E. Ion Temperature Measurement-Charge Exchange Analysis

To supplement the above Doppler technique, a single channel charge exchange analyser (figure 3-5) was constructed. This technique has been developed by several researchers[12,13,14] as a means of more directly measuring the ion distribution in the plasma without recourse to perturbing or evaporating probes. The principle of operation is simple. The hot ions charge exchange with the residual background gas at a rate $n_o n_i \sigma v$, where n_o is the neutral density, n_i is the ion density, σ is the velocity dependent charge exchange cross section, and v is the ion velocity. Because the masses of the two particles are nearly identical, the collision is resonant, with the cold neutral now emerging as a fast particle with the same energy as the ion had.

$$H^+_{fast} + H^o_{cold} \rightarrow H^o_{fast} + H^+_{cold}$$

Figure 3-5.

Charge exchange analyser.

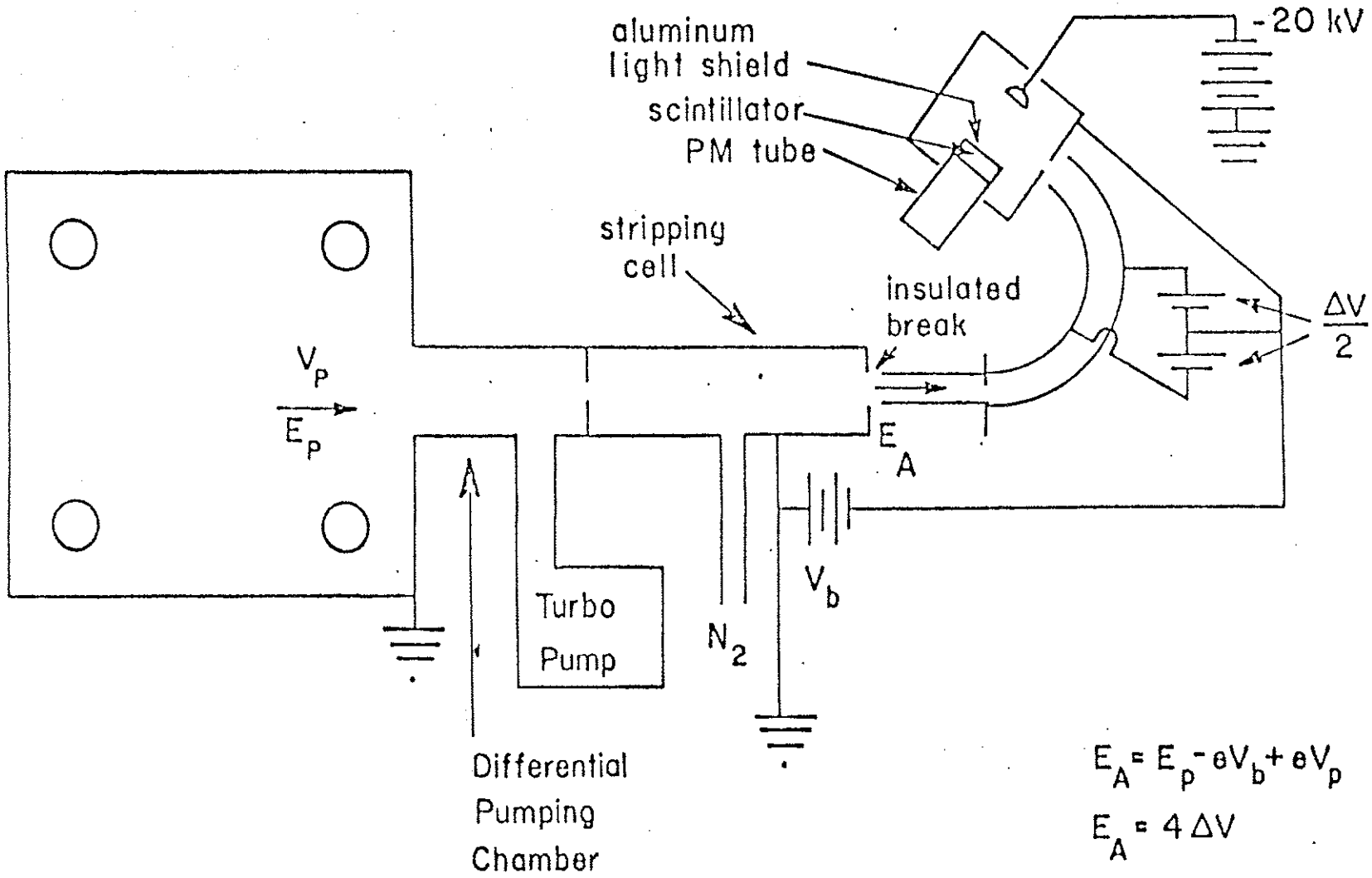

$$E_A = E_p - eV_b + eV_p$$

$$E_A = 4\Delta V$$

$$\therefore E_p = e(4\Delta V + V_b - V_p)$$

This neutral, assuming its mean free path is much larger than the plasma size, an assumption well satisfied in our machine, emerges through the confining magnetic field without further plasma interactions. It then enters a nitrogen stripping cell where it has some probability of losing its electron.

$$H^{o}_{fast} + N^{o}_{2} \rightarrow H^{+}_{fast} + N^{-}_{2}.$$

The fast ion is then analyzed by a 127 degree electrostatic curved plate analyser[15] and detected by a Daly detector whose output is proportional to the number of ions striking the detector knob and independent of their energy. Two modifications were made to the analyser to allow measurement of the relatively low temperature plasma. First, instead of using a continuous gas flow through the stripping cell with its attendant requirement for excessive amounts of differential pumping, a Veeco fast opening valve was used to pulse the stripping cell to ~4 microns. This resulted in a constant pressure for the duration of the experiment, but the gas loading of the pumping system and the Tokapole II vacuum was minimal. Higher pressure could not be used because of the requirement that the mean free path for low energy

particles be approximately the stripping cell length to prevent excessive scattering of the low energy particles. Secondly, because the bandwidth of the analyser[16] is proportional to the energy of the ion, the analyser was biased negatively with respect to the stripping cell, ~300 volts, to increase the analyser bandwidth. Normal technique was to vary the voltage on the curved plates from shot to shot and obtain the distribution function. The true distribution $\exp(-E/kT_i) \sim f(E)/E_p^{0.5}$ is obtained by weighting the PM tube output by the various conversion efficiencies,

$$\frac{f(E)}{E^{0.5}} \sim \frac{S}{A_{cx}(E_p)A_s(E_b)A_a(E_a)} \qquad (3-4)$$

where S is the output from the PM tube, E_p is the energy of the ion in the plasma, E_a is the ion energy in the analyser, and $A_{cx}(E_p)$[17], $A_s(E_p)$[18], and $A_a(E_a)$[6] are the relative conversion efficiencies of the plasma charge exchange, the stripping cell, and the curved plate analyser and detector, respectively. Noting that $E_a = E_p + V_b = 4V$, that $A_a(E_a) \sim E_a$, and that for 1 eV to 2 keV, $A_{cx}(E_p) \sim E_p^{.303}$, we can recast this as:

$$\frac{f(E)}{E^{0.5}} \sim \frac{S}{A_s(E_p)V(4V-V_b)^{.303}} \qquad (3\text{-}5)$$

where V is the voltage on the deflection plates, and V_b is the bias voltage. T_i can then be obtained from the slope of a least squares fit to a semilog plot (figure 3-6).

F. Plasma Density Measurement-Microwave Interferometer

Electron density n_e was measured by a 70 GHz microwave interferometer[19] which viewed the plasma through a vertical cord approximately centered on the discharge. Measurements of the line average density were obtained either by the direct observations of the interference fringes or by the standard "zebra stripe" technique in which the microwave source frequency was swept at one MHz to obtain a continuous display of the density evolution. The densities obtained were well below the cutoff frequency of the interferometer. The peak density in the center of the plasma was inferred to be ~60% greater than the average based on a cosine density distribution within the region limited by the antenna. A direct readout of density vs time based on a Princeton Plasma Physics Laboratory circuit is currently being implemented.

Figure 3-6.

Charge exchange analyser signal.

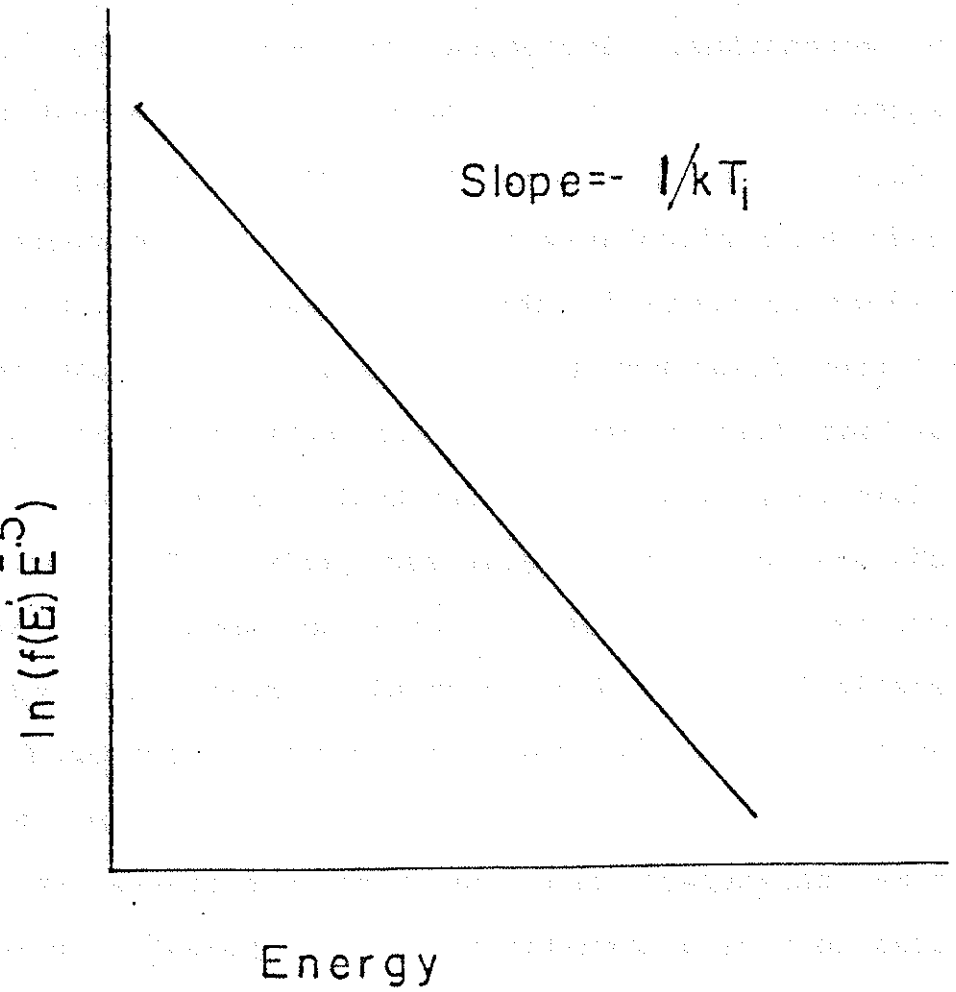
Slope =- 1/k T_i
ln (f(E) E^-.5)
Energy

IV. WAVE STRUCTURES AND BEHAVIOR

A. Wave Propagation and Penetration

Heating in the ion cyclotron range of frequencies (ICRF) in a single ion component plasma depends on one of two mechanisms, depending on whether the exciting frequency is near the fundamental or the second harmonic of W_{ci}. In the first case it is only necessary to impose a left hand circularly polarized (LHCP) component of the rf electric field in the rest frame of the ion at the cyclotron frequency (figure 4-1a). Even though both the slow and fast waves propagate near the ion cyclotron fundamental, it will be seen that the fast wave is purely right hand circularly polarized (RHCP). The slow wave is completely LHCP, but it will be seen to have poor accessibility to the central plasma and to cause significant edge heating. Above the cyclotron frequency only the fast wave propagates, and by proper choice of plasma parameters and launching structures it may be chosen to have a significant LHCP component. In order to drive the particles in phase so as to get coherent heating, a second mechanism must be invoked in which the rf driving frequency is an integral multiple of the ion cyclotron frequency. Power is then coupled into the ions due to a gradient in the rf electric field (figure 4-1b).

Figure 4-1.

Heating mechanism at (a) $W = W_{ci}$, (b) $W = 2W_{ci}$.

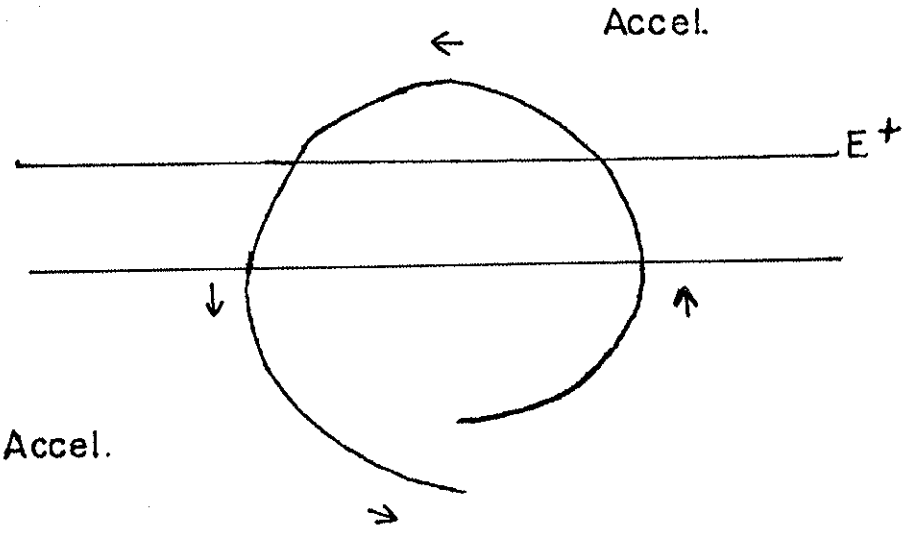

(a) $\omega = \omega_{ci}$

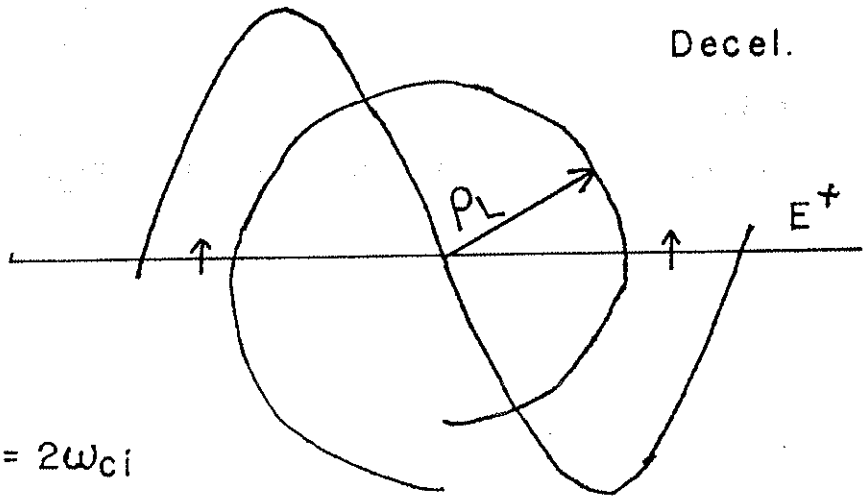

(b) $\omega = 2\omega_{ci}$

However, this coupling will be seen to be very weak with both attendant advantages and disadvantages. Finite temperature plasma theory yields some additional heating from the RHCP component, but its contribution is negligible.

We shall first define the appropriate hydromagnetic waves in an infinite plasma, then examine their various properties, and finally adopt the appropriate finite geometry model. Following Stix[2] we can write the wave equation for a cold, homogeneous plasma:

$$\bar{n} \times (\bar{n} \times \bar{E}) + \bar{\bar{K}} \cdot \bar{E} = \emptyset \qquad (4\text{-}1)$$

where $\bar{\bar{K}}$ is the dielectric tensor defined by Stix[20], $\bar{n} = \bar{k}c/W$ where $\bar{k}$ is the wave number with k_y assumed $\emptyset$, $k_{||}$ is the wave number parallel to the static magnetic field, c is the vacuum speed of light, and W is the angular frequency. Following the literature, the "||" and "z" subscripts will be used interchangeably. Expanding this explicitly gives:

$$\begin{pmatrix} K_{xx}-n_z^2 & K_{xy} & n_x n_z \\ K_{yx} & K_{yy}-n^2 & \emptyset \\ n_z n_x & \emptyset & K_{zz}-n_x^2 \end{pmatrix} \begin{pmatrix} E_x \\ E_y \\ E_z \end{pmatrix} = \emptyset \qquad (4\text{-}2)$$

For simplicity we further restrict ourselves to the high density, low frequency regime where $W \ll W_{ce}$, W_{pi}, W_{pe}, and the parallel conductivity is high. Here W_{ce} is the electron cyclotron frequency, and W_{pi} and W_{pe} are the ion and electron plasma frequencies, respectively. We arrive at the following ordering: $|K_{zz}| \gg |n_x^2|, |n_x n_z|$. This gives $|E_z| \ll |E_x|, |E_y|$ for typical MHD regimes. We shall set $E_z = \emptyset$, an approximation which is well satisfied at all points in the plasma except in the vacuum-plasma interface at the edge where heating is negligible. Noting the $K_{xx} \simeq K_{xy} \simeq (R+L)/2$ and that $K_{xy} \simeq K_{yx} \simeq i(R-L)/2$ we can further simplify to:

$$\begin{pmatrix} R+L-2n_z^2 & -i(R-L) \\ i(R-L) & R+L-2n^2 \end{pmatrix} \begin{pmatrix} E_x \\ E_y \end{pmatrix} \simeq \emptyset \qquad (4\text{-}3)$$

where $R \simeq [W_{ci}/(W_{ci}+W)]/V_a^2$ and $L \simeq [W_{ci}/(W_{ci}-W)]/V_a^2$ and V_a is the Alfven velocity. Finally, we define the Alfven indices of refraction as $N_\perp = V_a/V_\perp = k_x/k_A$, $N_\parallel = V_a/V_\parallel = k_z/k_A$, and write equation 4-3 as:

$$N_\perp^2 = A - N_\parallel^2 + \frac{A(1-A)}{A-N_\parallel^2} \qquad (4\text{-}4)$$

where $A = W_{ci}^2/(W_{ci}^2-W^2)$. Taking into account the possible sign ambiguities, we may write explicitly for $N_{||}$:

$$N_{||}^2 = \frac{2A-N_{\perp}^{2\pm}\,\mathrm{sign}\left(\frac{W}{W_{ci}}-1\right)\left(N_{\perp}^4+4A(A-1)\right)^{.5}}{2} \qquad (4\text{-}5)$$

where the upper sign is chosen for the fast wave and the lower sign for the slow wave. Figure 4-2 shows a plot for $W = 1.5\ W_{ci}$, and figure 4-3 shows a similar plot for $W = 1/2\ W_{ci}$. The fast wave propagates at all fields, but the cyclotron wave is evanescent above the cyclotron frequency. Even below the cyclotron frequency the slow wave is profoundly effected by its direction of propagation, unlike the fast wave, which is nearly isotropic (figure 4-4).

Figure 4-4 also demonstrates the fundamental problem of using the slow wave in a toroidal reactor. $N_{||}^2$ is essentially constant with respect to changes in $N_{\perp}^2$. Unlike the convenient magnetic beach arrangement which may be engineered into stellarators which allows the slow wave to propagate along the field lines to the resonant region through relatively constant density, a tokamak configuration requires an antenna to be located in the low density region. A wave propagating around the torus

Figure 4-2.

Hydrodynamic wave dispersion relation for $W = 1.5W_{ci}$. (Adapted from ref. 2)

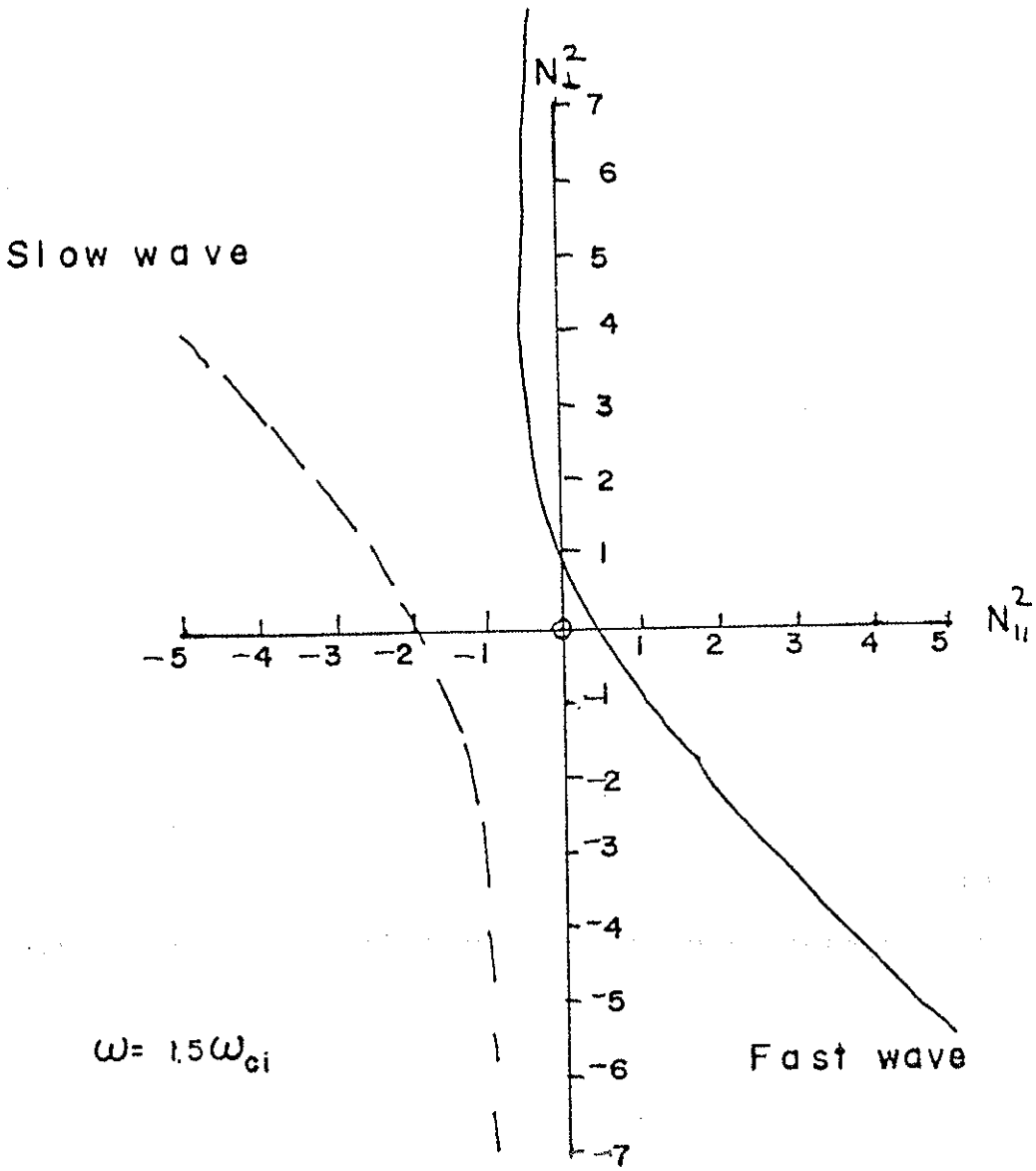
Slow wave
$N_\perp^2$
7
6
5
4
3
2
1
$N_\parallel^2$
-5 -4 -3 -2 -1 1 2 3 4 5
-1
-2
-3
-4
-5
-6
-7
$\omega = 1.5\omega_{ci}$
Fast wave

Figure 4-3.

Hydrodynamic wave dispersion relation for $W = .5W_{ci}$. (Adapted from ref. 2)

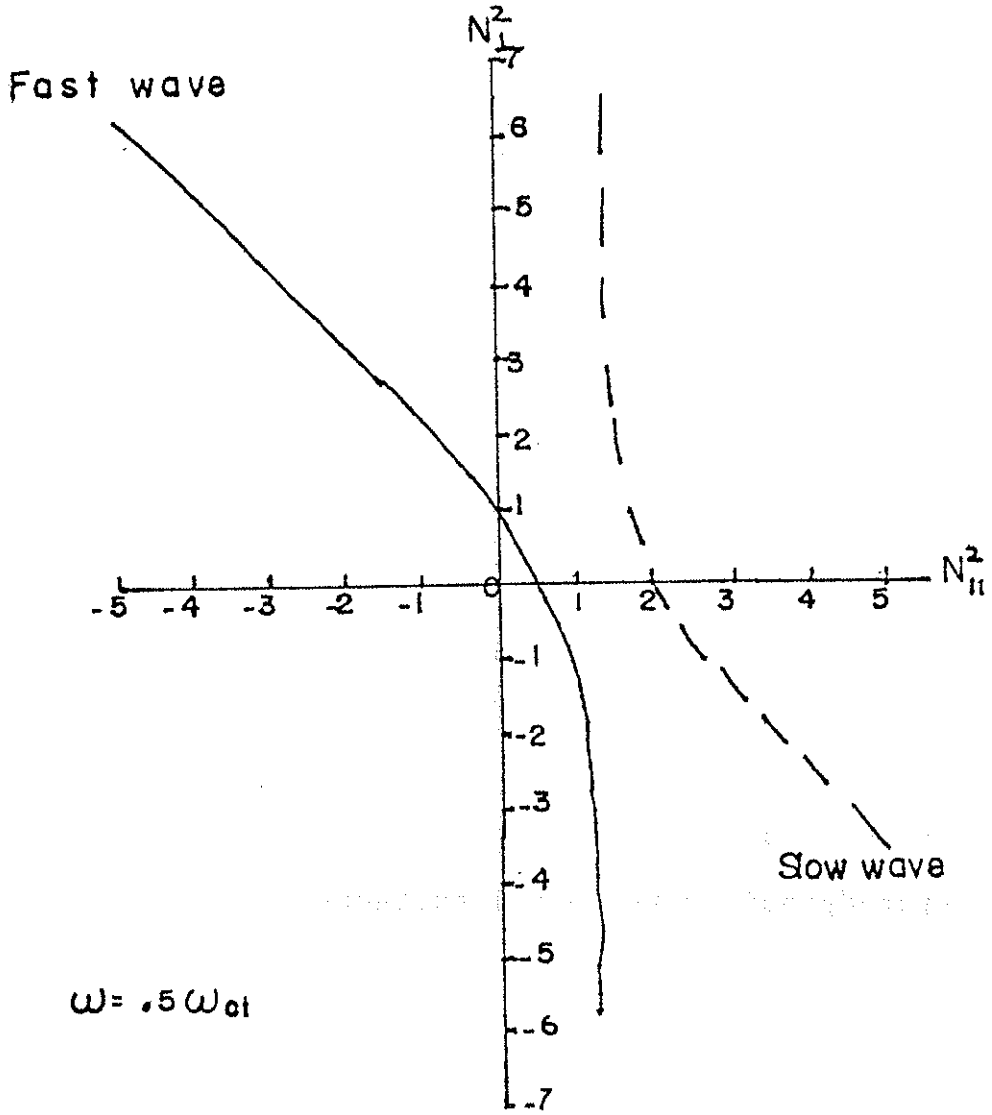
Fast wave
$N_\perp^2$
7
6
5
4
3
2
1
-5 -4 -3 -2 -1 0 1 2 3 4 5
$N_{||}^2$
-1
-2
-3
-4
-5
-6
-7
Slow wave
$\omega = .5\,\omega_{ci}$

Figure 4-4.

Hydrodynamic wave-normal surfaces.

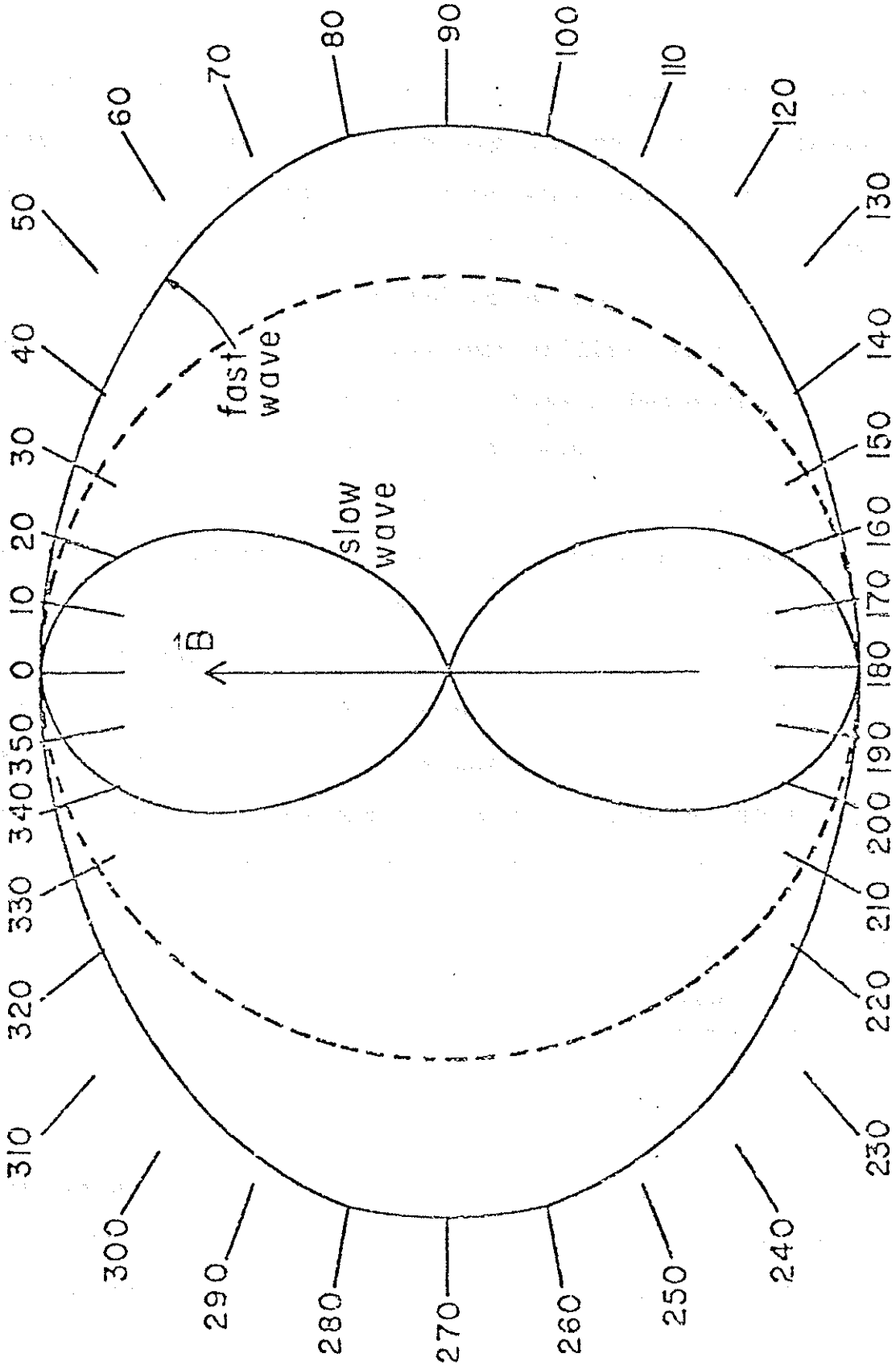
fast wave
slow wave
B
0
10
20
30
40
50
60
70
80
90
100
110
120
130
140
150
160
170
180
190
200
210
220
230
240
250
260
270
280
290
300
310
320
330
340
350

toward the core will experience little change in its parallel wave number, but the increasing density causes the perpendicular wave number to increase rapidly. The wave is quickly refracted toward the perpendicular ion cyclotron resonance which prevents it from reaching the core. A more familiar case would be that of visible light being refracted toward the normal when passing into an area where the index of refraction is increasing. Thus all heating occurs at the edge of the plasma.

Having disposed of slow wave heating, we will now concentrate on the fast wave as the only viable ICRF technique for a tokamak. To develop an approach for fast wave heating, we need to examine first the polarization of the electric field. Using equation 4-3 we can solve for the LHCP component $E_+ = E_x + iE_y$ and the RHCP component $E_- = E_x - iE_y$. The ratio of the two components is just:

$$\frac{E_+}{E_-} = \frac{\frac{W_{ci}}{W+W_{ci}} - N_{||}^2}{\frac{W_{ci}}{W-W_{ci}} + N_{||}^2} \qquad (4\text{-}6)$$

Figure 4-5 shows this ratio for various values of W/W_{ci} over the propagating range of $N_{||}^2$. Two trends are immediately obvious: increasing W/W_{ci} increases the

Figure 4-5.
$\frac{E_+}{E_-}$ vs N_{11}.

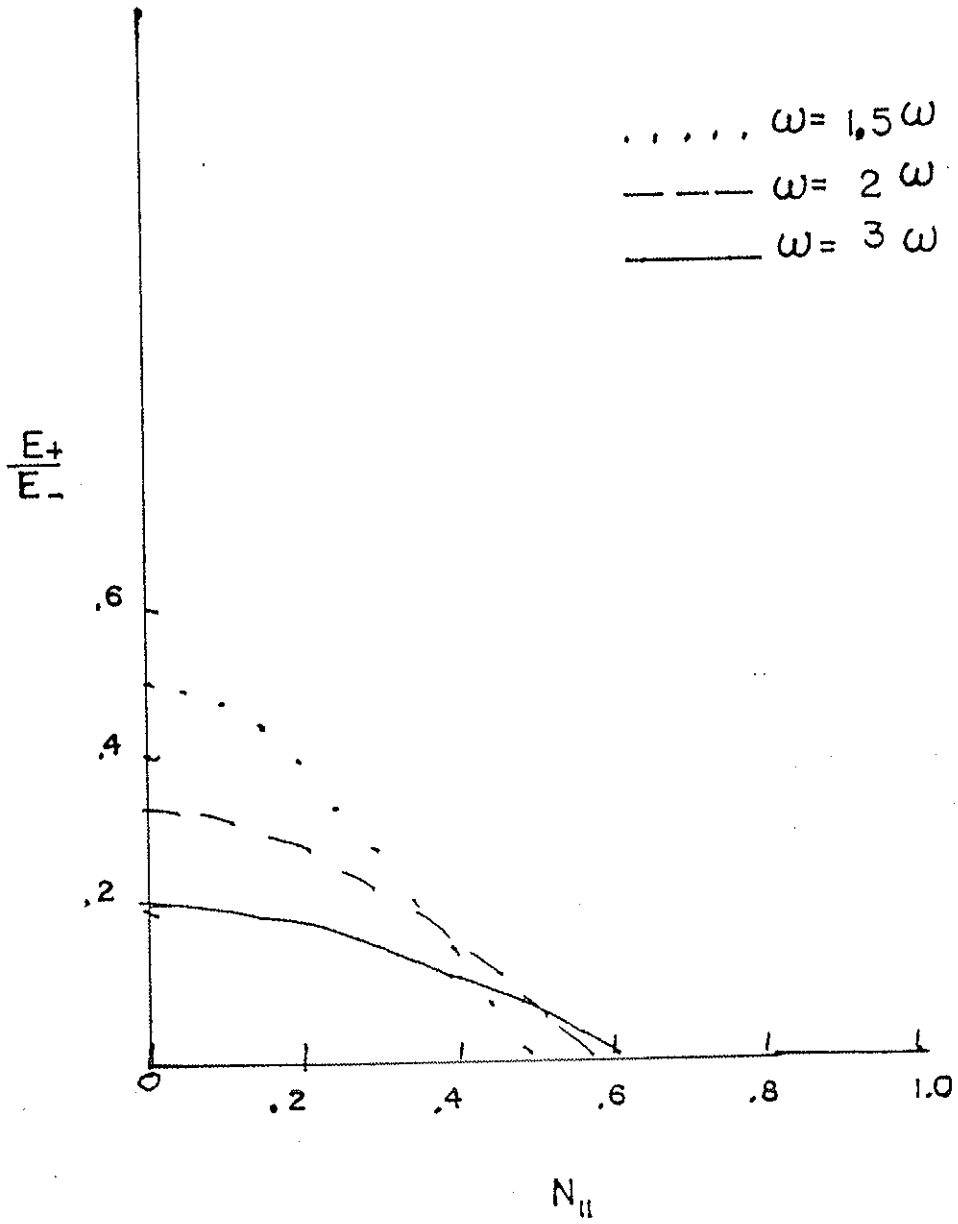
. . . . . ω= 1,5 ω
— — — ω= 2 ω
_____ ω= 3 ω
E+/E-
.6
.4
.2
0
.2
.4
.6
.8
1.0
N||

fraction of E_+, and increasing the parallel wave number decreases it. In section V it will be shown that increasing W beyond approximately $2W_{ci}$ actually decreases the heating efficiency for reasons associated with the width of the resonant zone and the portion of velocity space in which heating is peaked. The dependence on $N_{||}^2$ is strong motivation for the use of an array phased in the toroidal direction in a large machine to suppress high k_z modes. A small device such as Tokapole II in which the density of modes is low is best left to pick whatever modes are possible by variation of the plasma density.

A qualitatively accurate understanding of the criteria for modes to be present comes from the requirement that as in a microwave cavity there are minimum values of k_{z_o} and $k_{\perp o}$ with all allowed modes being approximate integral multiples of these. For any toroidal geometry there must be an integral number of full wavelengths in the toroidal direction. The criterion for the perpendicular direction is dependent on the waveguide geometry. For a rectangular case with conducting walls we require that one half wavelength stands across the cavity, while in the circular case the diameter must be 1.3 wavelengths. Figure 4-6 is a plot of the propagating dispersion relation with the typical mode numbers appropriate for Tokapole II superimposed. Eigenmodes

Figure 4-6.

Propagating eigenmode dispersion relation.

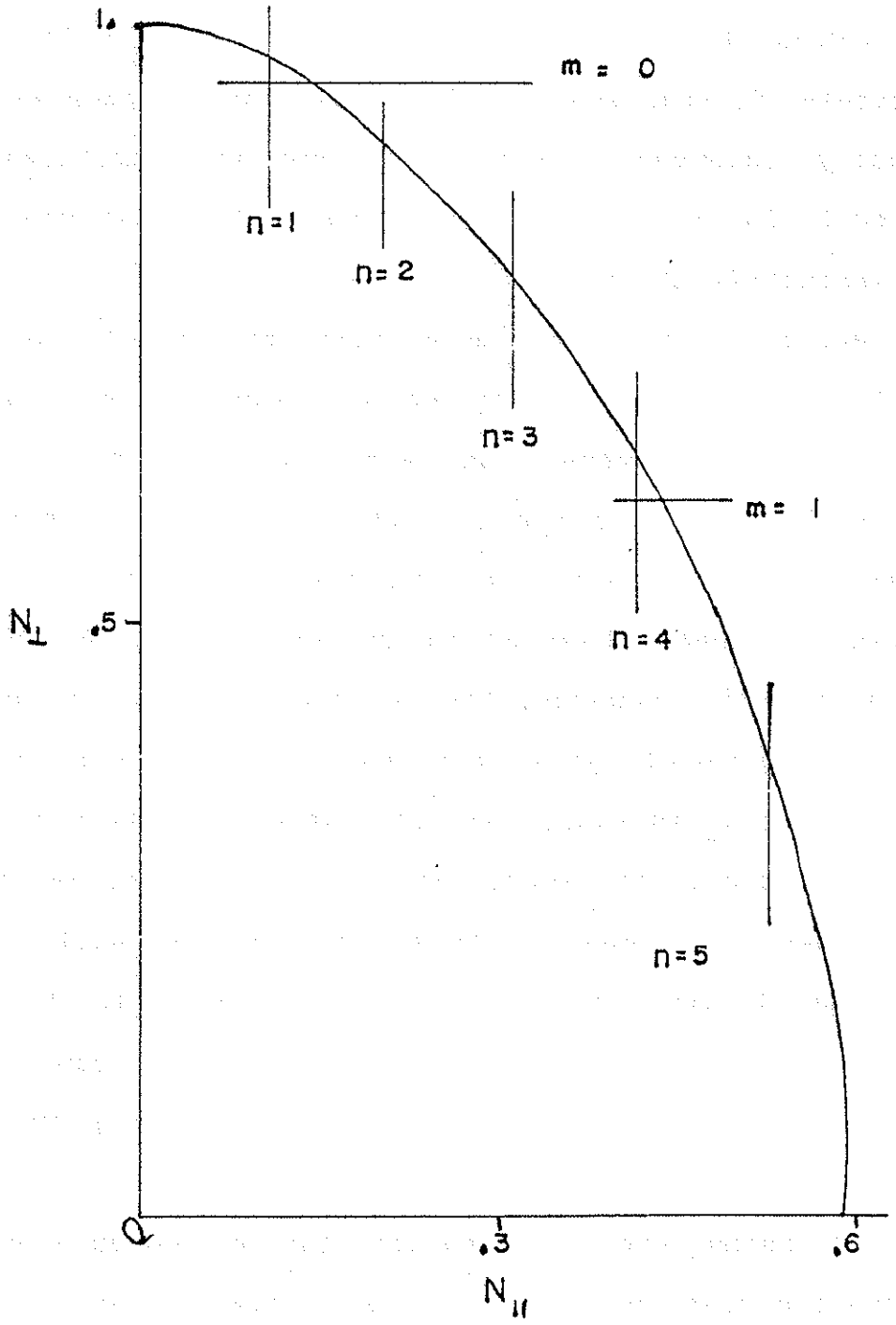
1.
m = 0
n=1
n=2
n=3
m = 1
n=4
n=5
$N_\perp$
.5
0
.3
.6
$N_{||}$

occur when the discrete mesh intersections coincide with the dispersion relation. Just satisfying one wave number is ordinarily insufficient as the wave will still interfere destructively. The fact that eigenmodes are actually observed despite the numerous approximations needed to do the calculations demonstrates that modes are not infinitely sharp.

Before considering more realistic models we must consider the accessibility of the wave to the plasma. Unlike the slow wave, the fast wave suffers no strong absorption. Even in the case where the machine size and density are too small to support a propagating wave, heating has been observed in the evanescent region near the antenna[21]. However, the requirement that the wave be propagating complicates coupling as well. The parallel wave number k_z is approximately constant across the plasma cross section, at least in an average sense on an eigenmode. This must apply to the edge as well. Since the edge density drops sharply, the perpendicular wave number drops quickly and becomes imaginary, causing the fields to evanesce before they can reach the propagating region.

By using the mode number for k_z imposed by the propagating region of the plasma we may use equation 4-4 to examine the behavior of the perpendicular wave number.

For imaginary values of the perpendicular wave number its reciprocal is just the e-folding length for the field. Figure 4-7 shows the decay length at various edge densities as a function of the toroidal mode number. Picking 5 as typical we can see that for a core density of 10^{13} cm^{-3} the decay length is infinite, and the wave propagates as expected. Below this density the decay length drops quickly, and for $\leq 10^{11}$ cm^{-3}, characteristic of the edge density in Tokapole II, the e-folding length is nearly constant at 10 cm. Since heating goes as $|E_+|^2$, coupling is very poor unless the antenna is located in or very near a fully propagating zone. The Mark I antenna was very inefficient for this reason, with most of the power not reaching the central plasma. Also, since the hoops tend to behave as magnetic limiters, the vacuum region is relatively larger than in conventional tokamaks. This problem is further complicated by the large size of the Mark II antenna which introduces additional losses and significantly decreases the density throughout the machine. This problem becomes less severe as the toroidal mode number is reduced, and it will not be a factor in a large device. The largest currently operating devices, PLT and TFR, have sufficient density at the limiter to allow wave propagation in the area around the antenna as

Figure 4-7.

Evanescence length vs toroidal mode number.

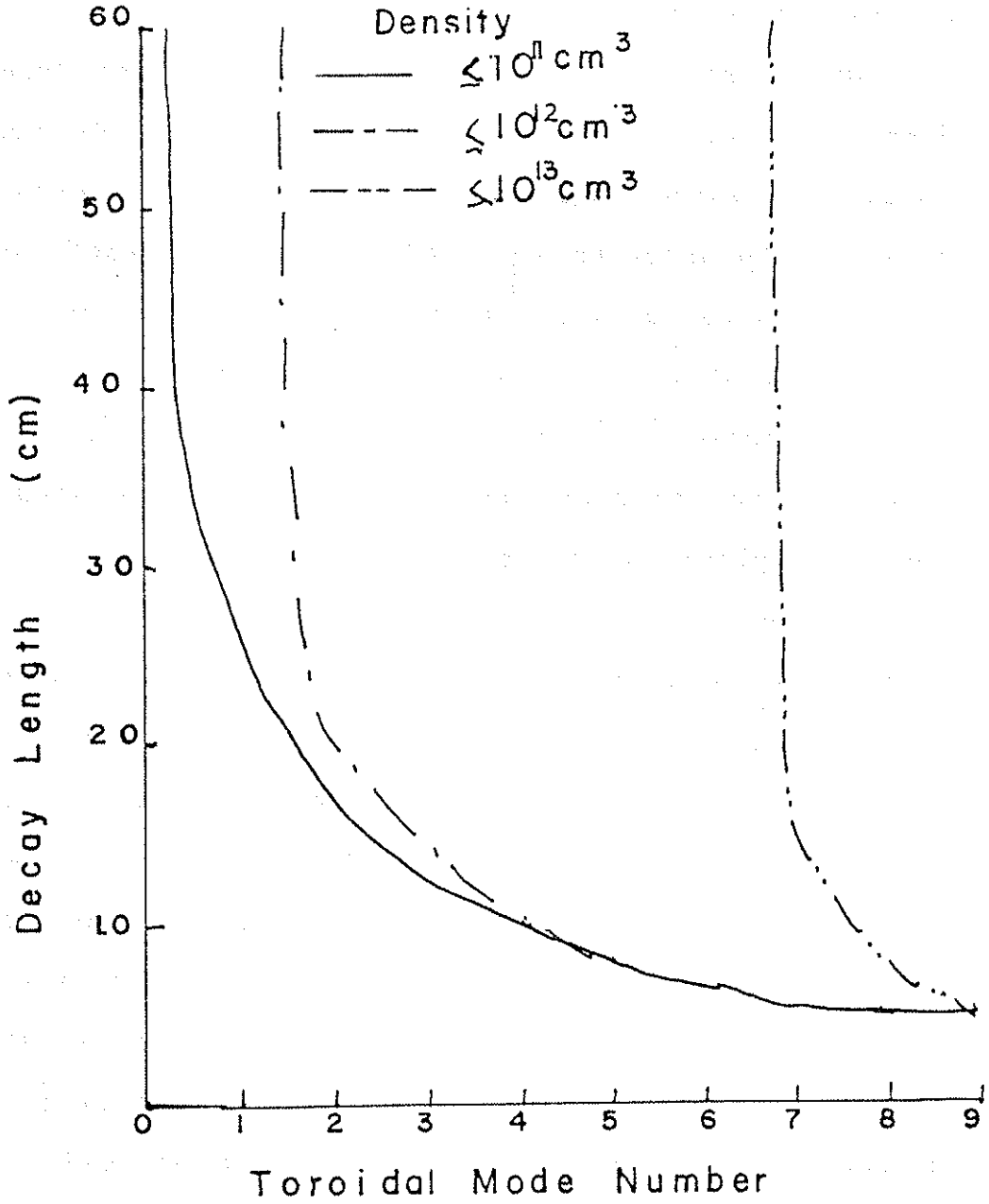
Density
$\lesssim 10^{11}$ cm^{-3}
$\lesssim 10^{12}$ cm^{-3}
$\lesssim 10^{13}$ cm^{-3}
Decay Length (cm)
60
50
40
30
20
10
0
1
2
3
4
5
6
7
8
9
Toroidal Mode Number

well as substantially higher core densities which further reduces the requirement on the edge density.

B. Eigenmode Structure

While we have previously used only the unbounded dispersion relation, we must now impose the boundary conditions which will bring about several important new effects. In order to make this problem tractable we need to make several additional assumptions. First we will not attempt to utilize the warm plasma dispersion relation. Several studies[22,23] have shown that cold plasma theory describes the propagation aspects well for a single ion component plasma with hot theory used only for the heating calculations. We also will ignore the effect of the rotational transform since the parallel wavelength is a small fraction of the machine circumference. The gradient in B_t is also ignored since we have only a single species plasma without mode conversion effects. Finally, we will for the most part ignore the effects of the poloidal field. This field results in lifting the degeneracy with respect to the propagation velocity in a straight currentless cylinder with only a static field in the z direction. Chance and Perkins[22] first pointed out this effect due to the poloidal field caused by the current. Detailed theory[24] shows that the splitting is proportional

to the poloidal mode number m, but is non-zero even if m = Ø.

The imposition of boundedness on the plasma is equivalent to requiring that the dispersion relation also satisfy Maxwell's boundary conditions. We shall assume a plasma column of uniform density with a sharp plasma-vacuum boundary surrounded by a perfectly conducting shell. The result of this procedure has been in substantial agreement with much more detailed calculations using as many as 1ØØ concentric shells of varying density[24].

We shall use the following cold plasma formulation of the wave equation in cylindrical geometry due to Woods[25]:

$$b_r + ib_\theta = i(C - k_{||}A)J_{m+1}(k_\perp r) \tag{4-7}$$

$$b_r - ib_\theta = i(C + k_{||}A)J_{m+1}(k_\perp r) \tag{4-8}$$

$$b_z = k_\perp A J_m(k_\perp r) = b_{z_o} J_m(k_\perp r) \tag{4-9}$$

$$E_r = \frac{W}{k_{||}} b_\theta \tag{4-1Ø}$$

$$E_\theta = -\frac{W}{k_{||}} b_r \tag{4-11}$$

$$E_z = \emptyset \tag{4-12}$$

$$\frac{C}{Ak_{||}} = \frac{(\frac{W}{W_{ci}})(k_{||}^2 + k_{\perp}^2)}{k_a^2 - k_{||}^2} \tag{4-13}$$

Here the convention is that the waves have solutions of the form $f(r)e^{i(k_{||}+m\theta-Wt)}$. The literature is approximately evenly divided between this convention and one with the same f(r) but with the i in the exponential term replaced by -i. This has the effect of reversing the sign of the m terms.

The limiting case of a fully filled waveguide requires $E_z(a) = E_\theta(a) = \emptyset$ at the wall radius a. $E_z(a)$ is automatically $\emptyset$ by equation 4-12. We can find an approximate solution for $E_\theta = \emptyset$ by noting that for a fast wave both sides of equation 4-13 are approximately unity making the polarization essentially RHCP. Under this assumption we get $J_{m-1}(k_{\perp}a) = \emptyset$. Similarly in the case of

a plasma surrounded by an infinite vacuum region we get $J_m(k_\perp a) = \emptyset$ by requiring continuity of the z and θ components of the electric and magnetic fields. For the intermediate case both sets of boundary conditions are required yielding a total of 6 boundary conditions across the plasma vacuum interface and at the wall. Paoloni[26] has demonstrated using a much more sophisticated formalism retaining electron inertia and hence a non-zero E_z that these rules:

$$\emptyset < W_{co} < \frac{2.4}{r_p} V_a \qquad m = +1 \qquad (4\text{-}14)$$

$$\frac{2.4}{r_p} V_a < W_{co} < \frac{3.83}{r_p} V_a \qquad m = \emptyset \qquad (4\text{-}15)$$

$$\frac{3.83}{r_p} V_a < W_{co} < \frac{5.2}{r_p} V_a \qquad m = -1 \qquad (4\text{-}16)$$

for propagation apply well to the m = +1, $\emptyset$, -1 modes where the range in the cutoff frequencies W_{co} depends on the surrounding vacuum blanket thickness. Figures 4-8 and 4-9 show the theoretical plots for propagating waves with a 2 cm vacuum blanket. The waves are sensitive to the

Figure 4-8.

Theoretical eigenmode structures for m = 1 and m = Ø with vacuum blanket.
(Adapted from ref. 26)

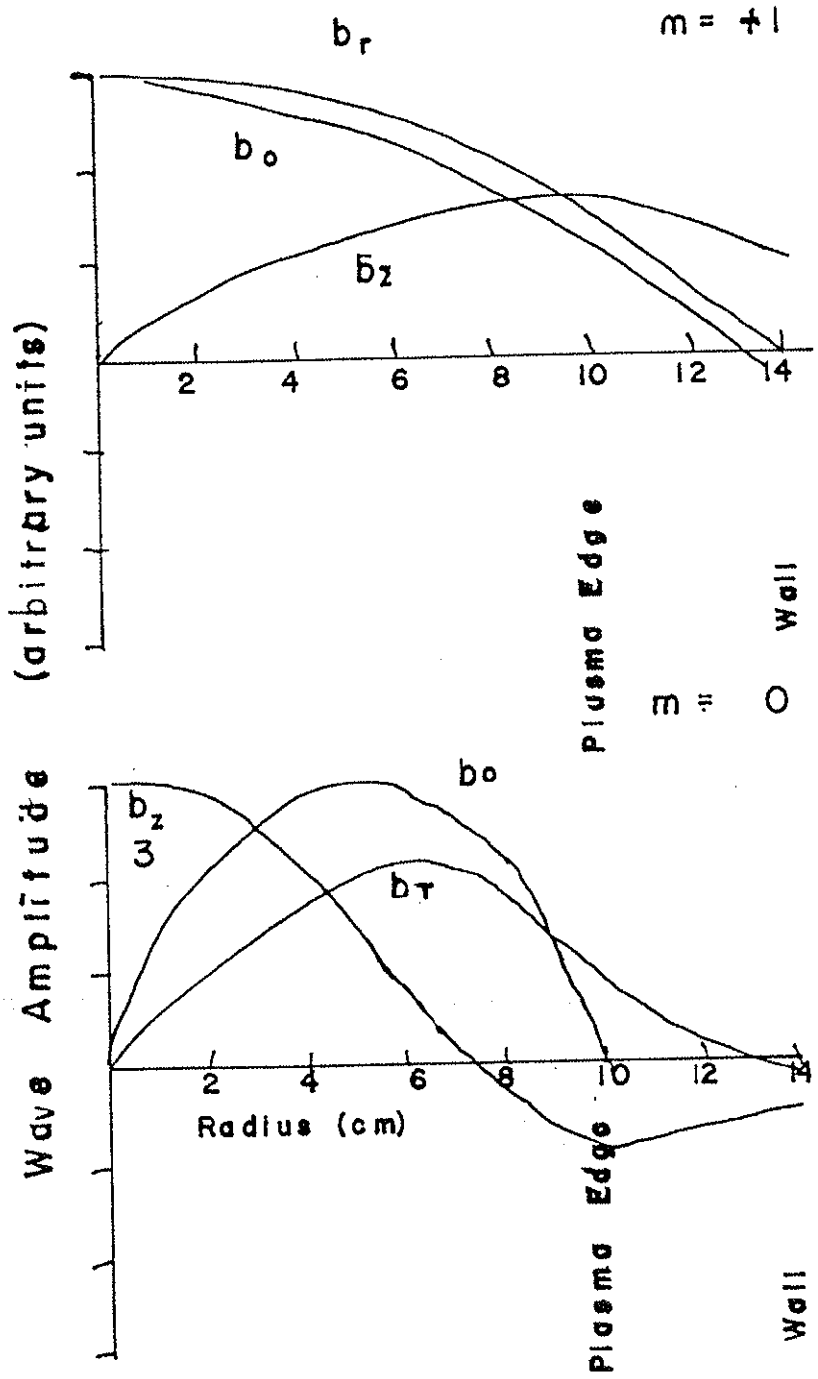
b_r
m = +1
b_o
b_z
2
4
6
8
10
12
14
Wave Amplitude (arbitrary units)
Plasma Edge
Wall
m = 0
b_o
b_z
3
b_r
2
4
6
8
10
12
14
Radius (cm)
Plasma Edge
Wall

Figure 4-9.

Theoretical eigenmode structures for m = -1 and m = +1*.
(Adapted from ref. 26)

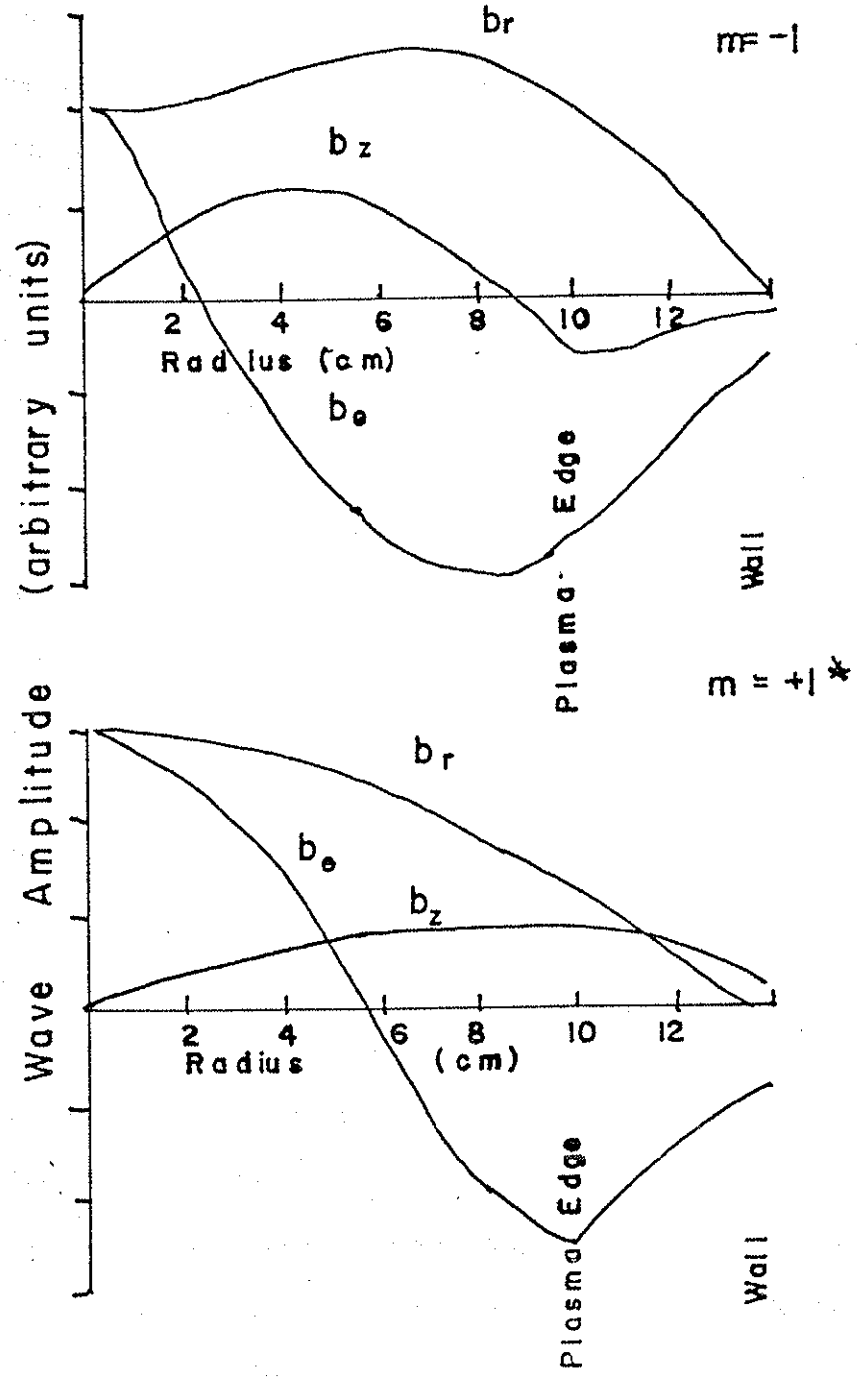
br
m = -1
bz
2
4
6
8
10
12
Radius (cm)
bθ
(arbitrary units)
Plasma Edge
Wall
m = +1 *
br
bθ
bz
Wave Amplitude
2
4
6
8
10
12
Radius
(cm)
Plasma Edge
Wall

sign of m. This result "comes out of the dispersion relation," but it is intuitively reasonable if one distinguishes between the spatial rotation of the instantaneous field patterns and the polarization which describes the rotation of the fields themselves at constant z. Klozenberg, McNamara, and Thonemann[27] first demonstrated in the low frequency limit that for positive m numbers the field pattern and the waves rotate in the same sense, while for negative mode numbers there is competition resulting in at least one radial null in b_σ.

The vacuum layer profoundly effects the m = +1 mode. For vacuum layers greater than a few cm the m = +1 wave does not suffer a cutoff and propagates with a nearly constant phase velocity. Below the normal propagation density the m = +1 mode undergoes a profound change in field structure. Here the $|b_r|$ flattens somewhat, not dropping until near the vacuum-plasma interface. More importantly the $|b_\sigma|$ component passes through zero near r = $.3r_p$ before reaching a secondary peak near the vacuum-plasma interface. This resembles the m = -1 mode found when the density is high enough to support normal propagation. The two modes can be separated without detailed phase information by noting that for the m = +1 mode $|b_\sigma(\text{interface})| \sim |b_{\sigma_o}|$, but for the m = -1 mode $|b_\sigma(\text{interface})| = 2|b_{\sigma_o}|$. A difference crucial to

heating is that for the m = -1 mode the wave is predominantly LHCP near the axis, becomes linearly polarized near the zero in the wave poloidal field, and then becomes predominantly RHCP until reaching the plasma edge. The reverse is true for the m = +1 mode. This m = +1 mode below normal cutoff will be designated the m = $+1^*$ mode for brevity.

The unusual structure of Tokapole II makes exact calculations of the wave propagation difficult without certain approximations. In addition to a weak poloidal field generated by the plasma current which reaches a value of 400 Gauss at the separatrix, ~.1 $B_t(0)$, the hoops also produce poloidal fields which under normal conditions reach values of 6 kG at the hoop surface. Clearly the small poloidal field approximations break down here. Fortunately the Mark II antenna acts as its own limiter, effectively blocking the plasma current outside a radius of approximately 13 cm as well as reducing the density substantially below that necessary for propagation. The plasma radius is actually rather diffuse and varies as a weak function of the plasma position. We shall ignore the hoop field since it is in the vacuum region as well as the imposition of conducting wall boundary conditions "near" the current channel over a relatively small region. With these assumptions the 9 cm vacuum region places the walls

effectively at infinity. We can then use equations 4-15 and 4-16 to calculate the cutoff frequencies W_{co} for various mode numbers. Assuming an average density in hydrogen of 5 x 10^{12} cm^{-3} and B_t = 4.0 kG we get f_{co} = 11.5 MHz for m = 0 and f_{co} = 18.2 MHz for m = -1. The actual values are probably slightly higher due to the proximity of the conducting hoops. These calculations suggest that modes for m = +1* should be the first seen at the lowest density in the discharge with the m = 0 mode being just accessible at the highest densities. The 12 MHz rf source would require a density of 1.2 x 10^{13} cm^{-3} for the m = -1 mode or have its frequency moved to 18 MHz for the available density.

C. RF Magnetic Field Measurements

The relatively low temperatures found in Tokapole II combined with the limiter action of the Mark II antenna allowed the use of the insertable probe described in IIB rather than the conventional edge probes with the concomitant requirement for detailed phase information to unfold the data. Insertion through either a mid-plane or mid-cylinder probe port allowed the direct measurement of the b_z and b_θ components directly with the probe search loop perpendicular to the other two field components. While the b_r component is not readily measured, the other two are sufficient to unambiguously determine both the

mode excited and the power input. The probe had little effect on the plasma. It was necessary to account for a slight variation in the starting time of the discharge by correlating the rf fields with the enhanced loading of the rf source by monitoring the oscillator drive current spikes. As expected, the field patterns of the modes observed on the early rising edge of the plasma density were characteristic of the m = +1* mode made possible by the large vacuum boundary (figure 4-10a). At the highest density, $\bar{n} = 5 \times 10^{12}$ cm^{-3}, patterns characteristic of the m = 0 modes were observed (figure 4-10b) as well as the normal m = +1 mode (figure 4-10c). As was expected the m = -1 mode was not observed under the conditions of the standard discharge. The actual measured fields will be used in section VI for the heating calculation. The measurements show a postiori that the assumptions concerning the location of the the plasma-vacuum interface were valid.

D. Passive Mode Tracking

We turn now to an elegant formalism proposed by Stix[2] which can be made to yield an intuitively understandable picture of an eigenmode as well as providing a quantifiable model which bypasses many experimental complications. Consider first a linear waveguide infinite in the z direction containing some plasma and a static

Figure 4-10.

Measured wave amplitudes.

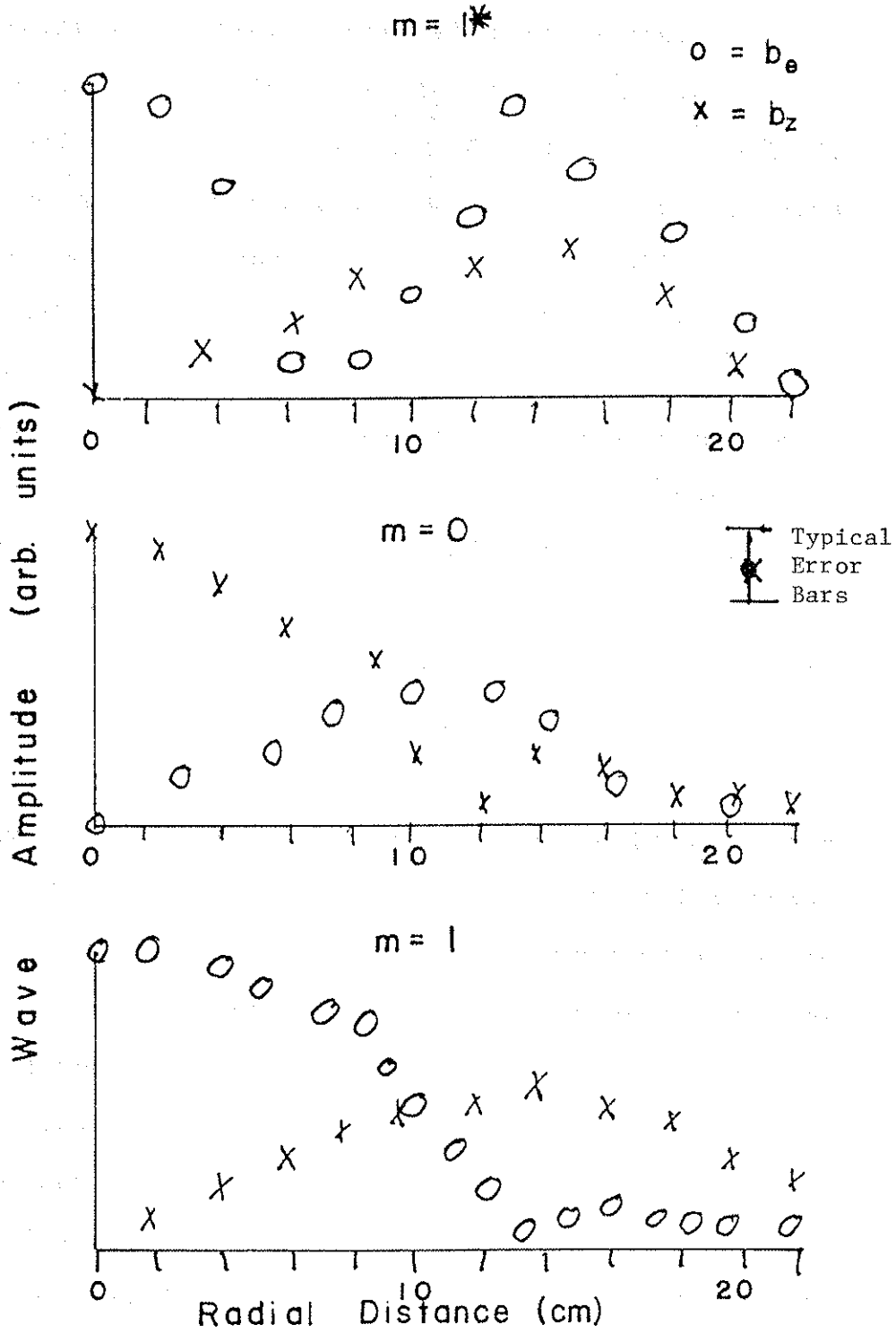
m = 1*
o = b_e
x = b_z
0
10
20
m = 0
Typical
Error
Bars
Wave Amplitude (arb. units)
m = 1
Radial Distance (cm)

magnetic field B_t along the z axis. The cross section and plasma parameter profiles are completely arbitrary so long as they are not functions of z and they allow propagation of the fast wave. A current loop of equally arbitrary shape protrudes into the waveguide at z=Ø with length 2l (figure 4-11a). The antenna launches waves in both z directions, but by symmetry we will consider only the right traveling wave. For an antenna whose length is much less than the parallel wavelength of the fast wave, it can be shown[20] that the electric field ramps up linearly beneath the antenna from a value of zero at z = -l to a value of E' at z = +l. This can be thought of as the result of a series of filamentary currents each launching its own wave in phase with its neighbors. The sum departs from linearity as the antenna length in the z direction becomes a significant fraction of the parallel wavelength. The total back electric field, even for a long antenna, averages to some value we will call E_o. Suppose further that we have calculated this plasma response E_o to the particular current distribution for the specific geometry of the experiment. Now place an infinite array of identical antennae in the waveguide at a spacing of 2 R (figure 4-11b). The first antenna to the left generates at the test antenna an additional back electric field twice that of the single antenna, but attenuated and phase

Figure 4-11.

Plasma filled waveguide model.

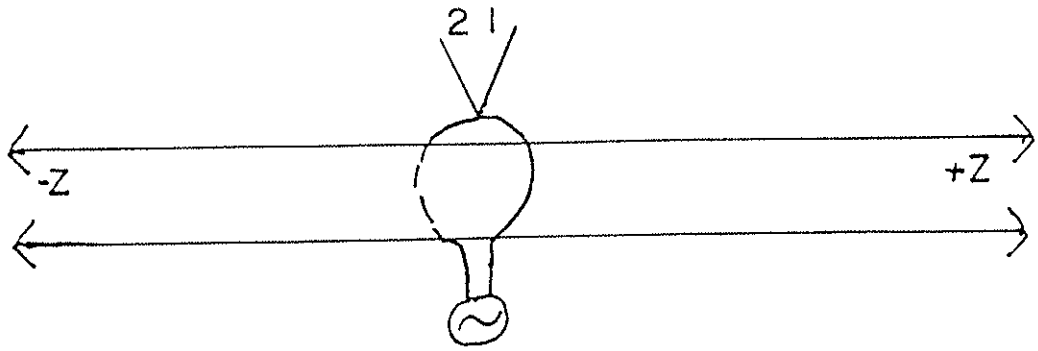

4-11a

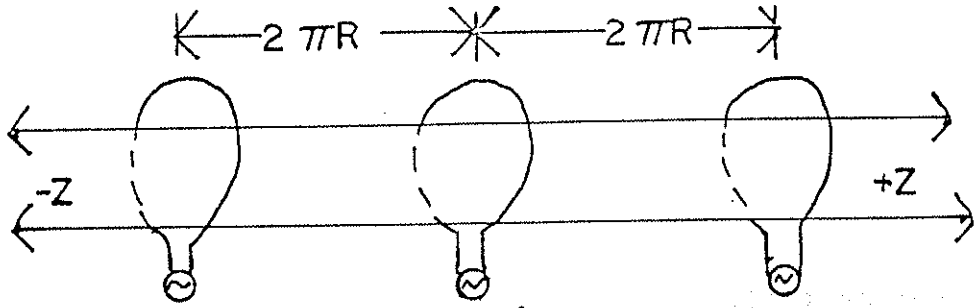

4-11b

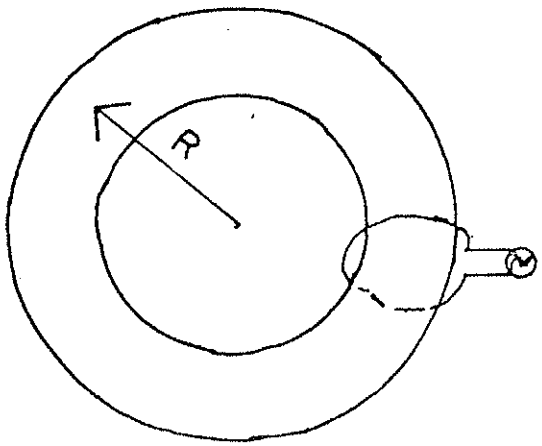

4-11c

shifted by the plasma an amount exp(-a+ib). The reason the contribution from the other antennae are twice as great than from the test antenna on itself is that its own back field is increasing linearly and so sees an average of only one half while the other antennae make a full contribution of the maximum value to the field. The nth antenna's contribution is $2E_o\exp(n(-a+ib))$, and the total contribution is:

$$E_{total} = E_o+2E_o \exp(n(-a+ib)) \qquad (4\text{-}17)$$

Summing this infinite series to get E_{total}, we get:

$$E_{total} = E_o\frac{1-\exp(-a)+2i\sin(b)\exp(-a)}{1-2\exp(-a)+\exp(-2a)} \qquad (4\text{-}18)$$

If we replace the infinite linear configuration with a closed torus containing a single antenna (figure 4-11c), the same formalism applies. The parameter a is then the attenuation of the wave due to absorption mechanisms in one transit of the torus, i.e. the number of times a wave transits the torus before its magnitude e-folds. Then b is the phase shift imposed by the propagating wave, $b = 2\pi m$, where m is the number of full wavelengths that fit around the torus, and is integral for an eigenmode, and half integral for an antimode. This back emf has both

real and imaginary components, corresponding to the resistance and reactance applied to the driving current. The real component E_r times the antenna current I is just the input power to the plasma. Additionally there is a reactive component E_i which may be represented in the series lumped component model shown in figure 4-12 as the voltage produced by the current flowing through a reactance of value X_p. The physical reason for this behavior is similar to that found in a resonant microwave cavity except that the waves are traveling rather than standing. If the wave is a little "fast" for instance, the induced voltage arrives back at the antenna before the current has returned to its initial phase, i.e. the phase shift is inductive. Formally integrating the electric field to get the back emf and dividing equation 4-18 by the instantaneous antenna current and separating it into its real and imaginary parts gives with a little algebraic substitution:

$$Z_{total} = Z_o \frac{\sinh(a)+i\sin(b))}{\cosh(a)-\cos(b)} \qquad (4\text{-}19)$$

Z_o is a real coefficient which for a given value of a is chosen to make $Z_{total} = r_s$ at $b = \emptyset$ giving $Z_o = r_s(\cosh(a)-1)/\sinh(a)$. Equation 4-19 clearly shows the

Figure 4-12.

Series equivalent tank circuit.

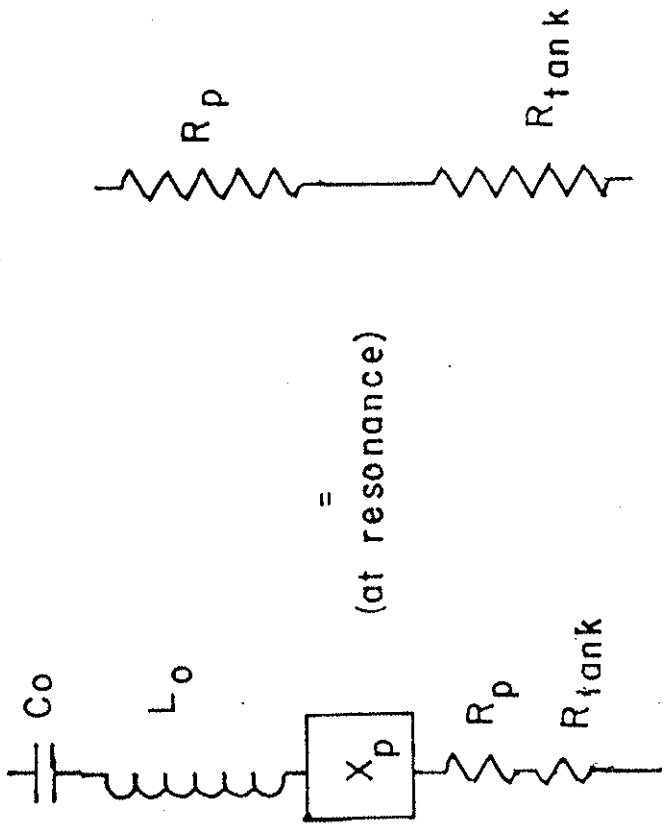
Rp
Rtank
=
(at resonance)
Co
Lo
Xp
Rp
Rtank

benefits of heating on an eigenmode. For a lightly damped fast wave the resistive series loading r_s is on a mode ~2/a larger than for a highly damped wave where a>>1. Fortunately r_s is strongly peaked on the mode, but it declines rapidly away from the mode center. The plasma reactance $|X_p|$ is zero on a mode, and highly peaked adjacent to the mode, decreasing more slowly away from the mode center. Figure 4-13 shows the relative widths of the resistive loading resonance as a function of a, while figure 4-14 shows the behavior of the reactive component.

The width of the resistive component is easily expressed in terms of the full width at half maximum:

$$b_{r_s}(\text{FWHM}) = 2\cos^{-1}(2-\cosh(a)) \qquad (4-20)$$

An analogous width based on the spacing between the two points where $|X_p|$ reaches a maximum may be defined as:

$$b_{x_p}(\text{FWHM}) = 2\cos^{-1}\left(\frac{1}{\cosh(a)}\right) \qquad (4-21)$$

We get the usual dependences for a resonant circuit in which the width is broader for increasing dissipation.

The concept that weaker damping produces a greater loading is somewhat contradictory and deserves some explanation. The reason for needing weak damping contains

Figure 4-13.

Eigenmode equivalent resistive loading.

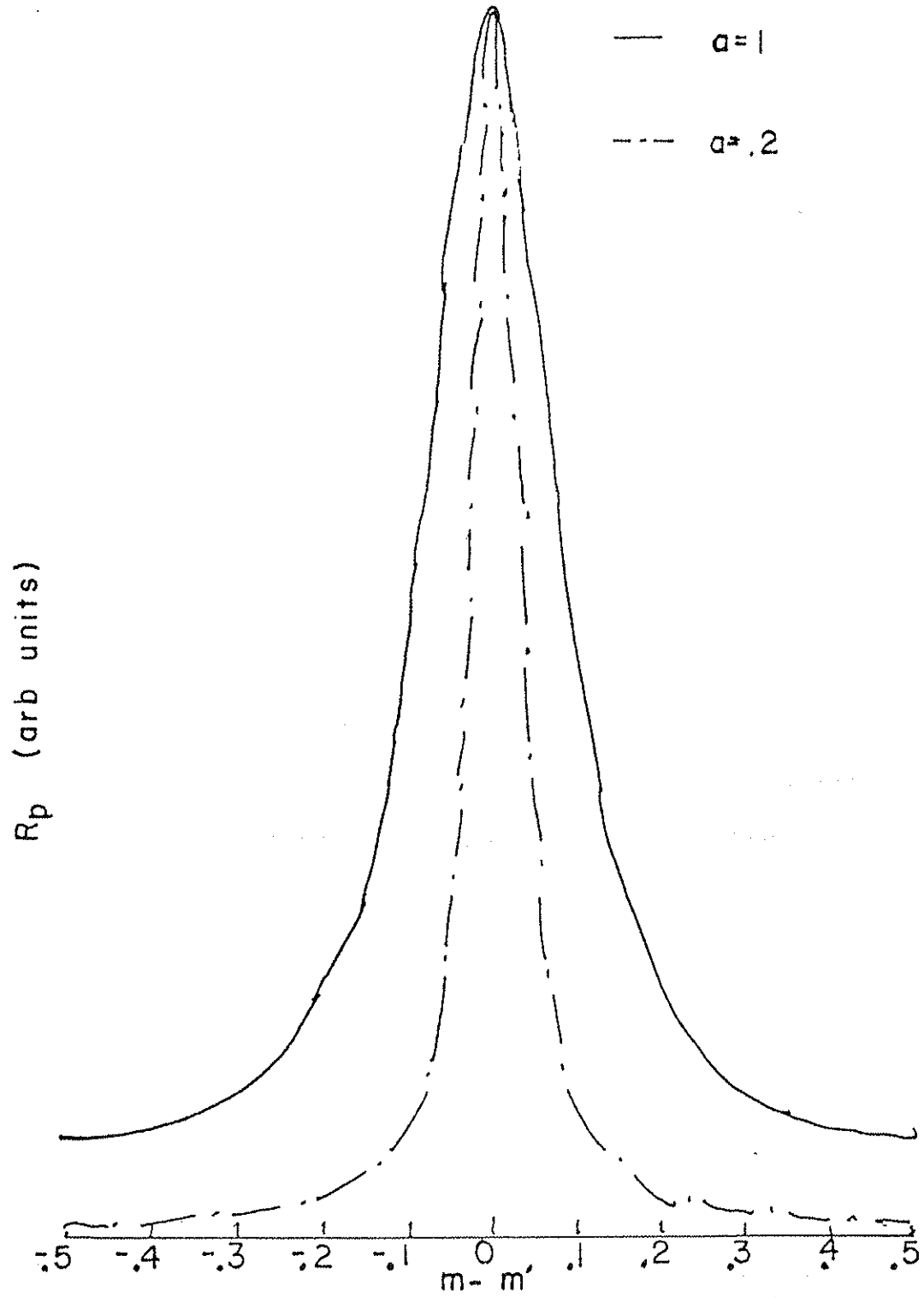
a=1
a=.2
R_p (arb units)
-.5
-.4
-.3
-.2
-.1
0
.1
.2
.3
.4
.5
m- m'

Figure 4-14.

Eigenmode equivalent reactive loading.

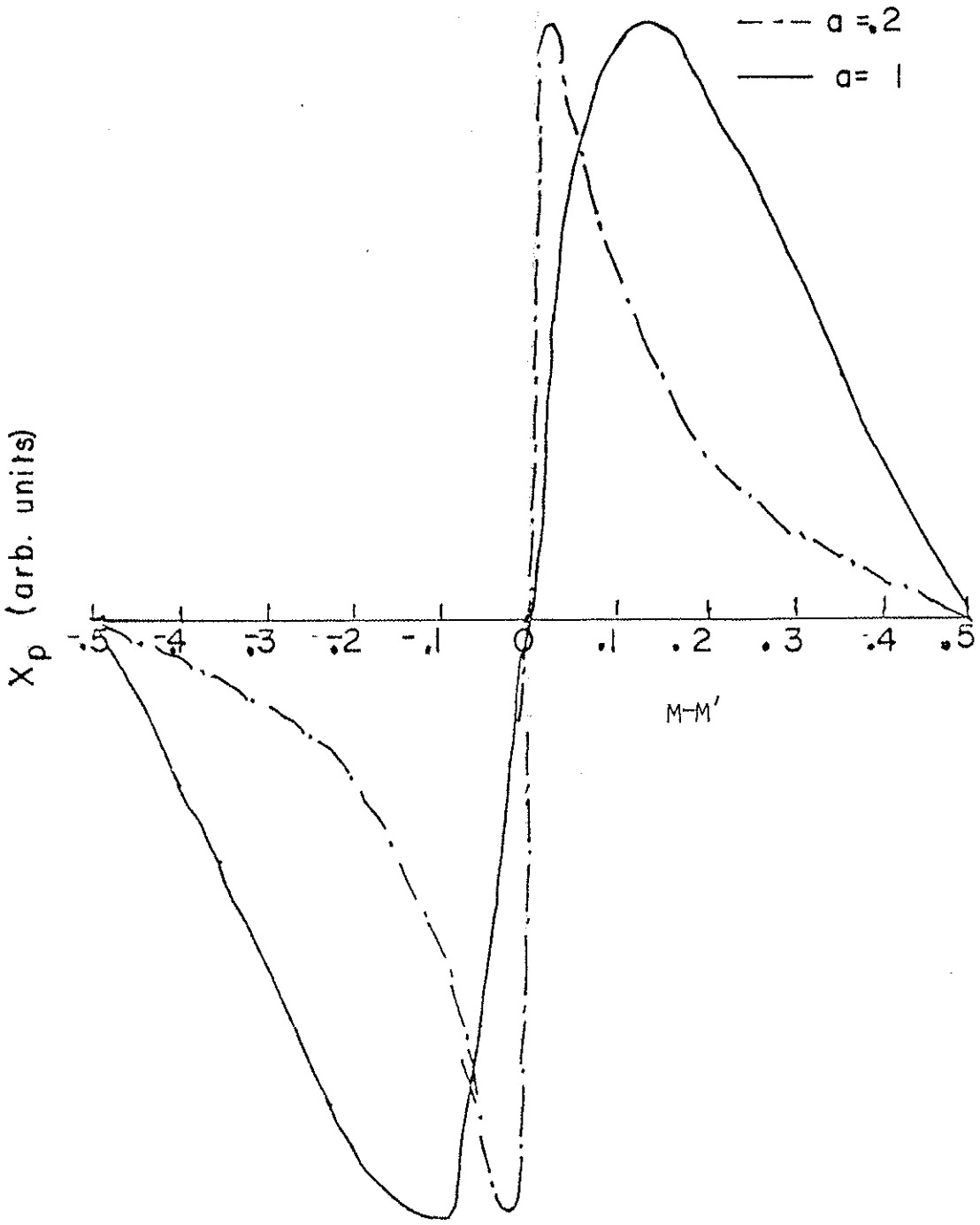
a = .2
a = 1
χ_p (arb. units)
-.5
-.4
-.3
-.2
-.1
0
.1
.2
.3
.4
.5
M-M'

two components, one involving pure physics and the other practical engineering. From a physics standpoint, weak damping implies that the entire plasma is essentially equally accessible to the wave. This allows the power to be distributed to all the resonance zones rather than being concentrated at only one section or near the antenna. An example would be the propagating slow waves which cannot reach the core for reasons already discussed. Power would have to be deposited near the edge.

One can then ask about an intermediate case with a = 2. The damping is still weak enough to heat the plasma uniformly but strong enough that the wave has a negligible effect on the antenna after one toroidal transit. For a large enough current in the antenna we can apply arbitrarily large amounts of power to the plasma. In practice we must be limited by the amount of voltage which may be applied to the coupling structure. Conceptually the advantage is easily seen from the parallel circuit model (figure 3-7) used in section III. Heavy loading corresponds to a small parallel resistance. We can write the loading resistance in terms of the series equivalent and express the power input as:

$$P = \frac{V^2 r_s}{X_o^2} \qquad (4\text{-}22)$$

where X_o is the usual value of the lumped circuit component at W_o. For a constant voltage, the power input is proportional to the series loading. Since a large a as discussed above represents an extremely hot plasma already at thermonuclear temperatures, we can now consider a more physical case of a lightly damped plasma which is being heated well off an eigenmode. Since the waves interfere destructively the fields in the plasma are smaller, the series resistance is lower, and the heating less. In all these cases the result of heating on an eigenmode is to reduce the effective parallel impedance seen by the rf source, i.e. an impedance matching to more physically realizable parameters.

Because of the desirability of using an eigenmode for power deposition, it would be advantageous to be able to adjust the driving mechanisms or even the plasma parameters to keep the rf source at the correct frequency for as long as possible. Various schemes have been proposed or applied, including both open and closed loop[28] feedback for shifting the rf source frequency, and even mechanically adjusting the limiter radius to resonate the

plasma column[26]. In this experiment we have an rf source whose frequency can be shifted by the plasma in a beneficial manner.

To study this effect, we will adopt a slightly simplified version of the fast wave dispersion relation, sometimes called the elliptical approximation[30]:

$$N_{||} = \frac{(1-N_{\perp}^2)\cdot 5}{(1+\frac{W}{W_{ci}})\cdot 5} \qquad (4\text{-}23)$$

This approximation (figure 4-15) differs from the more exact expression by overestimating $N_{\perp}$ by at most 10%. For simplicity we will also assume B_t and the plasma size are constant during the time of interest. Both assumptions are well satisfied in the experiment. All variations in the dispersion relation will be assumed to enter through density variations effecting the Alfven velocity, i.e. $|(dn/dt)/n| >> |(dB/dt)/B|$.

If the density and plasma column are sufficiently large there will exist instantaneously a W' such that if the rf source were on that frequency it would be driving an eigenmode with a parallel mode number m' an integer. The perpendicular mode numbers are assumed to be integral but otherwise arbitrary, and as they are much less

Figure 4-15.

Simplified dispersion relation.

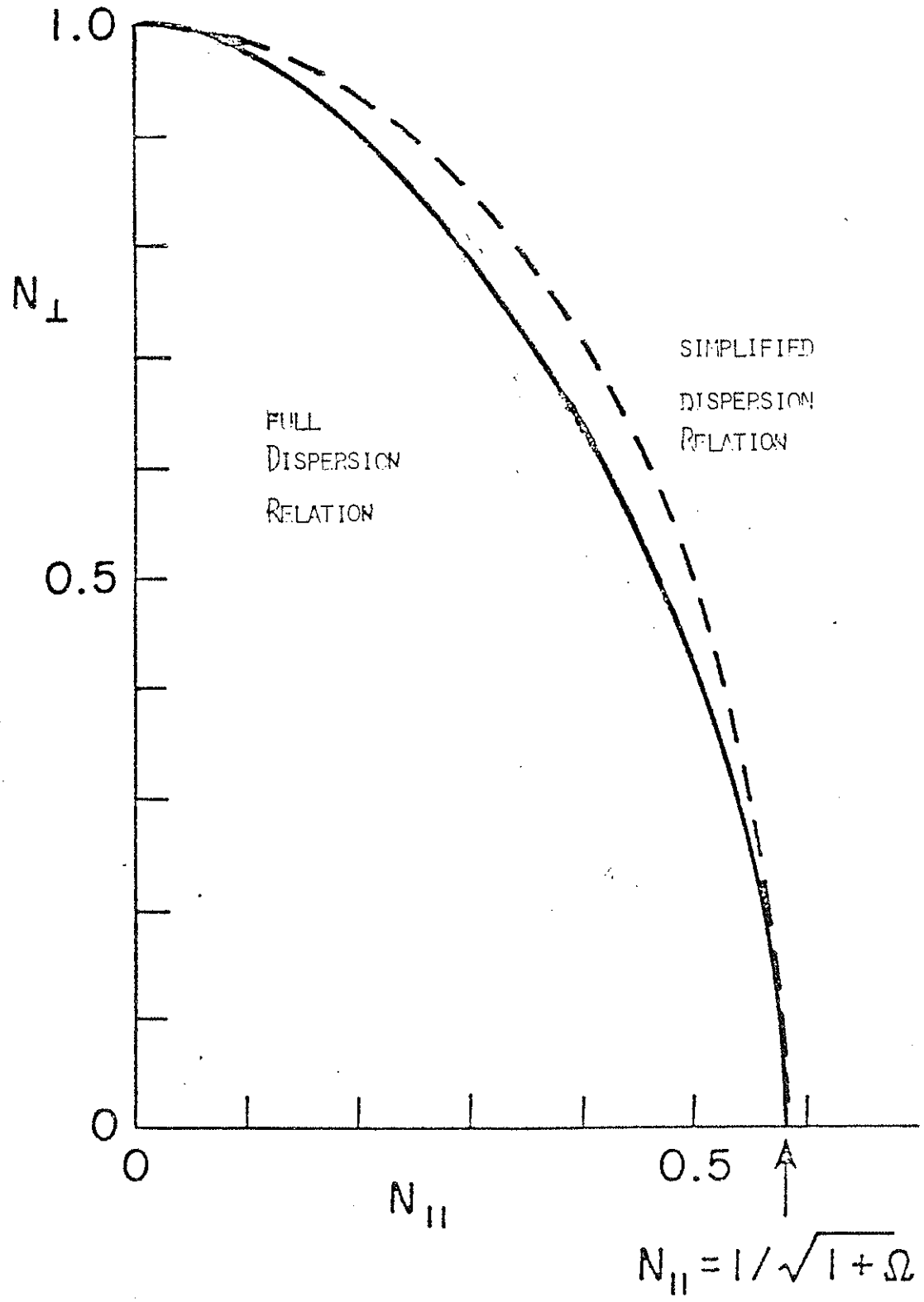
1.0
0.5
0
$N_\perp$
SIMPLIFIED
DISPERSION
RELATION
FULL
DISPERSION
RELATION
0
0.5
$N_{||}$
$N_{||} = 1/\sqrt{1+\Omega}$

sensitive to changes in plasma parameters, will be assumed constant throughout the experiment. The toroidal mode number m' is just the number of parallel wavelengths around the torus and may be written as:

$$m' = \frac{RW'}{V_{||}} \qquad (4\text{-}24)$$

A similar relation for the frequency w actually being excited is:

$$m = \frac{RW}{V_{||}} \qquad (4\text{-}25)$$

Hence:

$$m = m' \frac{WV'_{||}}{W'V_{||}} \qquad (4\text{-}26)$$

To eliminate the velocity dependence we invoke the dispersion relation equation 4-23 with V_a constant and arrive at:

$$m = m' \frac{W}{W'} \left(\frac{1+\frac{W'}{W_{ci}}}{1+\frac{W}{W_{ci}}} \right) .5 \qquad (4\text{-}27)$$

Now we have finally:

$$b = 2\pi(m-m') = 2\pi m'\left(\frac{W}{W'}\left(\frac{1+\frac{W'}{W_{ci}}}{1+\frac{W}{W_{ci}}}\right)^{.5}-1\right) \qquad (4-28)$$

which supplies the angular spacing between the actual and ideal mode frequencies. The sign of the induced reactance is such as to pull the rf source toward the ideal frequency. The rf source has a natural frequency $W_o = (L_oC_o)^{-\emptyset.5}$ in the absence of plasma. We may ignore the slight effect of the resistive component on the frequency since $r_s << X_o$. This is justified here but not necessarily so for a more heavily loaded experiment. Retaining the loading would result in the eigenmode resonance being slightly asymmetric. The presence of other modes far from W_o will also be ignored. They are widely separated in Tokapole II and have the effect of shifting W_o slightly[29]. We calculate the perturbed frequency by requiring the sum of the complex reactances to be zero:

$$X_{L_o}-X_{C_o}+X_p = \emptyset \qquad (4-29)$$

where X_{L_o} and X_{C_o} are the values of the lumped reactances in the tank circuit. This may be cast in a form normalized to the lumped reactance:

$$W = \frac{X_p W_o}{2X_o} + W_o \left(\frac{X_p^2}{4X_o^2} + 1\right)^{.5} \qquad (4\text{-}30)$$

By combining equations 4-19,4-28 and 4-30, we arrive at a nonlinear equation easily solved iteratively for W/W_o in terms of W'/W_o. Previously we have assumed V_a constant to look at the plasma at a fixed time. To calculate the change of W' to changes in density we define n_o as the density where $W' = W_o$, and n' the actual instantaneous density. Since at all times m=m', equation 4-26 becomes if $W = W_o$:

$$W' = W_o \left(\frac{1 + \frac{W'}{W_{ci}}}{1 + \frac{W_o}{W_{ci}}}\right)^{.5} \qquad (4\text{-}31)$$

Finally, again holding B constant, equation 4-29 becomes:

$$W' = W_o \frac{\frac{W^2}{W_{ci}} n_o}{2\left(\frac{W}{W_{ci}}+1\right)n'} \left(1+\left(1+\frac{4\left(\frac{W}{W_{ci}}+1\right)n'}{\left(\frac{W}{W_{ci}}\right)^2 n_o}\right)^{.5}\right) \quad (4\text{-}32)$$

Equation 4-32 is remarkably insensitive to B and is easily linearized over the range of validity.

In order to experimentally evaluate this theory, we need to know approximate values of Z_o and a. Both may be calculated theoretically[24,30], but the large vacuum region as well as the unusual field structures in Tokapole II prevent doing this to sufficient accuracy. The primary problem comes in calculating the contribution of the wave fields in the edge to the phase velocity. Rather than adjust the theory parameters to give physically reasonable results, it was decided to use the direct loading measurements for r_s.

The damping decrement a was evaluated by a technique proposed by Takahashi[30]. Instead of looking at the response of the antenna to its own wave, we place a small rf b_z probe into the edge of the plasma. The antenna current is also monitored directly by a Rogowski loop. For an antenna current I, a signal s proportional to I is detected at the probe from the first pass of the wave. For each additional wave transit there is an additional

contribution sIexp((n(-a+ib)) as before. This sum can be written as:

$$S_{total} = \frac{sI}{1-\exp(-a)\cos(b)} \qquad (4-33)$$

For n integral, the signal is real, on a mode, and produces a probe signal $S_r=sI/(1-\exp(-a))$. For n half integral, the signal is real, on an antimode, and is detected with a magnitude $S_a=sI_a/(1+\exp(-a))$. Defining $Y=I_aS_r/I_rS_a$, we can solve for Stix's a to get:

$$a = \ln(\frac{Y+1}{Y-1}) \qquad (4-34)$$

The assumptions for this approach are essentially the same as before giving hope that the same deviations from an ideal case will tend to cancel. The greatest deficiency is that the temporal spacing between the mode and the antimode is much greater than the width of the single mode. The assumption that the plasma profile and coupling are little modified between the two points is less well satisfied, but should nevertheless give a fair approximation of a. Figure 4-16 shows a typical case.

Figure 4-16.

Antenna current and rf b_z versus time.

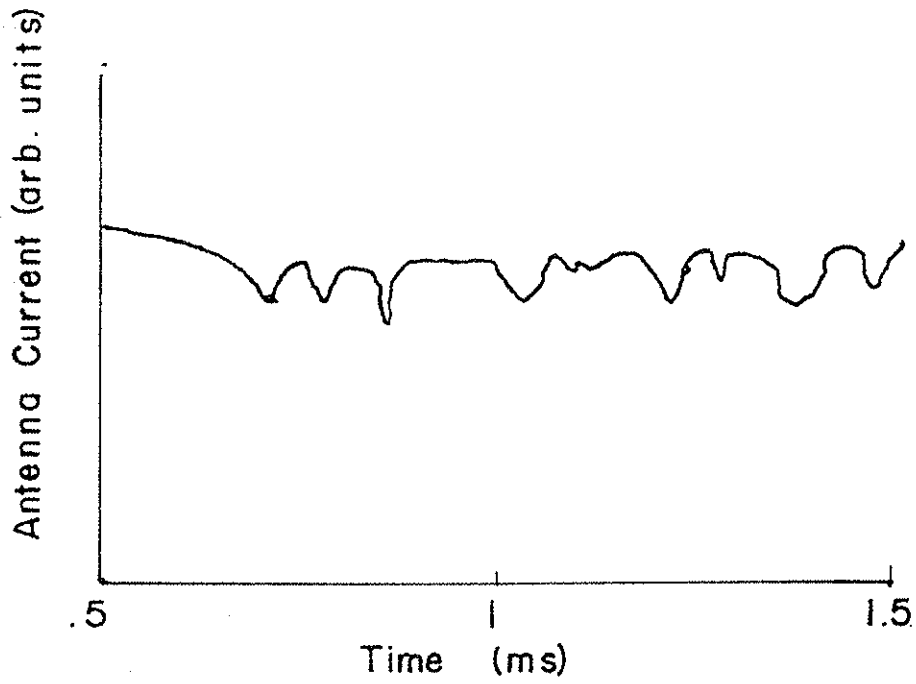
Antenna Current (arb. units)
.5
1
1.5
Time (ms)

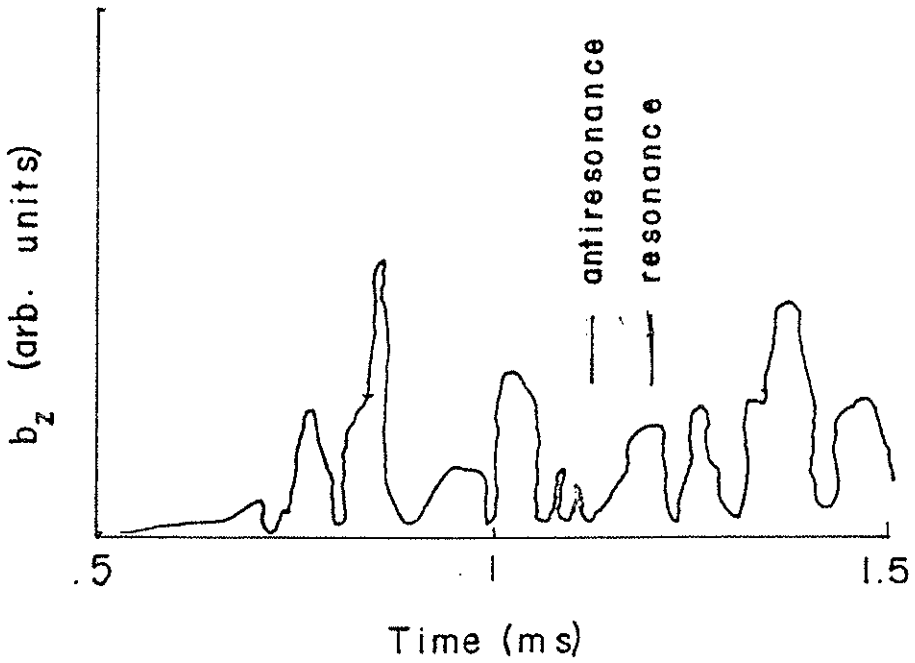
b_z (arb. units)
antiresonance
resonance
.5
1
1.5
Time (ms)

Figure 4-17 shows a versus location of the resonance zone. Taking a typical value of a for resonance as .2 and r_s as .5 ohms we can examine the agreement with the theory by measurement of the frequency shift magnitude, direction, and dependence on n.

For the heating zone in the plasma center, the theoretical frequency shift is shown in figure 4-18 along with the measured data from the phase locked loop frequency meter. Figure 4-18 represents a rising density. Plotted in figure 4-19 is a similar plot for a falling density at the end of the discharge. The qualitative appearance is the same, but the order of the frequency shift is reversed and the longer period reflects the slower rate of decay of the density in good agreement with theory. Finally, we may move the resonance zone toward the plasma edge where the damping is less. The magnitude of the frequency shift is a complex function hidden by this formalism, but the width between the two points of greatest frequency shift is independent of the actual loading. Figure 4-20 shows the agreement of the width with the measured a.

The effectiveness of the enhancement of the power deposition can be evaluated by comparing the ratios of the theoretical integrated series resistance over the passage of the mode with and without the tracking reactance. For

Figure 4-17.

Spatial dependence of damping decrement a.

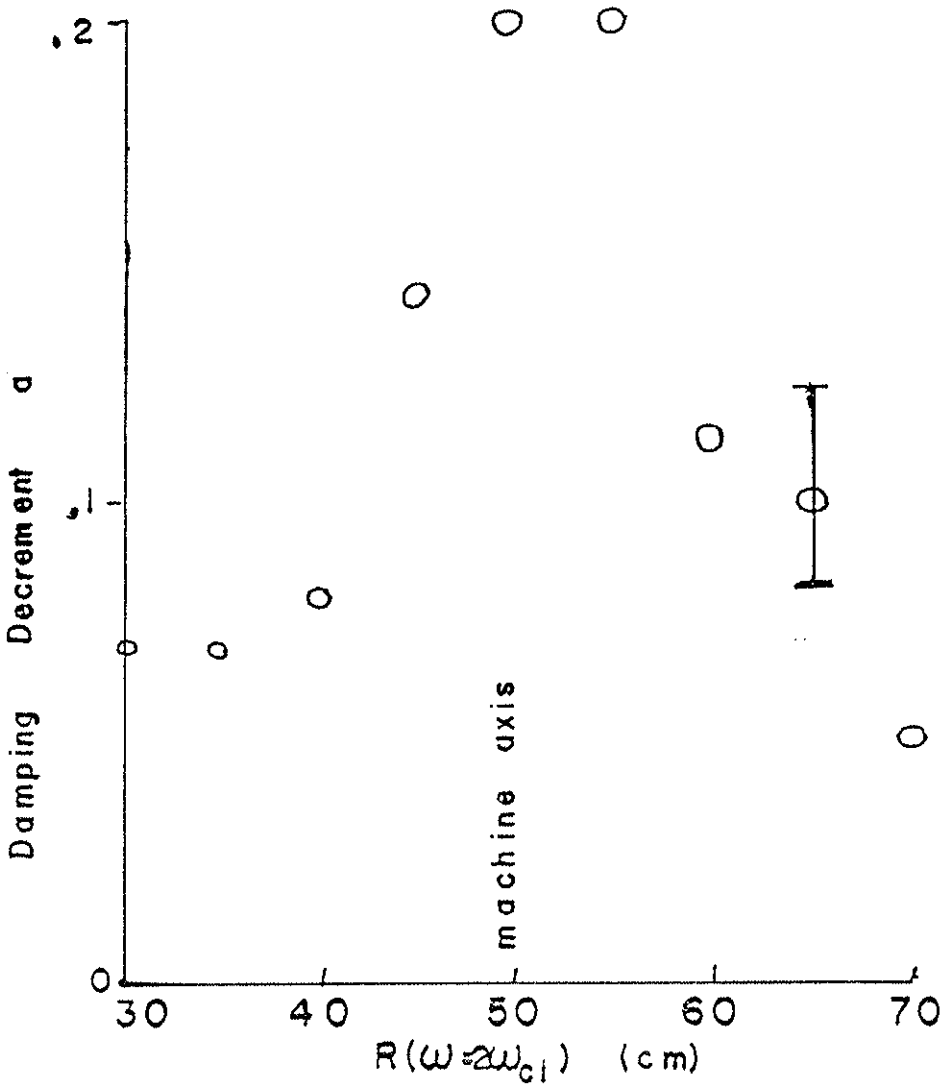
.2
.1
0
Damping Decrement α
machine axis
30
40
50
60
70
R(ω=ω_ci) (cm)

Figure 4-18.

Plasma induced frequency shift, rising density.

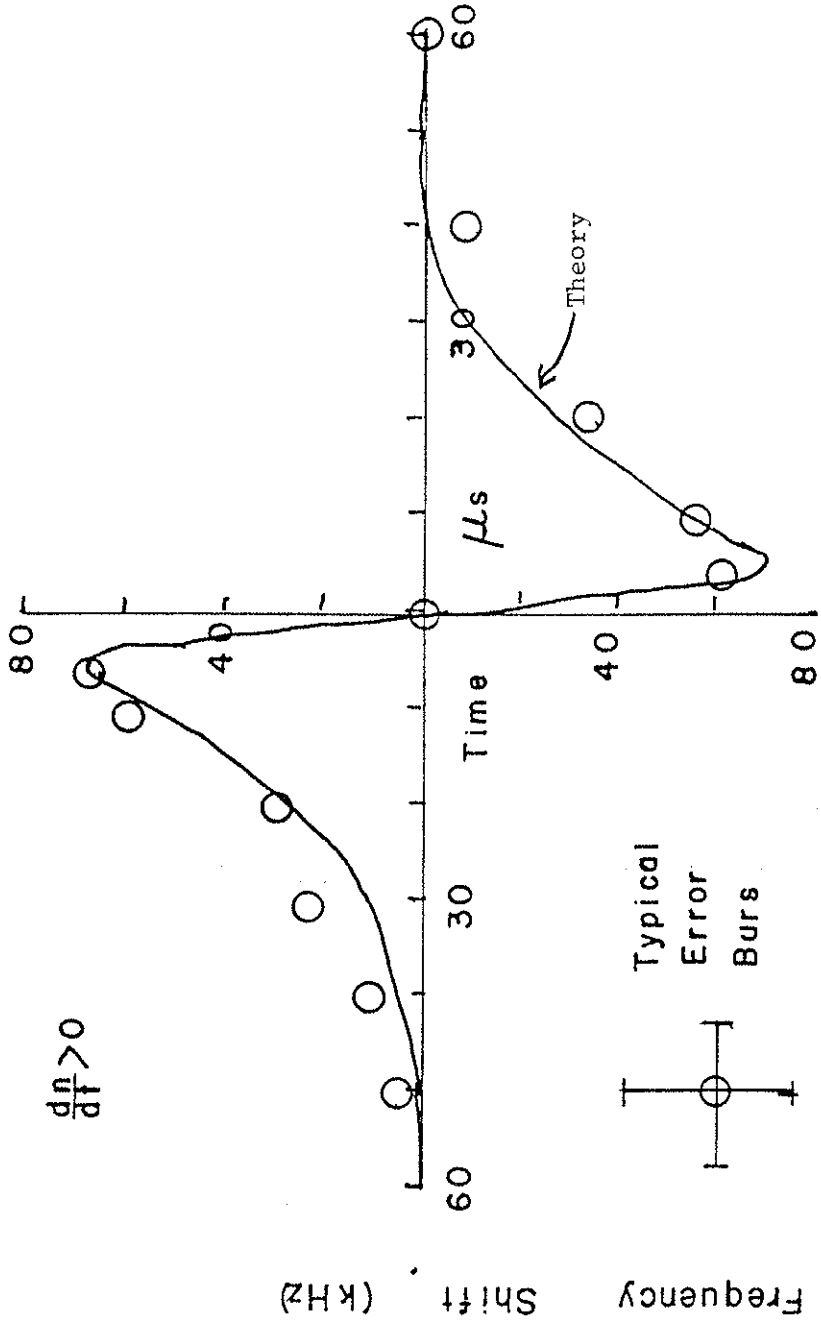
Frequency Shift (kHz)
60
30
0
30
60
80
40
0
40
80
Time
μs
Theory
Typical Error Burs
dn/df > 0

Figure 4-19.

Plasma induced frequency shift, falling density.

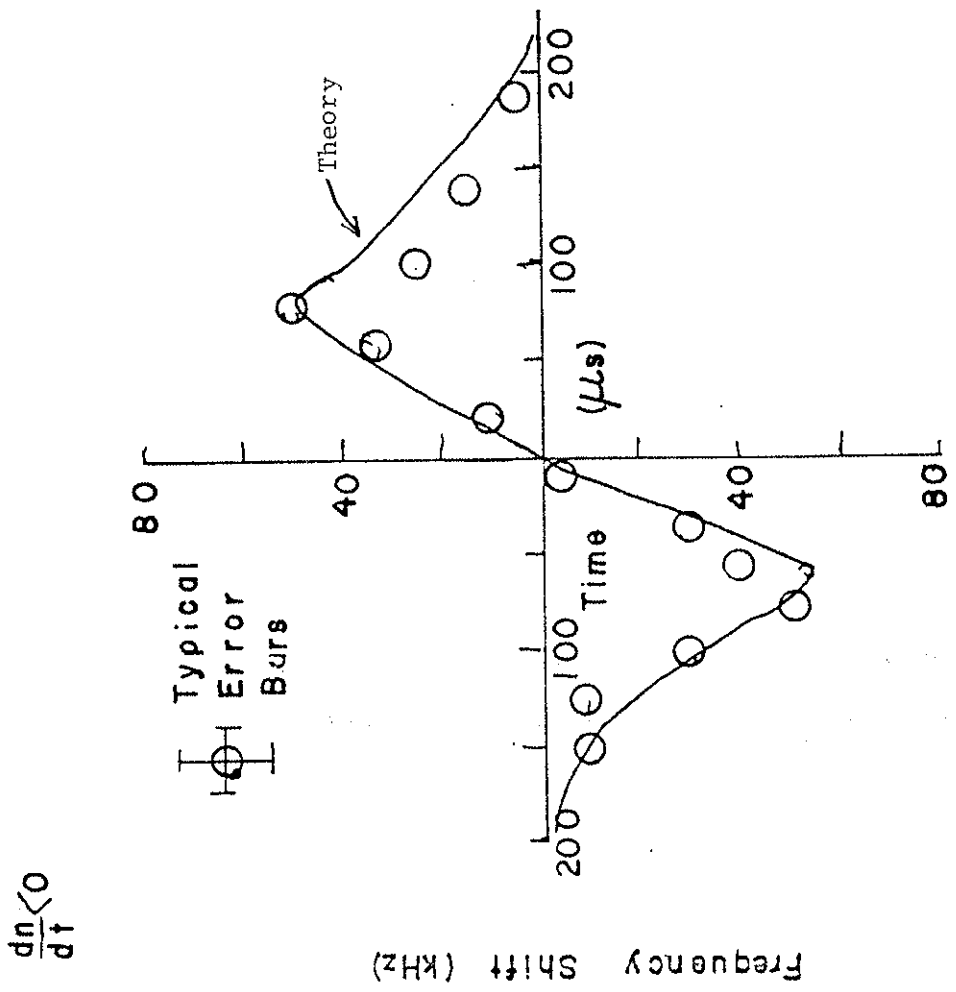
Frequency Shift (kHz)
Time (μs)
80
40
100
200
Theory
Typical Error Bars
dn/dt < 0

Figure 4-20.

Angular shift width vs damping decrement a.

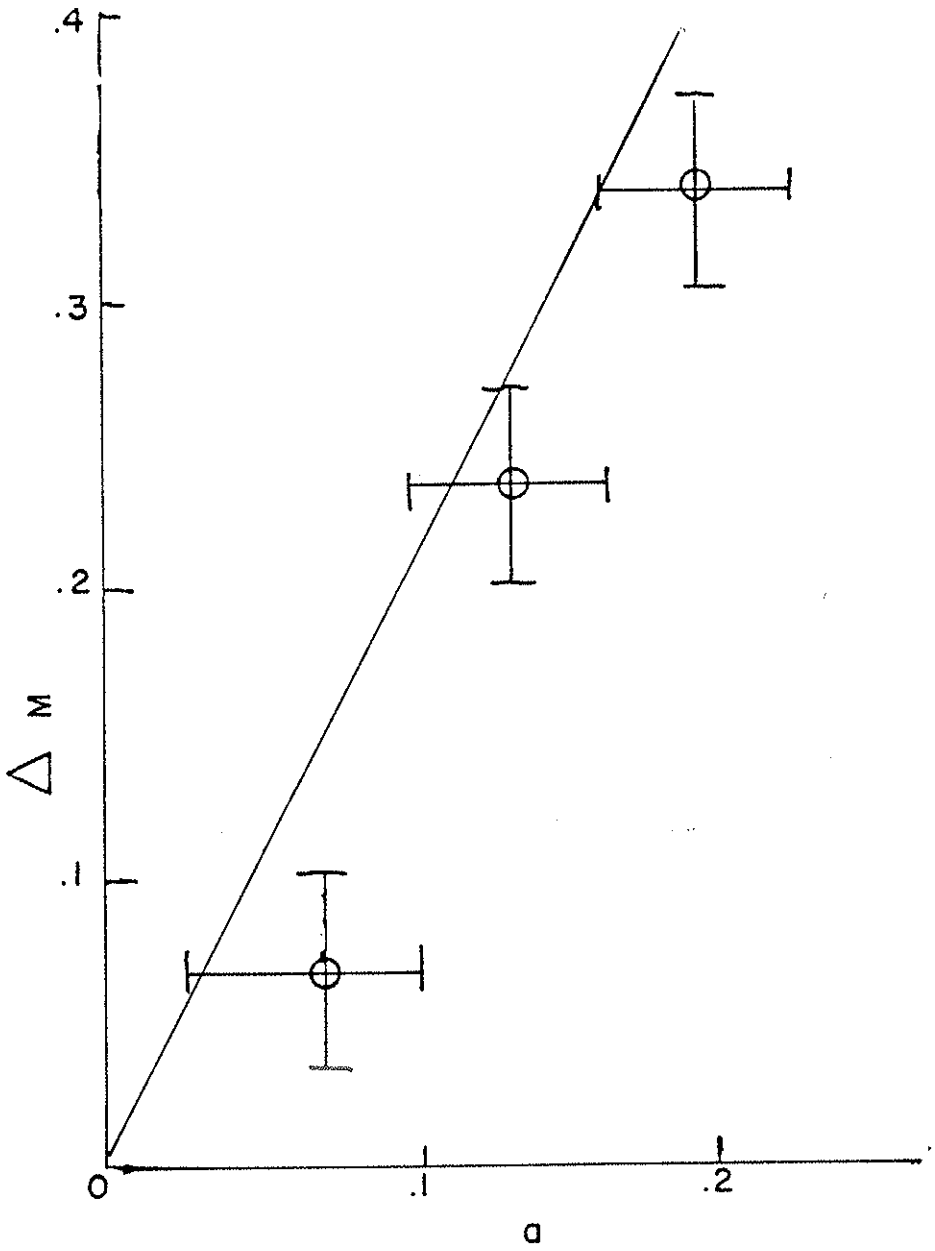
.4
.3
.2
.1
0
.1
.2
Δ M
a

this case it is probably better to concentrate on the narrow section of the mode where the tracking is most effective. We find for $.9<W'/W_o<1.1$ the ratio is 1.39. A 39% improvement in power deposition over the realistic tracking range is useful, but now let us examine the behavior of the tracking effect with various parameter changes. Holding all other parameters constant, we see that the tracking effect increases as the toroidal mode number increases. A change in $V_{||}$ is ~ m times more effective than for a single wavelength. Since the LHCP component decreases with increasing m, this effect is counter productive.

Changes in the plasma obviously effect the damping and loading, but we may conceptually decouple these two effects by considering changes in the damping as being due solely to changes in the ion temperature. Since both the damping decrement a and the loading in the absence of toroidicity go as T_i, we can hold these two in a constant ratio and examine the temperature effects on loading. The effects of the changes in r_s may be examined by holding the temperature constant and imagining adjusting the antenna to be more or less efficient. The results will be presented in generalized units where r_s is given in terms of its magnitude relative to a. Additional detail would be useless as both a and r_s are sensitive functions of the

plasma size, temperature, composition, and the launching structure. Additional details for the exact calculation of a and r_s for specific applications are covered in many papers, but most clearly in reference 30.

Figure 4-21 shows the behavior of the tracking with respect to increasing temperature. The tracking is relatively ineffective at very low and very high temperatures, but is relatively independent over a wide range of temperatures. The effectiveness increases monotonically with r_s. In practice the loading cannot be increased without limit due to restrictions on antenna size and coupling. Also, for sufficiently large values of r_s the induced reactive component is sufficient to dominate the lumped circuit components in the tank circuit and cause the oscillator to be unstable.

The use of such a circuit is seemingly ideal for the present generation of small and medium sized research devices. Significant gains in power input can be made with fewer components than would be required for a conventional oscillator-amplifier-coupler-antenna chain. Such a design does require individual construction though, and is not readily adaptable to frequencies above ~20 MHz because of the difficulty in supressing parasitic oscillations. For use in larger machines the active tracking techniques currently under development promise to

Figure 4-21.

Tracking heating enhancement vs damping decrement a.

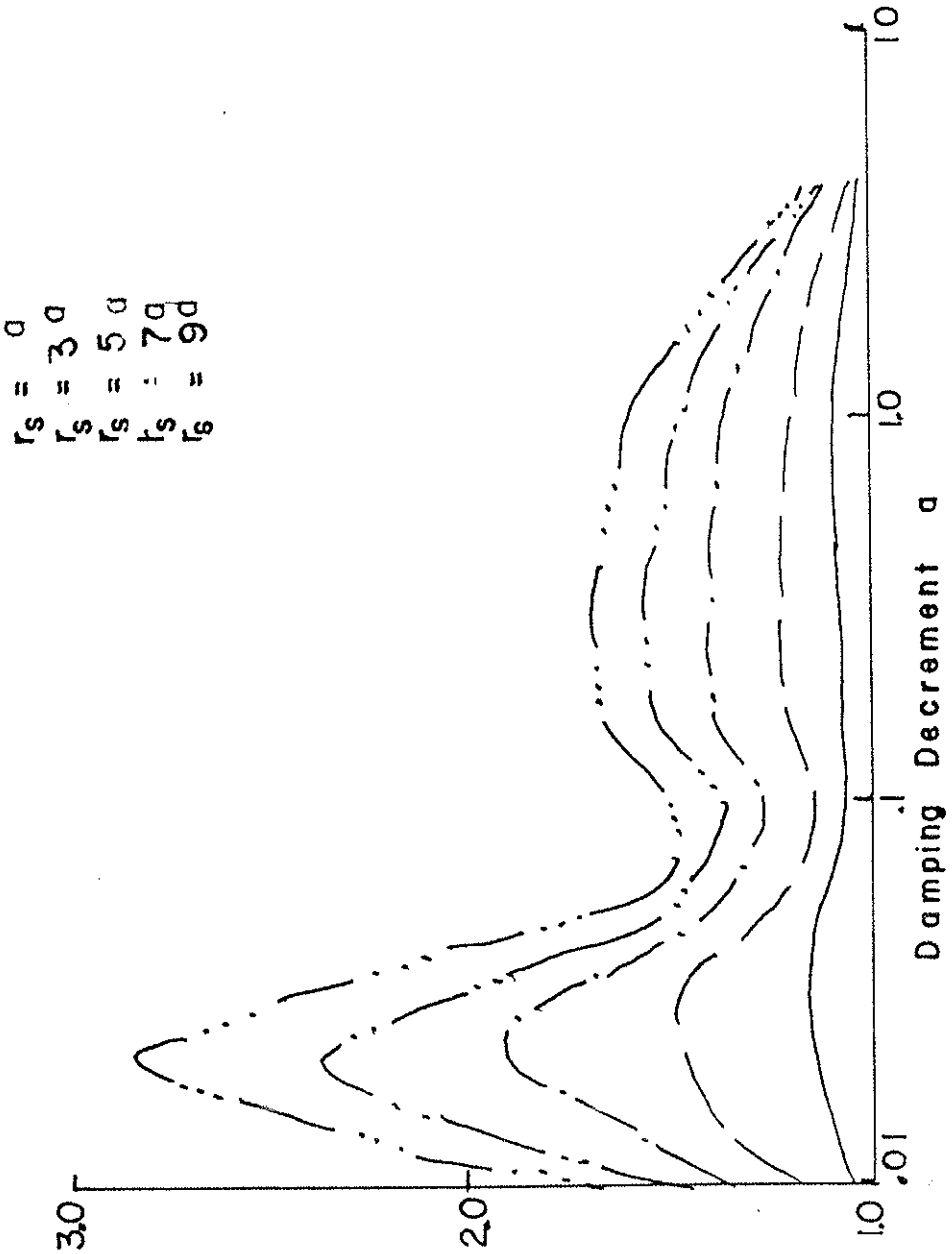

Power Deposited With Tracking/Power Deposited Without Tracking

allow tracking over much wider ranges. The density of modes for larger devices, however, would tend to frustrate tracking efforts due to their great number and close proximity to each other. Also, the presence of ion-ion hybrid resonances may greatly mask such effects, as would the resonant minority particles in a deuterium-tritium plasma. If the very formidable engineering problems could be overcome for making such a passively tracking rf source operate in a reactor frequency regime, this sort of tracking might again be useful. The high density of modes would provide a spectrum of closely packed modes which would not require great frequency excursions from W_o. $\Delta f/f_o$ for this experiment is $\simeq .006$.

V. ION HEATING THEORY AND CALCULATION

A. Ion Heating

Having demonstrated the existence of an rf field with significant LHCP we can now proceed to calculate the power deposited in the plasma ions. We start with the basic definition of power input as:

$$P_{abs} = \langle Re(\bar{J}\cdot\bar{E})\rangle \qquad (5\text{-}1)$$

Defining the effective dielectric tensor $\bar{\bar{K}} = \bar{\bar{U}} + \bar{\bar{\sigma}}/i\omega\epsilon_o$ where $\bar{\bar{U}}$ is the identity matrix and $\bar{\bar{\sigma}}$ is the normal conductivity tensor[20], we can rewrite equation 5-1 as:

$$P_{abs} = \frac{1}{4}(-i\omega\epsilon)\bar{E}^*\cdot(\bar{\bar{K}}-\bar{\bar{K}}^*)\bar{E} \qquad (5\text{-}2)$$

Noting that $\bar{\bar{K}}-\bar{\bar{K}} = 2i\bar{\bar{K}}^a$ where $\bar{\bar{K}}^a$ is the anti-Hermetian part of the dielectric tensor we get:

$$P_{abs} = \frac{\omega\epsilon E\cdot(\bar{\bar{K}}_a\cdot\bar{E})}{2} \qquad (5\text{-}3)$$

For a cold plasma the anti-Hermetian part is zero resulting in no power deposition. The warm plasma dispersion relation is complicated even when appropriate

approximations are made, but fortunately power absorption has been shown[30,31] to reduce to the more tractable and usable form:

$$\frac{P}{\text{unit vol}} = \frac{\sqrt{\pi} e W_{ci}^2}{k_{||} v_t}\left(\frac{k_{\perp}^2 v_t^2}{2W_{ci}^2}\right)(hn-1)\exp\left(-\left(\frac{W-hnW_{ci})}{k_{||} v_t}\right)^2\right)|E_+|^2 \quad (5\text{-}4)$$

where hn is the harmonic number W/W_{ci} and $V_t = (2kT_i/m_i)^{.5}$ in the ion thermal velocity for a Maxwellian distribution. Assuming that the field E_+ is kept constant, we see that three factors influence the power deposition. First, the exponential factor is negligible except in a narrow range where the magnitude of its exponent is smaller than unity. Since W_{ci} is a function of position dominated by the 1/R dependence of the toroidal field the width of this heating range is (figure 5-1) then:

$$\triangle x = \frac{2k_{||} v_t R}{hnW_{ci}} \quad (5\text{-}5)$$

where R is the machine major radius and the shear is assumed to be zero. Physically, the plasma is assumed collisional enough that particles lose their energy and phase information between passes through the heating strip. Each kick received by a particle passing through a

Figure 5-1.

Tokamak cyclotron resonance zone.

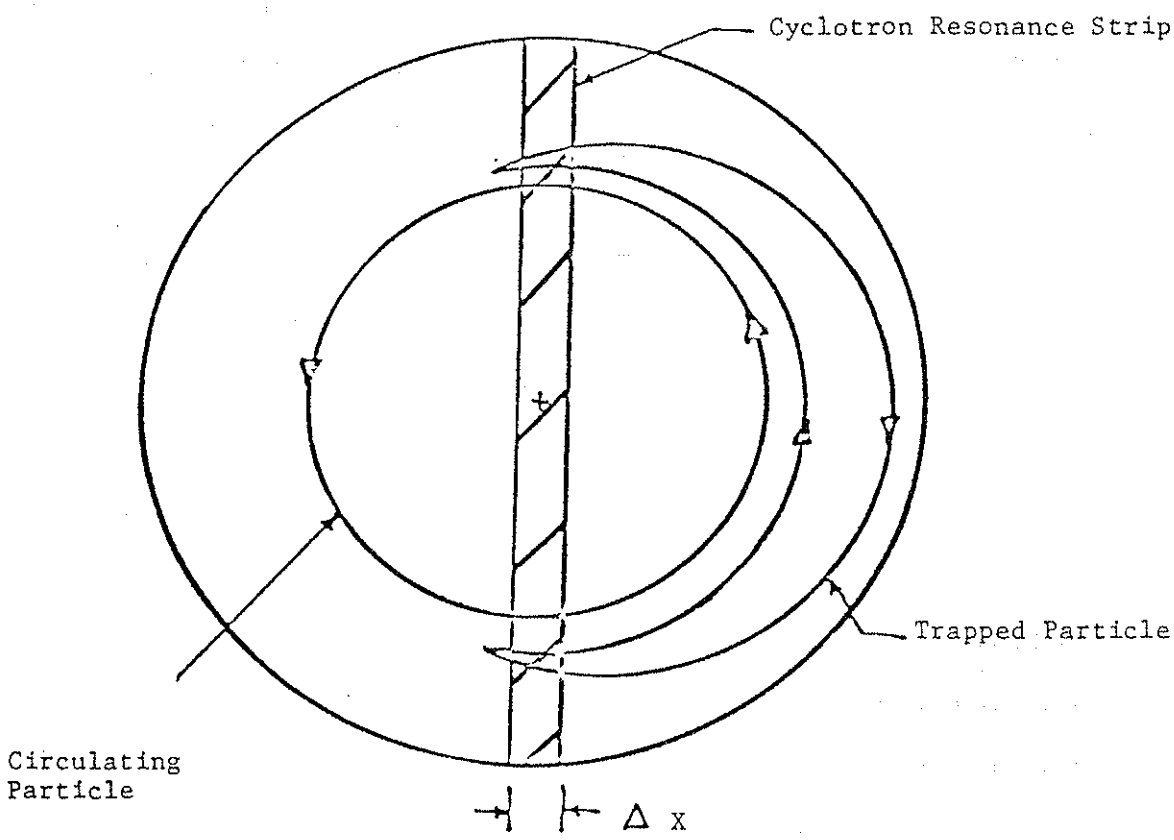
Cyclotron Resonance Strip
Trapped Particle
Circulating
Particle
Δ x

resonance zone may be considered random. Interestingly Stix[2] has demonstrated that the collisionless damping in a non-uniform B field yields the same results as the hot plasma theory usually used in detailed Fokker-Planck calculations. We see by equation 5-5 that the number of ions in the heating zone decreases with increasing harmonic number. Secondly, the finite gyro radius term $k_{\perp}^2 v_t^2/2w_{ci}^2 = .5(k_{\perp} r_L)^2$ where r_L is the ion gyroradius and is typically $\simeq .\emptyset 2$ for Tokapole II at hn = 2. It increases only linearly with temperature but decreases with B_t^2. Thirdly, it can be shown[6] that the heating strength is proportional to $J_m(k_{\perp} r_L)$. Since the first maxima of a Bessel function for $m > \emptyset$ occurs at progressively larger values of $k_{\perp} r_L$ with increasing m, the heating tends to produce tails at the expense of body heating. This is undesirable for both obvious physics reasons and the engineering fact that rf power becomes more expensive with increasing frequency.

By assuming $|E_+|$ is constant over the coupling zone width and integrating across the cross section of the plasma:

$$P_{total} = \frac{\sqrt{\pi}\epsilon w_{pi}^2 v_t^2}{8 w_{ci}^3} R r_p l_t \left(\frac{c}{k_{||} A} - 1\right)^2 w^2 b z_o J_m(k_{\perp} r_p) \quad (5\text{-}6)$$

where $l_t = 2\pi R$ and the other constants are as defined in section IV. For the few modes accessible in Tokapole II we can construct the table in figure 5-2. Calculation of the $m = \emptyset$ and the $m = +1$ normal case is straightforward because they follow the (relatively) simple theory presented in this section. The usual assumptions needed to calculate the wave coupling by the antenna to the plasma in the edge region may be bypassed since it was possible to measure directly the b_z field component. For the $m = +1^*$ case no such simple theory is available.

A curiosity of eigenmode heating is that while the series resistance reflected into the antenna is substantially higher than for the off-resonance condition for a given mode, that resistance decreases with increasing plasma temperature. This paradoxical result may be understood by realizing that the antenna behaves somewhat like a transformer with a variable turns ratio. Increasing the plasma temperature makes the plasma more dissipative, but it also decreases the amount of flux linking the primary resulting in a smaller impedance transformation. A simple derivation of this which bypasses the messy details may be made by noting that:

Figure 5-2.

Allowed mode values.

FIRST RADIAL MODE

n	$k_{\perp}$	$k_{\parallel}$	$N_{\perp}$	$N_{\parallel}$	$\frac{C}{k_{\parallel}A}$
m = +1					
4	19.4	8.Ø	.769	.317	1.533
5	16.3	1Ø.Ø	.645	.396	1.358
6	12.3	12.Ø	.486	.475	1.194
7	5.86	14.Ø	.232	.554	1.Ø41
m = Ø					
4	19.4	8.Ø	.765	.317	1.533
5	16.3	1Ø.Ø	.645	.396	1.358

$$P_{ICRF} = \frac{v^2}{r_s} = \frac{W^2\phi^2}{2r_s} = \frac{WU}{Q} \qquad (5\text{-}8)$$

where Φ is the wave flux through the antenna (primary), Q is the quality factor of the plasma, and U is the stored wave energy in the cavity. Solving for r_s we get:

$$r_s = \frac{W^2\phi^2 Q}{2U} \qquad (5\text{-}9)$$

Since both ϕ^2 and U are proportional to the square of the wave amplitude, only the Q term with its T_i^{-1} dependence survives. Hence the benefits of eigenmode heating are still substantial, but they decrease with increasing plasma temperature. In the case of a reactor this would be a factor of $\simeq 3$.

B. Electron Heating.

Using the same general technique as for the ions, Stix[2] has shown that when the phase velocity of the wave V_p is near the electron thermal speed V_{T_e} the electrons undergo transit-time magnetic pumping and electron Landau damping. These effects have been shown to be coherent with cross-terms. The transit-time and cross-terms exactly cancel with only the Landau damping surviving. The power to the electrons is one half that calculated for

the transit-time damping alone. Thus the power input density may be written:

$$\frac{P_e}{\text{unit vol}} = -\epsilon \frac{V_{T_e} W^2}{k_{||}} \left(\frac{W_{pe}}{W_{ce}}\right)^2 \exp\left(-\frac{V_p}{V_{T_e}}\right)^2 |b_z|^2 \qquad (5\text{-}7)$$

where W_{ce} and W_{pe} are the electron cyclotron and plasma frequencies respectively. For the estimated 50 eV electron temperature in the plasma with the antenna installed, $V_{T_e} \simeq 3 \times 10^6$ m sec^{-1} while $V_p \simeq 7 \times 10^6$ m sec^{-1}. In practice b_z peaks at the plasma edge where V_{T_e} is expected to be much lower, suggesting that power input to the electrons is negligible.

A reasonably unambiguous technique was evolved to detect electron heating. Spitzer[11] has shown that the resistivity of the plasma may be written as:

$$R_{Spitzer} = \frac{\pi^{1.5} m_e^2 Z e^2 c^2 \ln\Lambda}{2(2kT_e)^{1.5}} \qquad (5\text{-}8)$$

where $\ln\Lambda$ is a very weak function of the electron temperature and density and may be considered a constant. Since the resistivity is only a function of T_e and Z, any electron heating should be manifested in a reduction of

the resistivity and hence the loop voltage. Using a probe technique developed by Miller[32] and Shepard[33] we were able to measure the loop voltage across the entire plasma cross section. It was found that the ICRF did decrease the loop voltage when the rf was applied during the startup phase by allowing the plasma to form more quickly. After the plasma was started there was no difference in the loop voltage at the highest power levels applied until nearly one ms later when additional impurities which had diffused into the plasma had raised the loop voltage. No electron heating was detected at any radius.

VI. ION HEATING EXPERIMENTS

A. The Standard Experiment

The time evolution of the normal discharge with ECRH pre-ionizaton and the Mark II antenna installed is shown in figures 6-1 and 6-2. The gap voltage (part 6-1a) is used to drive the plasma current. The more conventional loop voltage on axis (part 6-1b) is measured[32] directly. B_t (part 6-1c) is allowed to reach its maximum near the peak of the ohmic heating voltage and is then crowbarred. The plasma current (part 6-1d) rises quickly and is relatively stable for a period of $\simeq$ 1 msec. The ohmic heating power (part 6-2a) is substantially above that of conventional tokamaks due to the high plasma resistivity. The ICRF power (part 6-2b) is only shown here in an illustrative manner and will be discussed in detail in section VIB. The electron density (part 6-2c) is only shown for the normal discharge without ICRF and after the rf pulse since the rf disables the interferometer. The 10 kW X-band (part 6-2d) is used to provide preionization for the ohmic heating. Not shown is a 100 watt S-band (2.45 GHz) source which is on throughout the experiment. The normal filling pressure is $\simeq$ 3 x 10^{-4} torr with the gas triggered 16.67 msec before the poloidal gap voltage and with late gas puffing to hold up the density triggered at

Figure 6-1.

Typical experimental parameters (I).

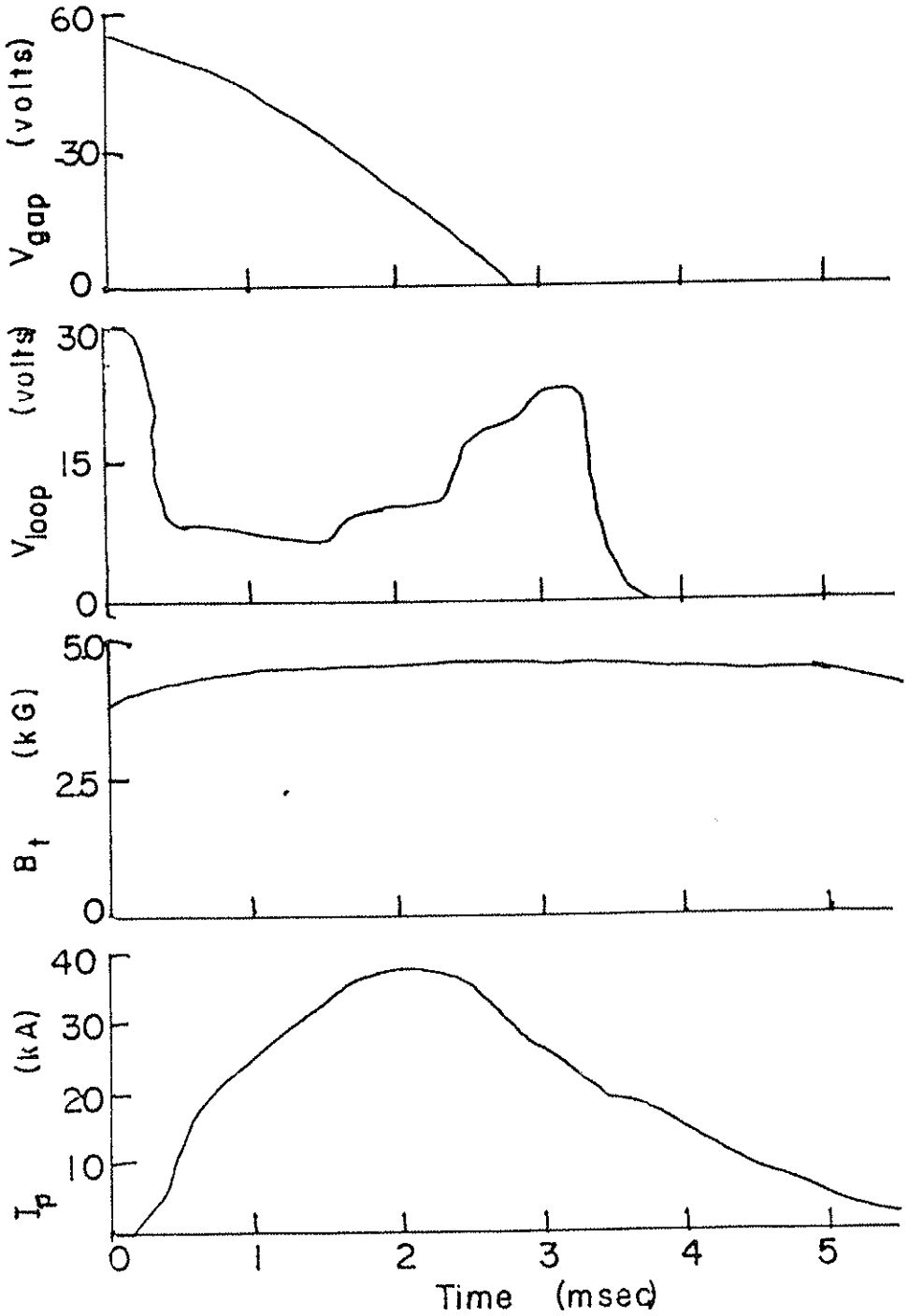
60
30
0
V_{gap} (volts)
30
15
0
V_{loop} (volts)
50
25
0
B_t (kG)
40
30
20
10
I_p (kA)
0
1
2
3
4
5
Time (msec)

Figure 6-2.

Typical experimental parameters (II).

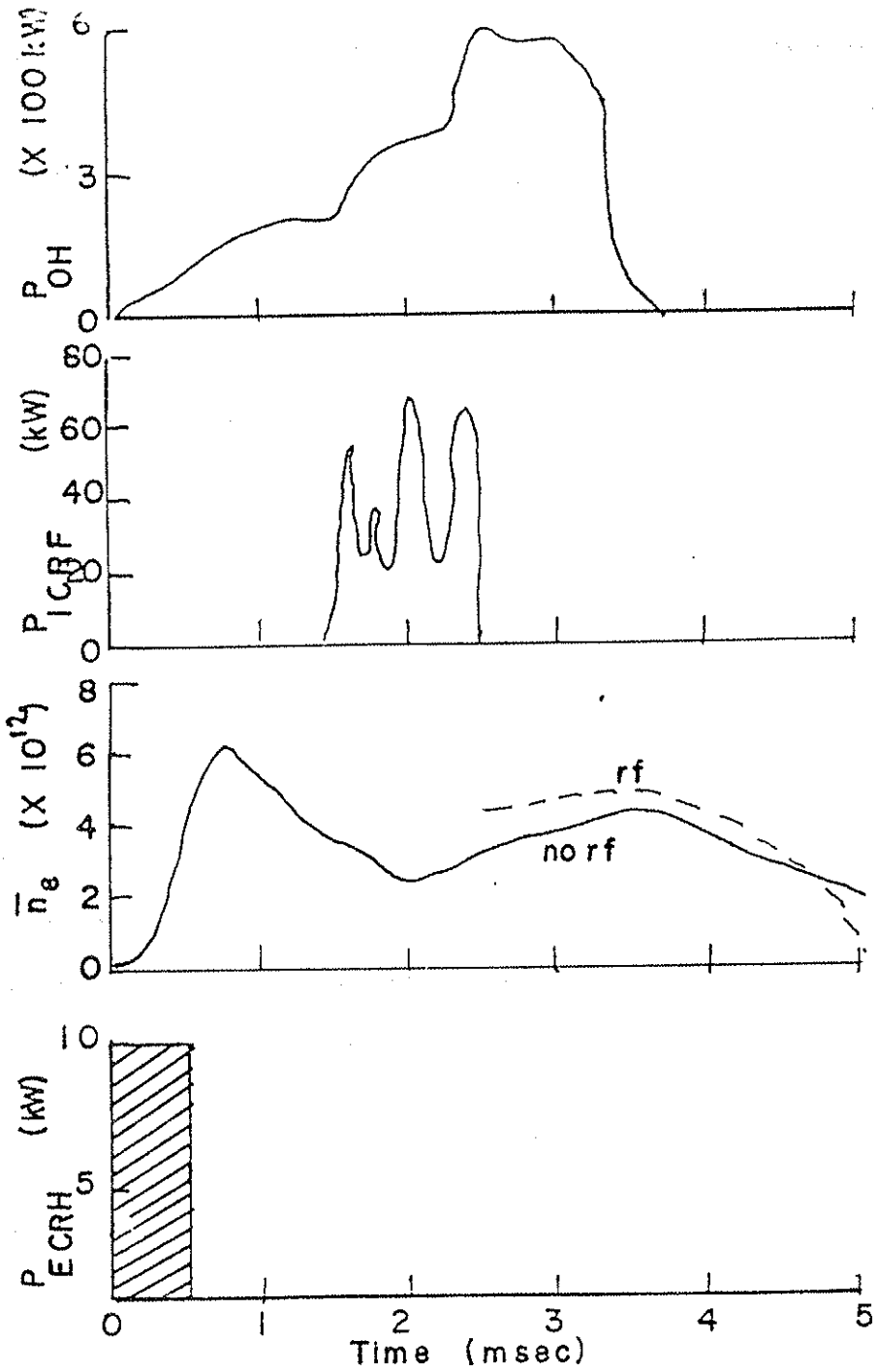
P_{OH} (X 100 kW)
6
3
0
P_{ICRF} (kW)
80
60
40
20
0
$\bar{n}_e$ (X 10^{12})
8
6
4
2
0
rf
no rf
P_{ECRH} (kW)
10
5
0
1
2
3
4
5
Time (msec)

1 msec after the ohmic heating voltage is applied. The plasma density, current, and discharge length are approximately a factor of 2 below those obtained with the antenna retracted in the normal discharge. Part of the performance is regained by increasing the ohmic heating voltage 25%. Similar problems exist with the use of other types of baffles indicating significant current flowing beyond the magnetic limiters. The electron density increase with rf is at least partly due to impurity influx from the walls and especially the copper hoops.

B. Antenna Loading

The definitive test of the heating theory in section V comes from a comparison of the power deposited in the ions as measured at the rf source with the power computed from the measured rf fields with equation 5-6. In order to make this comparison, several factors must be considered in the loading measurements made using the method of section IIIC. There are other sources of loading which can mask the eigenmode loading on the rf source. The early Mark IIa antenna showed an essentially constant loading at $\simeq$ 1300 ohms independent of the toroidal field and all plasma parameters except the density. The loading, but not the heating, scaled roughly linearly with density. While significant plasma heating and wave generation occured, it was impossible to see

clearly increases in loading due to the presence of eigenmodes (figure 6-3a). The addition of a Faraday shield reduced the background loading by a factor of ≃ 2.5, and for the first time made clearly visible the enhanced eigenmode loading (figure 6-3b) in the dc drive current I_{DC} (figure 2-2) from the power supply to the oscillator.

This additional background loading comes from two sources. The primary source is the "parasitic loading" caused by the presence of plasma in the near field around the antenna. Particles are electrostatically accelerated into the antenna depositing their energy as heat and/or by sputtering off impurities. The second source is the normal cyclotron heating in the evanescent Å field present around the antenna even when the density is too low for wave propagation. This mode was used in the earliest small machines such as the Model C Stellarator which were too small for propagating modes[2]. The limited space and other mechanical considerations on the antenna made construction of a truly efficient Faraday shield such as used in TFR[33], ATC, or PLT difficult. The residual loading remaining after the installation of the Faraday shield is understandable in terms of the electrostatic fringe field that leaks out through the gaps in the shield and the significant plasma density expected at the

Figure 6-3.

(a) I_{DC} vs time for the Mark IIa antenna.
(b) I_{DC} vs time for the Mark IIb antenna.

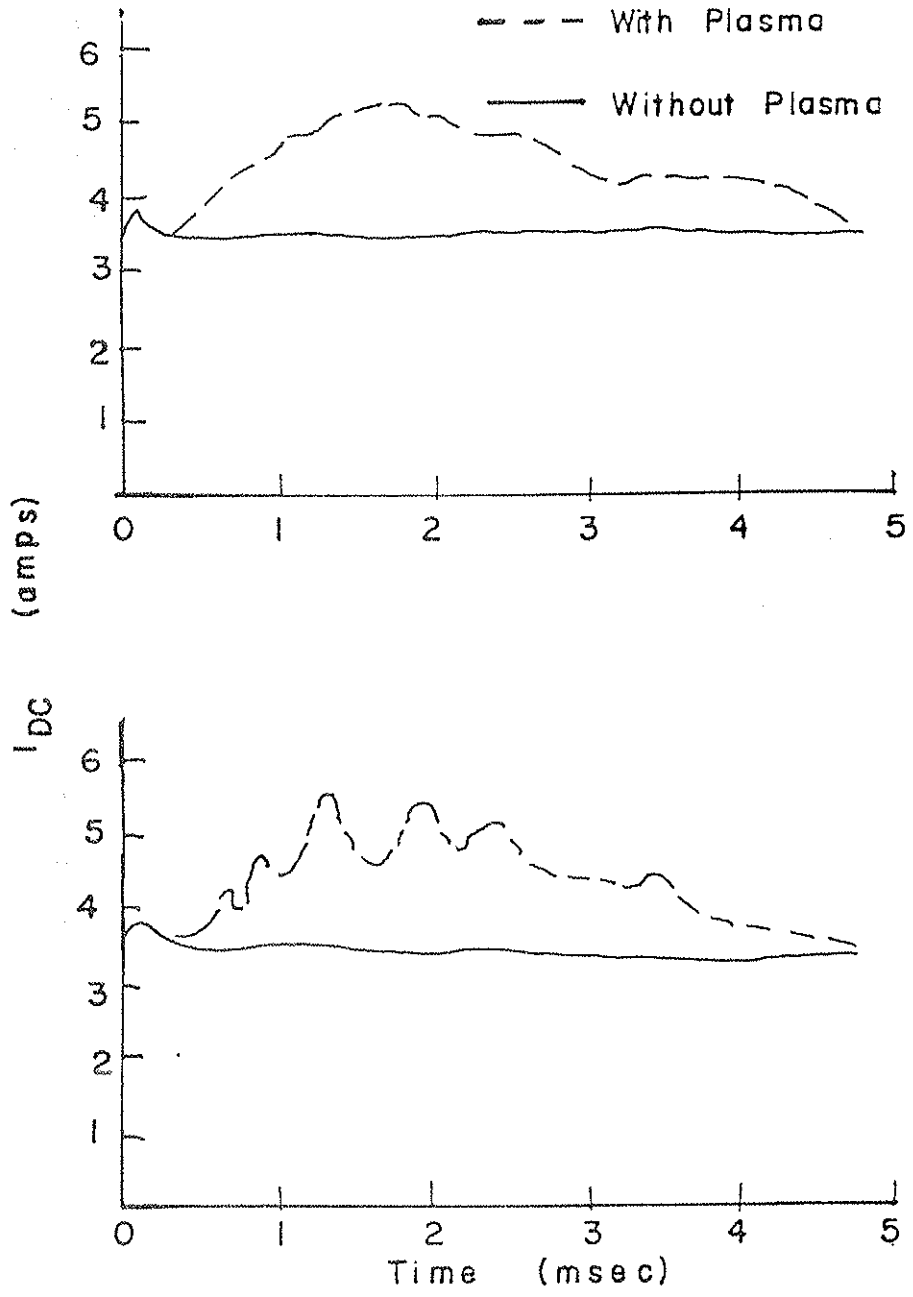
With Plasma
Without Plasma
I_{DC} (amps)
0
1
2
3
4
5
6
Time (msec)

unshielded bottom of the antenna as well as in the evanescent zone heating.

In order to separate the sources of loading, the model of figure 3-7 will be used with the plasma further divided into two parallel resistors $R_{eigenmode}$ and $R_{background}$. These may be experimentally resolved by noting from rf field measurements that the fields are down a factor of ~ 20 away from the antenna during the time of interest in the absence of an eigenmode and by assuming that all the loading immediately adjacent to the loading peaks is purely backgound loading. The loading measured on a peak is just the parallel sum of the background and eigenmode loading. The pure eigenmode ion loading is then calculated from the standard parallel resistor formula.

By combining the loading measurements with the rf field measurements we can identify the power input from the 3 types of modes in Tokapole II (figure 6-4). The agreement is reasonably good. The higher loading than predicted from the actual wave field probably comes from the crude model used which ignores edge heating, profile effects, and wall loading. The decrease in loading with increasing T_i is consistent with the T_i^{-1} dependence of eigenmode heating (figure 6-5).

Figure 6-4.

Measured vs calculated ion power input for the m = Ø and m = +1 modes.

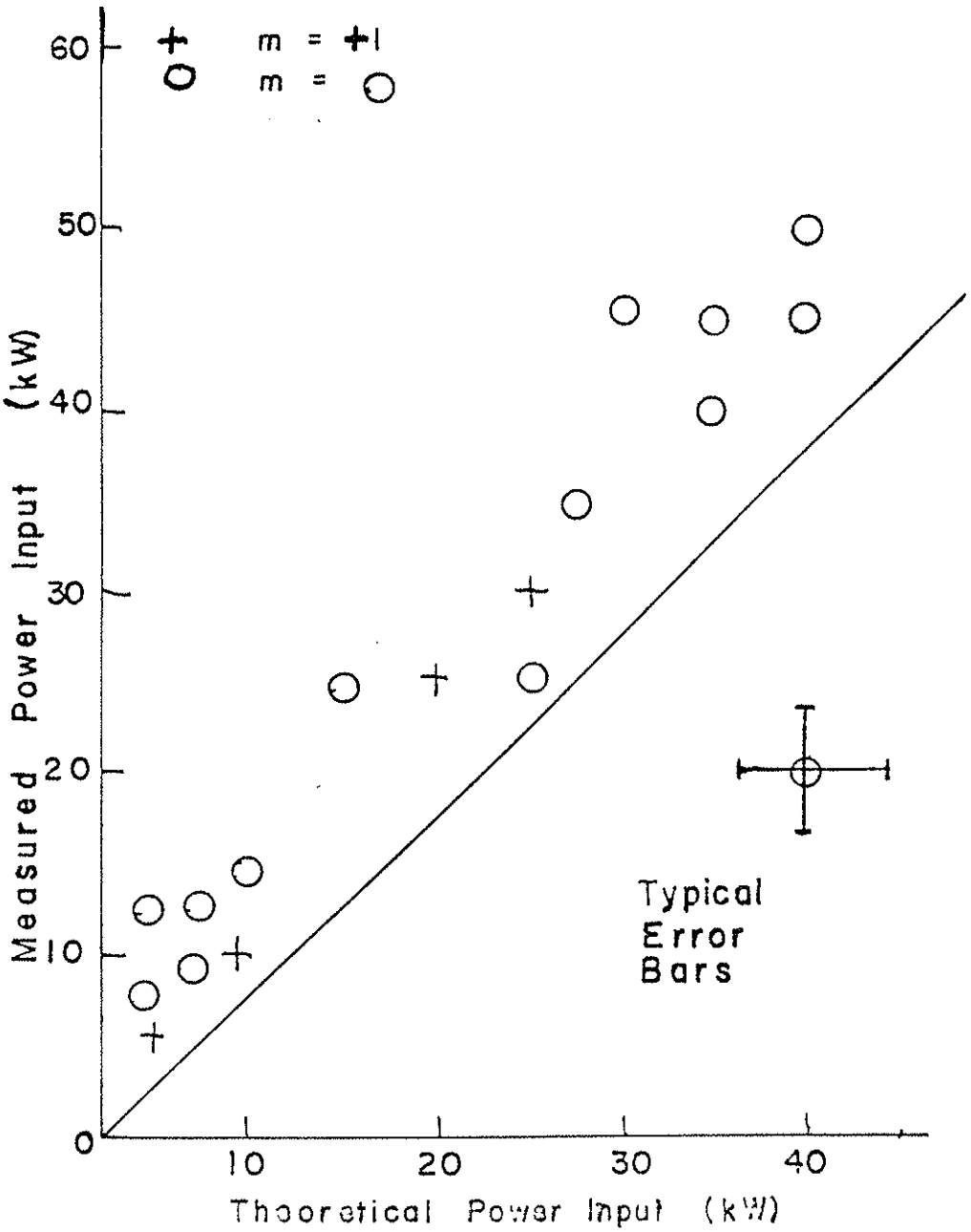
m = +1
m = 0
Measured Power Input (kW)
Theoretical Power Input (kW)
Typical Error Bars
0
10
20
30
40
50
60

Figure 6-5

Dependence of the m = Ø mode loading on T_i.

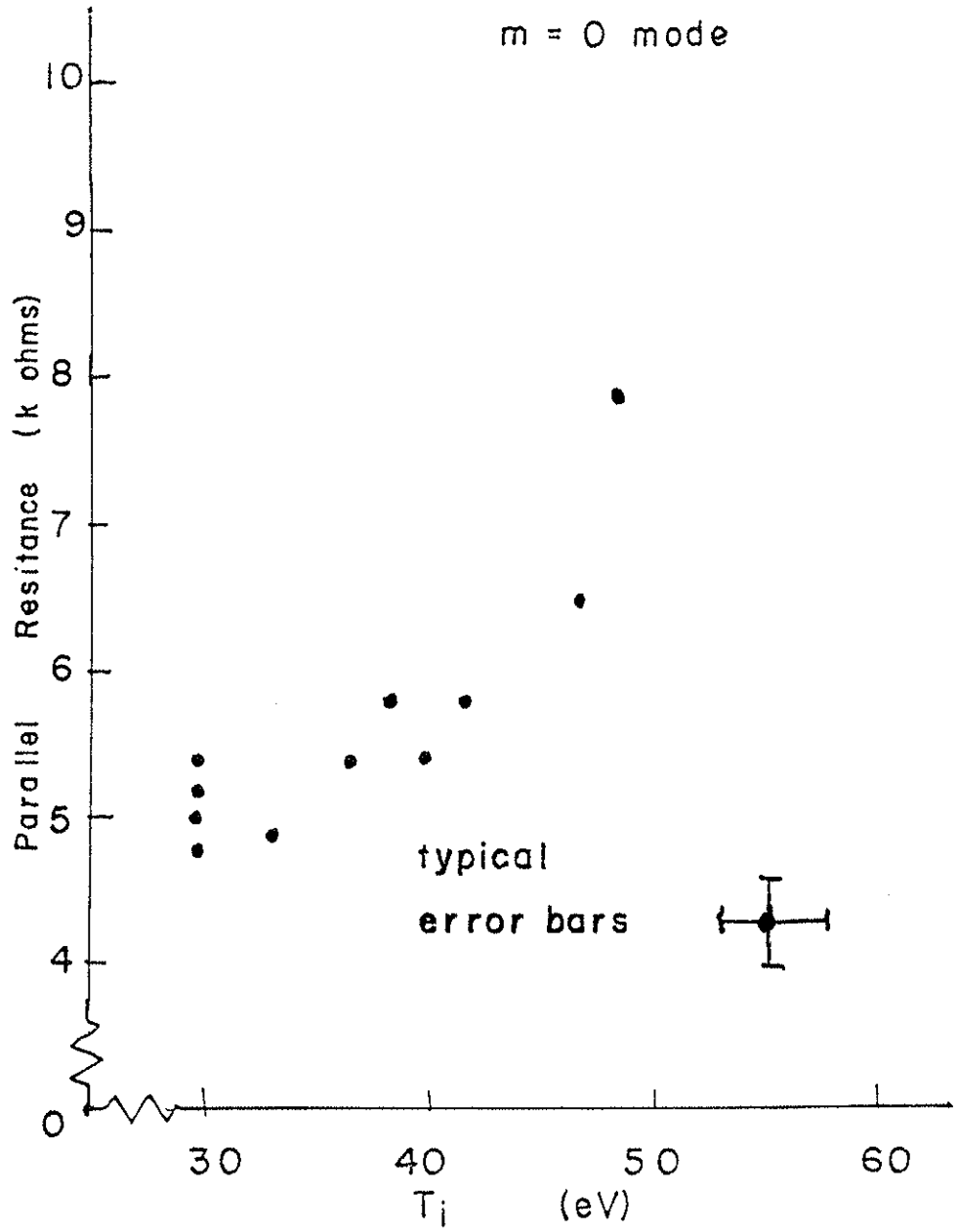
m = 0 mode
Parallel Resitance (k ohms)
10
9
8
7
6
5
4
0
typical
error bars
30
40
50
60
T_i (eV)

C. Ion Energy Distribution

The charge exchange analyser enables the resolution of non-Maxwellian distributions not easily detectable with Doppler techniques. A typical ion velocity distribution is shown in figure 6-6 for both the purely ohmically heated and rf supplementary heated cases. This two-component distribution in the rf case is typical of heating schemes which preferentially heat more energetic particles[2,21]. Experimentally the tail constitutes about 8% of the particles in the hottest plasma obtained. The body temperature must be regarded with some caution because charge exchange measurements were made in the 100-400 eV range which is far out on the distribution for a temperature of <100 eV where statistics were relatively poor. The break near 2 keV is consistent with particles being lost through loss cones caused by poorly confined particles on banana orbits.

D. Ion Heating Parameter Variation

Normal operation with $W = 2W_{ci}$ on axis placed the fundamental and third harmonics completely outside the plasma column. A crude demonstration of this heating can be seen in figure 6-7. The line average density of Cu I was measured spectroscopically with different toroidal fields on axis. The enhanced copper radiation is assumed to be due to energetic ions or charge exchange neutrals

Figure 6-6.

Typical ion energy distribution from charge exchange measurements.

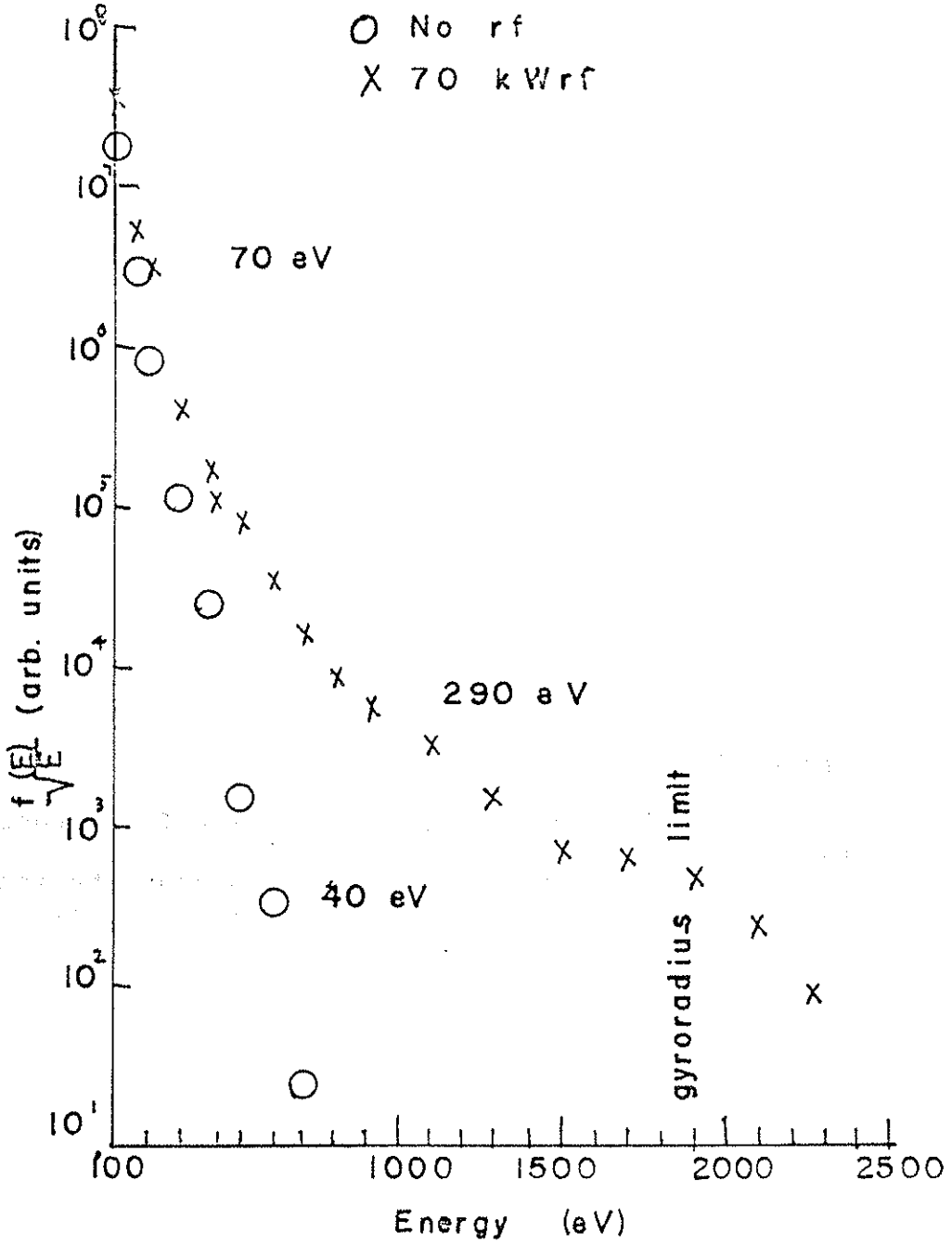
O No rf
X 70 kW rf
70 eV
290 eV
40 eV
gyroradius limit
f(E) (arb. units)
Energy (eV)
100
1000
1500
2000
2500

Figure 6-7.

Cu I radiation vs location of B_t ($W = 2W_{ci}$) resonance zone.
The presence of the ≃ 5 kG fields around the internal rings shifts the location of the resonant $|B| = 4$ kG surface near the copper rings.

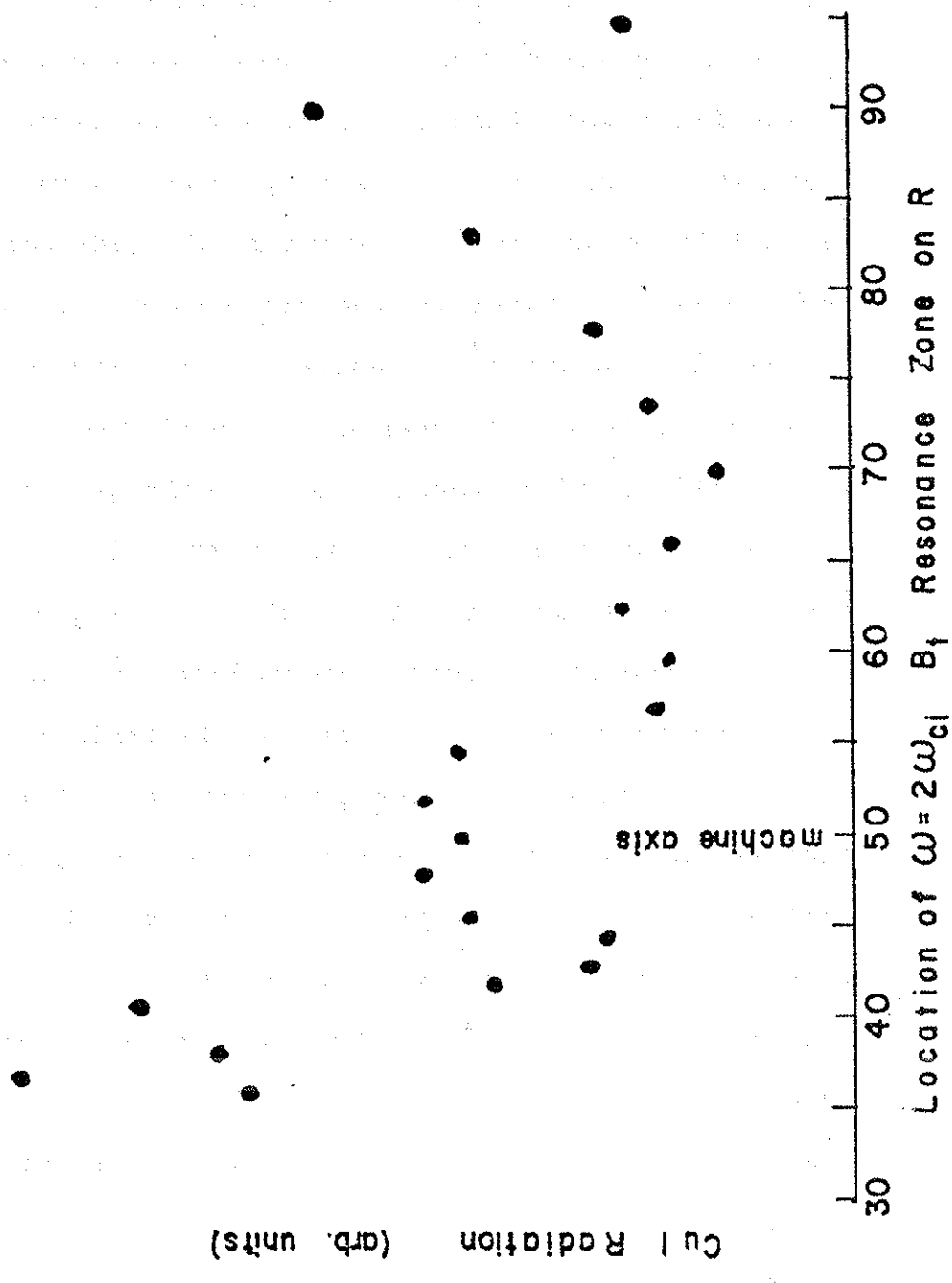
Cu I Radiation (arb. units)
machine axis
30
40
50
60
70
80
90
Location of $\omega = 2\omega_{ci}$ B_t Resonance Zone on R

impacting the hoop. The two largest peaks occur with the resonance zone near the hoops, but the smaller peak in the center is caused by heating of the current channel.

A more detailed result is shown in figures 6-8 and 6-9. The first was obtained by moving the resonance zone by adjusting B_t while holding the plasma current approximately constant. A minimum of 150% of the rf voltage needed to saturate the ion temperature was used. The single data point with negligible heating occurs when there is no cyclotron resonance in the plasma. Figure 6-8 shows a similar plot where the rf voltage was reduced below the saturation point. While this ignores profile effects it does demonstrate that in Tokapole II the attainable temperature was independent of the harmonic used so long as sufficient power is available to overcome coupling inefficiencies. The presence of higher harmonic resonances in a low aspect ratio device will provide some additional heating, though the $W = 2W_{ci}$ term clearly dominates. The $W = W_{ci}$ slow wave resonance is substantially less effective than the higher harmonics as expected.

Since the loading of the antenna is proportional to ϕ^2, it is desirable to place the antenna in the highest rf field region possible. The Mark II antennae were adjustable in spacing from the plasma. Figure 6-10

Figure 6-8.

Maximum ion temperature vs harmonic heating number on axis, high power.

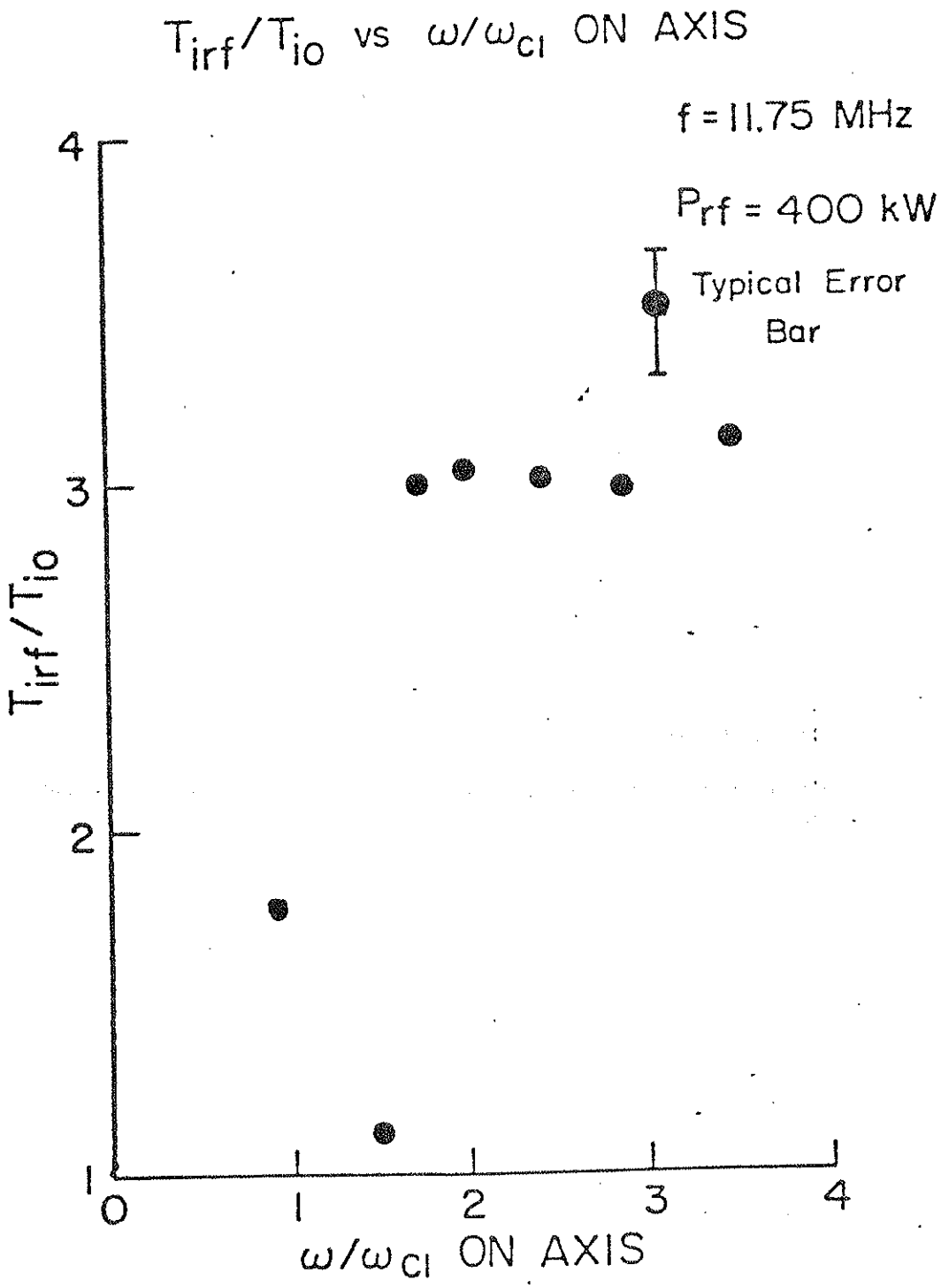
T_{irf}/T_{io} vs ω/ω_{ci} ON AXIS
f = 11.75 MHz
P_{rf} = 400 kW
Typical Error Bar
T_{irf}/T_{io}
ω/ω_{ci} ON AXIS
0
1
2
3
4

Figure 6-9.

Maximum temperature increase vs harmonic number, medium power.
The multiple resonances are shown to indicate which are responsible for heating.

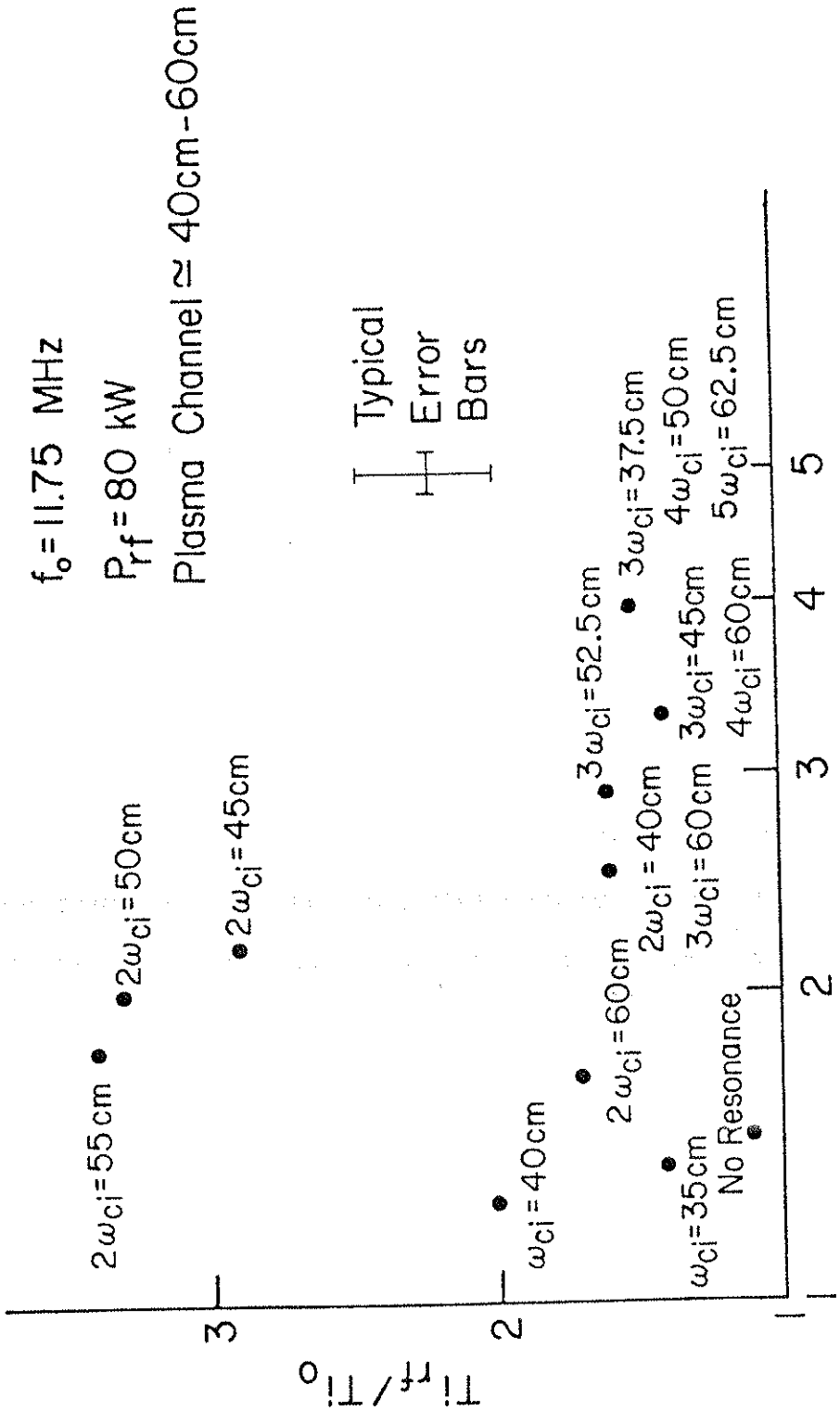
f_o = 11.75 MHz
P_{rf} = 80 kW
Plasma Channel ≅ 40cm-60cm
Typical Error Bars
$T_{i,rf}/T_{i_o}$
ω/ω_{ci} ON AXIS
1
2
3
4
5
$2\omega_{ci}$=55cm
$2\omega_{ci}$=50cm
$2\omega_{ci}$=45cm
ω_{ci}=40cm
$2\omega_{ci}$=60cm
$2\omega_{ci}$=40cm
$3\omega_{ci}$=52.5cm
$3\omega_{ci}$=37.5cm
ω_{ci}=35cm
No Resonance
$3\omega_{ci}$=60cm
$3\omega_{ci}$=45cm
$4\omega_{ci}$=60cm
$4\omega_{ci}$=50cm
$5\omega_{ci}$=62.5cm

Figure 6-10.

Relative heating and coupling vs antenna insertion.

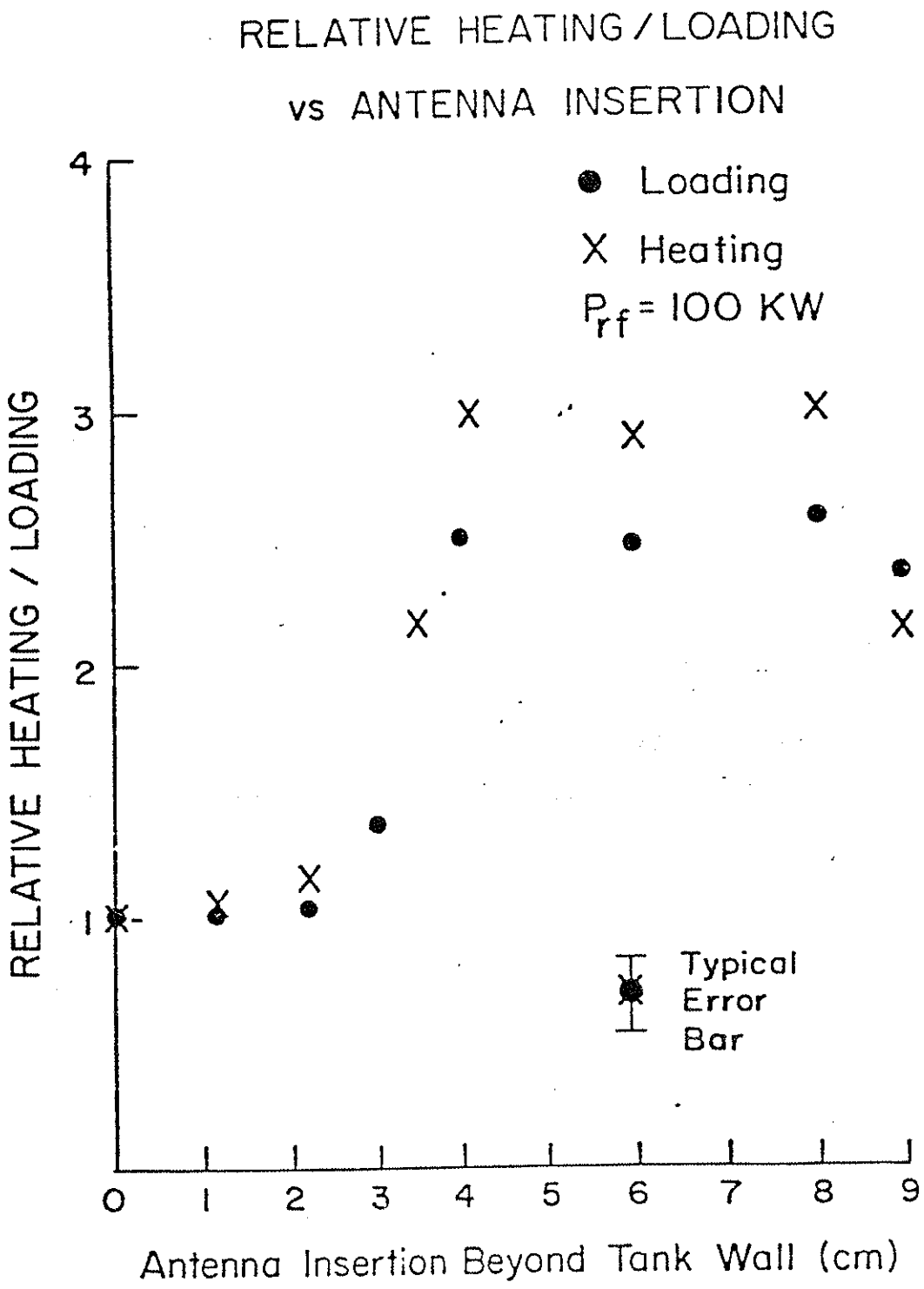
RELATIVE HEATING / LOADING
vs ANTENNA INSERTION
Loading
X Heating
P_{rf} = 100 KW
RELATIVE HEATING / LOADING
4
3
2
1
Typical
Error
Bar
0
1
2
3
4
5
6
7
8
9
Antenna Insertion Beyond Tank Wall (cm)

demonstrates the strong dependence of both the loading resistance and the attainable temperature. The break where the antenna protrudes beyond the separatrix and begins to reduce the central plasma channel is apparent. This problem will be much less severe in a higher density machine where the propagating region extends to the limiter. Figure 6-11 shows the importance of having the launching device perpendicular to the local $k_{||}$.

Tokapole II experienced enhanced reflux and impurities with the application of rf. In the somewhat dirtier machine of May 1979, the rf produced a marked decrease in the amp-secs performance parameter[4]. This termination was still very benign in sharp contrast to the major disruptions precipitated by the rf in the ST tokamak[22]. This effect is due to the enhanced impurities, and it closely parallels the results obtained by deliberate impurity doping achieved by Dexter and Groebner[34]. The much cleaner machine of March 1980 showed only a slight decrease in amp-secs at the highest power available despite several improvements in the rf source (figure 6-12). This edge heating is due in part to the fact that modes with small radial mode numbers have large gradients in E_+ near the edge of the plasma. Also, the m = $+1^*$ mode has a large $|E_+|$ component near the edge of the plasma. Since the profile is hollow at startup when this

Figure 6-11.

Plasma loading vs antenna orientation relative to the local $B_{||}$.

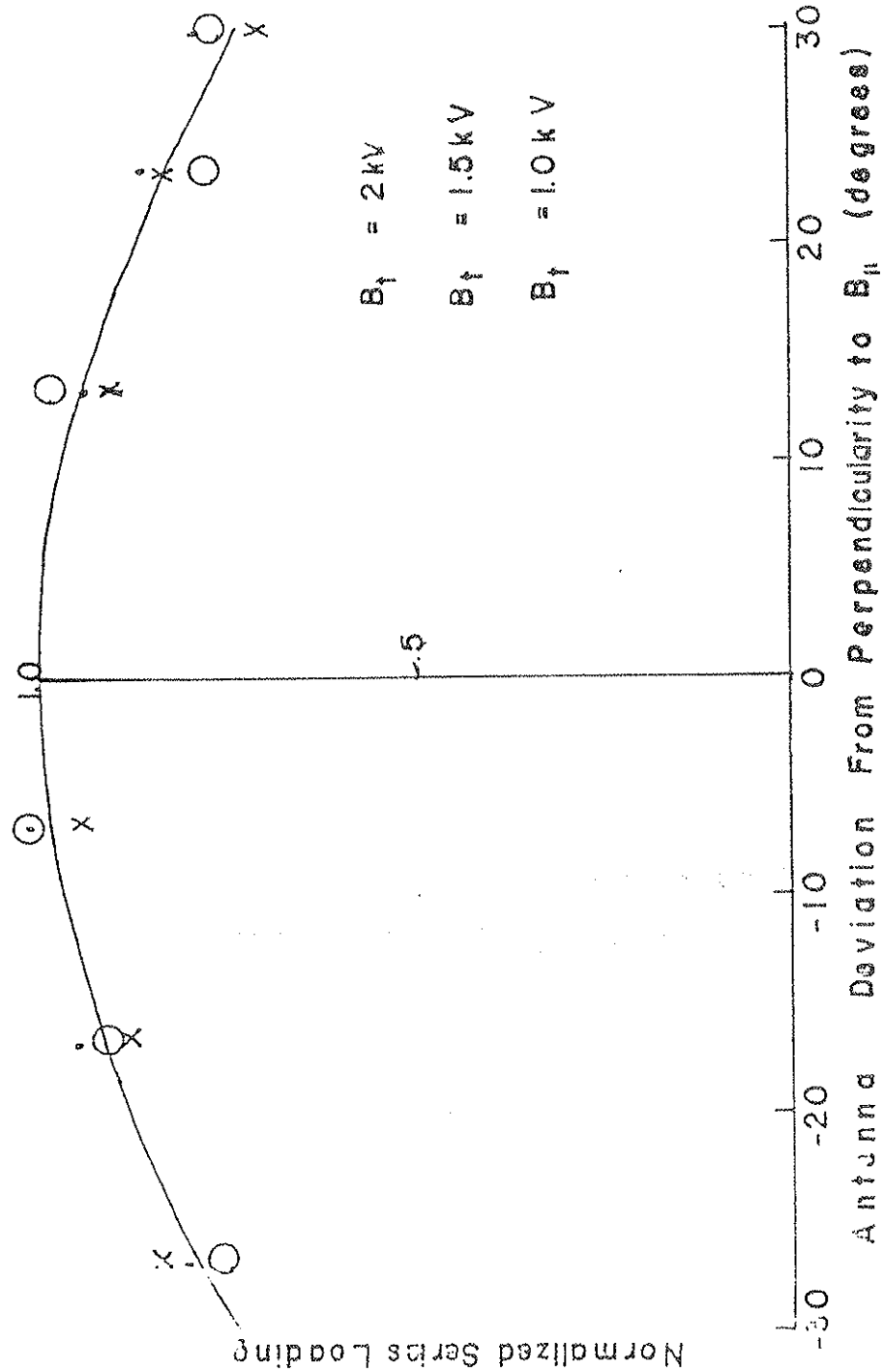
Normalized Series Loading
1.0
.5
0
-30
-20
-10
20
30
Antenna Deviation From Perpendicularity to $B_{\perp}$ (degrees)
$B_{\uparrow}$ = 2 kV
$B_{\uparrow}$ = 1.5 kV
$B_{\uparrow}$ = 1.0 kV

Figure 6-12

Amp-secs vs applied rf voltage.

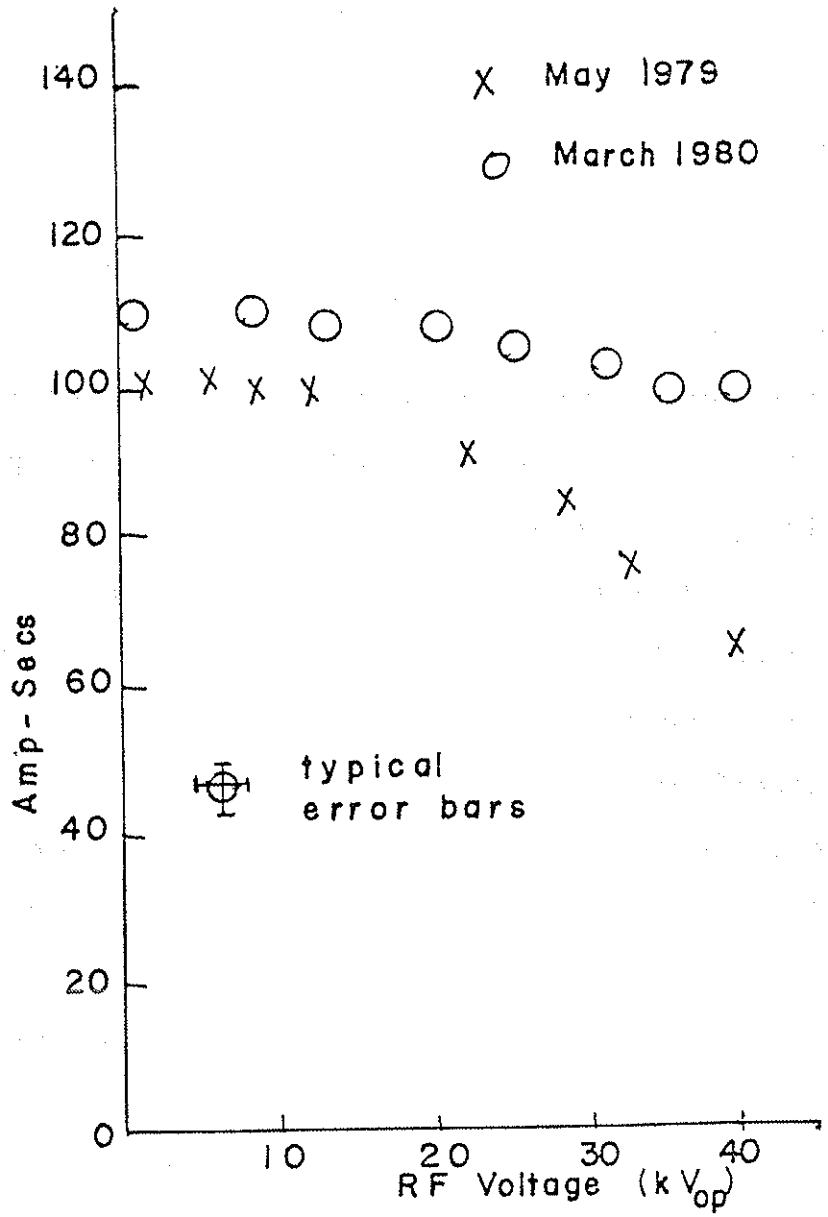
140
120
100
80
60
40
20
0
Amp-Secs
May 1979
March 1980
typical
error bars
10
20
30
40
RF Voltage (k V_{op})

mode propagates, the effect is further magnified. Figure 6-13a shows the enhanced C III radiation as a function of the time the rf is applied.

The largest impurity effect is seen in the Cu I radiation. While all other impurities in the May 1980 machine at most doubled, the Cu I radiation could be increased by more than an order of magnitude (figure 6-13b). While no quantitative calculation could be made, directional measurements indicated the enhancement was isotropic with respect to the four hoops, unlike the ohmic case, and was proportional to the power input. The increase in Cu I radiation was not peaked in the vicinity of the antenna. This demonstrates that the heating was not a near field effect since the antenna has several copper fittings and was located between two lower hoops. This suggests that losses to the hoops may have been a significant loss mechanism for energetic particles.

Theoretically, several mechanisms are expected to cause significant power loss. Low current tokamaks such as ST and ATC[22] have suffered from gyroradius limitations in which particles with large perpendicular energy are too energetic to be confined by the poloidal flux and are lost by impacting the limiter. Kieras has shown[35] that particles above a few hundred eV which are sufficiently collisionless that the bounce frequency is near to or

Figure 6-13.

(a) Enhanced C III radiation vs rf application time.
(b) Enhanced Cu I radiation vs rf application time.

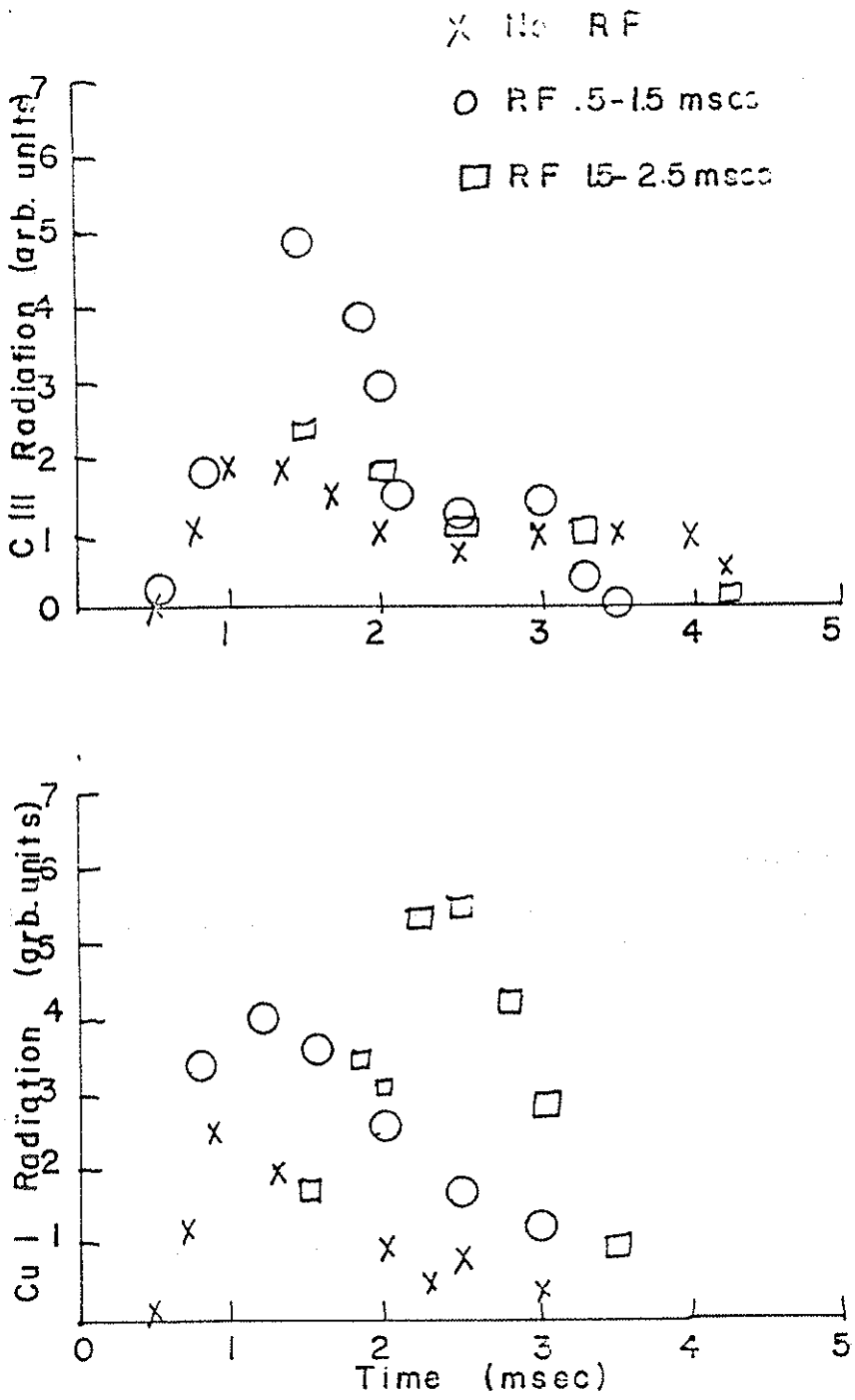
No RF
RF .5-1.5 msec
RF 1.5-2.5 msec
C III Radiation (arb. units)
Cu I Radiation (arb. units)
Time (msec)
0
1
2
3
4
5
6
7

greater than the ion-ion collision frequency are lost primarily to the antenna or depart the current channel.

The truncation of the distribution function (figure 6-6) is not sharp for several reasons. The loss of particles only occurs for counter streaming particles whose banana orbits lie on the outer edge of the current channel. Also, the minimum perpendicular energy at which particles begin to be lost is a continuous function of the minor radius with particles beyond about half the plasma radius being only weekly confined. Also, the charge exchange analyser sees a weighted average of the particles on a cord which is nevertheless peaked at the hot center of the discharge. Finally, the resolution of the charge exchange analyser is $\tilde{-}$ 125 eV at this energy. Figure 6-14 compares the experimental values with the theoretical I_p^2 dependence[35].

The gross energy confinement time for Tokapole II has been established in the past[4] to be approximately 250 usec by assuming equal ion and electron energy confinement times. Because $T_i << T_e$ in the ohmic case the exact number is insensitive to the ion energy confinement time t_i. The charge exchange measurements enabled two different independent measurements of t_i directly. The first technique involved noting that above approximately 400 eV the charge exchange signal was negligible off an

Figure 6-14.

Gyroradius energy limit vs I_p.

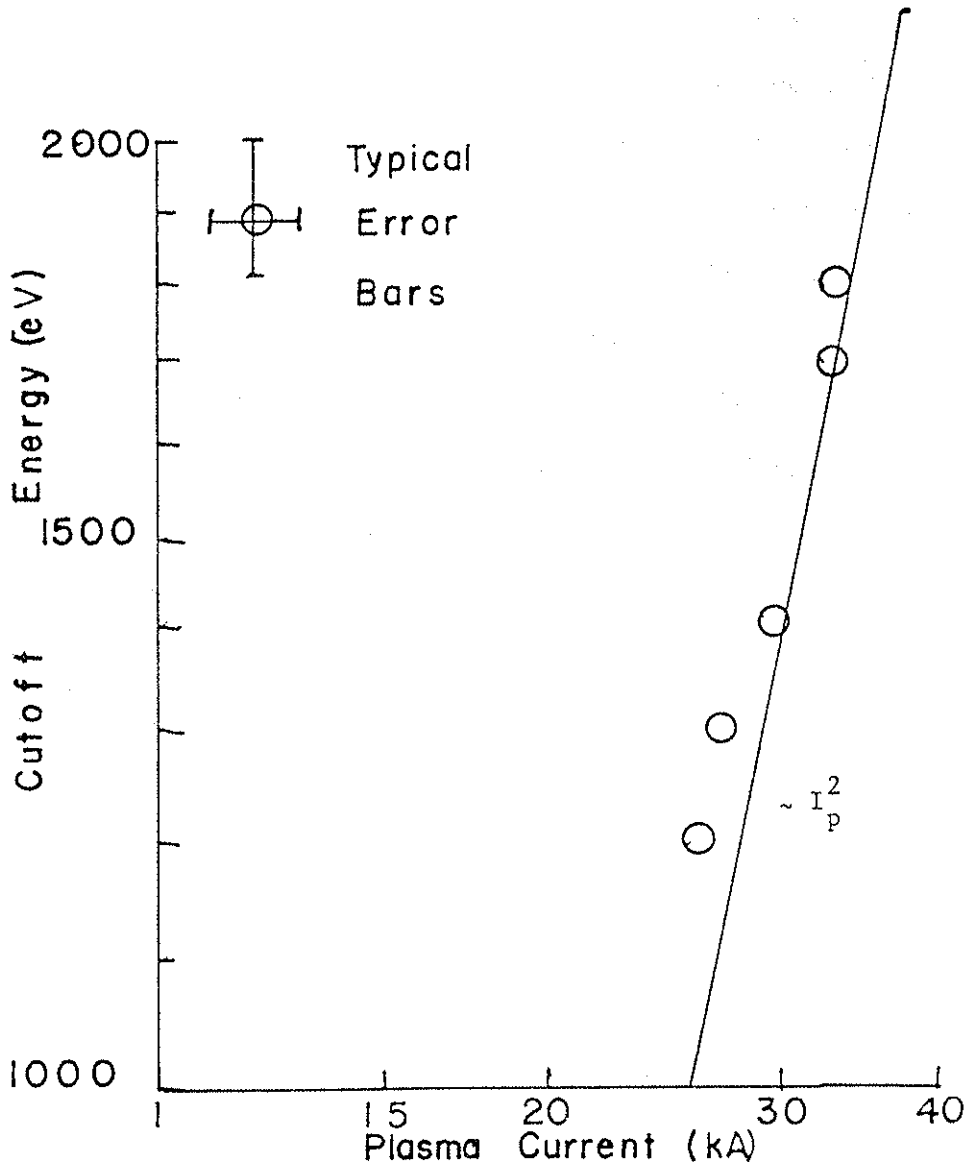
2000
1500
1000
Cutoff Energy (eV)
Typical
Error
Bars
~ I_p^2
1
5
20
30
40
Plasma Current (kA)

eigenmode resonance. Even below 600 eV the signal was still readily apparent above the ohmic heating signal. Since the modes were quite sharp it was possible to assume the heating was abruptly terminated with mode passage and then measure the e-folding time of the charge exchange signal. Any additional heating would make this determination an upper bound on t_i. This loss rate was found for collisionless particles to be proportional to E^{-1}, with the increase in confinement time saturating in the collisional regime (figure 6-15). Secondly, the confinement time could be calculated from the assumption $t_{energy} = U/P$ where U is the stored energy in the ions and P is the ICRF input power. Figure 6-16 gives the bulk energy confinement time of the effective Maxwellian temperature <E> at various plasma currents. The decreasing dependence of t_i on <E> with increasing I_p suggests the gyroradius term loss is progressively less important with increasing current as expected. Assuming the confinement time indicated by saturation in figure 6-15 is the bulk confinement time, the agreement is good between that time and the measured time from figure 6-16 at I_p = 25 kA.

The change in confinement and power input is reflected in the attainable temperature (figure 6-17). Both the body and tail temperatures are effected. By

Figure 6-15.

Particle confinement time vs particle energy.

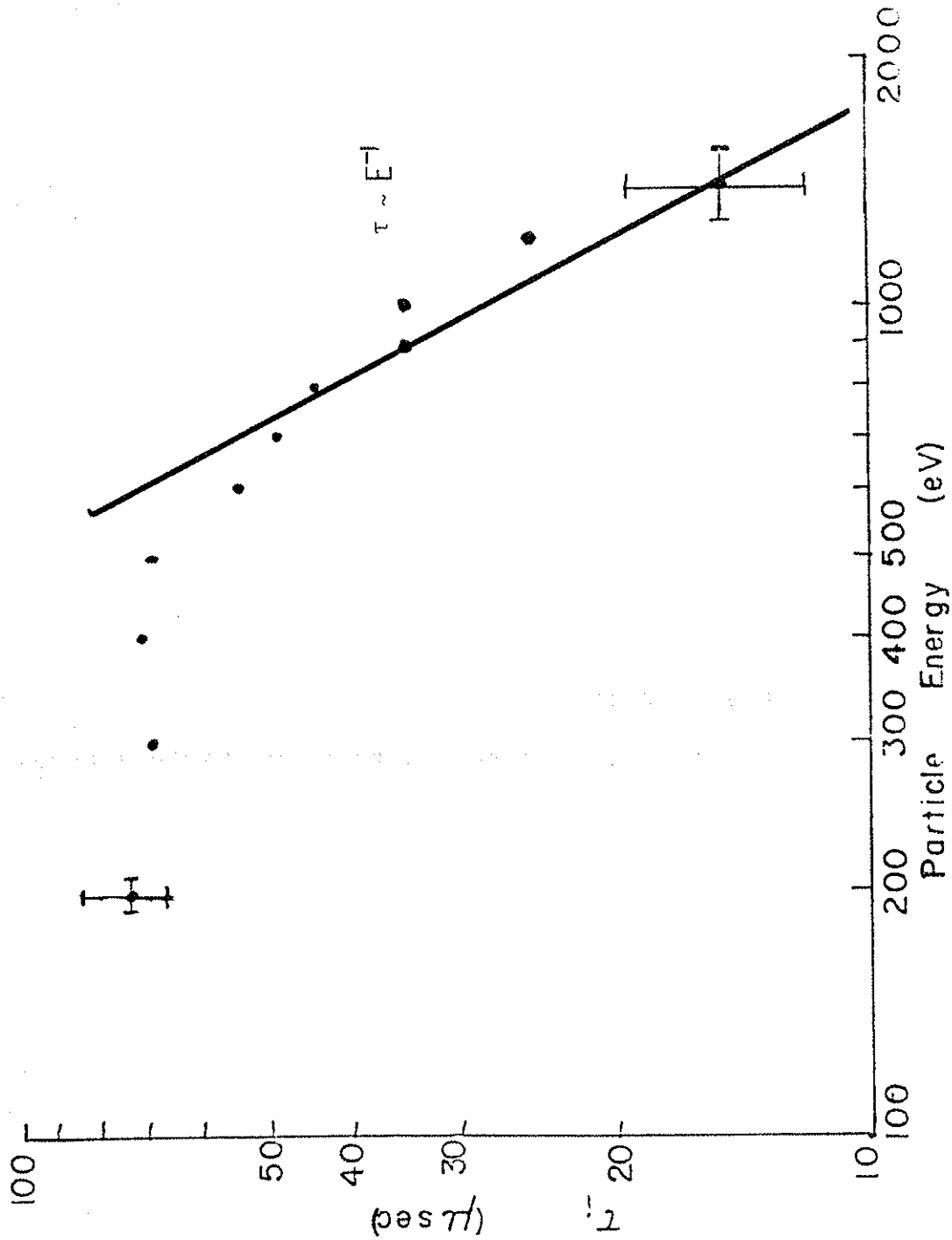
100
50
40
30
20
10
τ_i (μsec)
100
200
300
400
500
1000
2000
Particle Energy (eV)
$\tau \sim E^{-1}$

Figure 6-16.

Ion energy confinement time vs <E>.

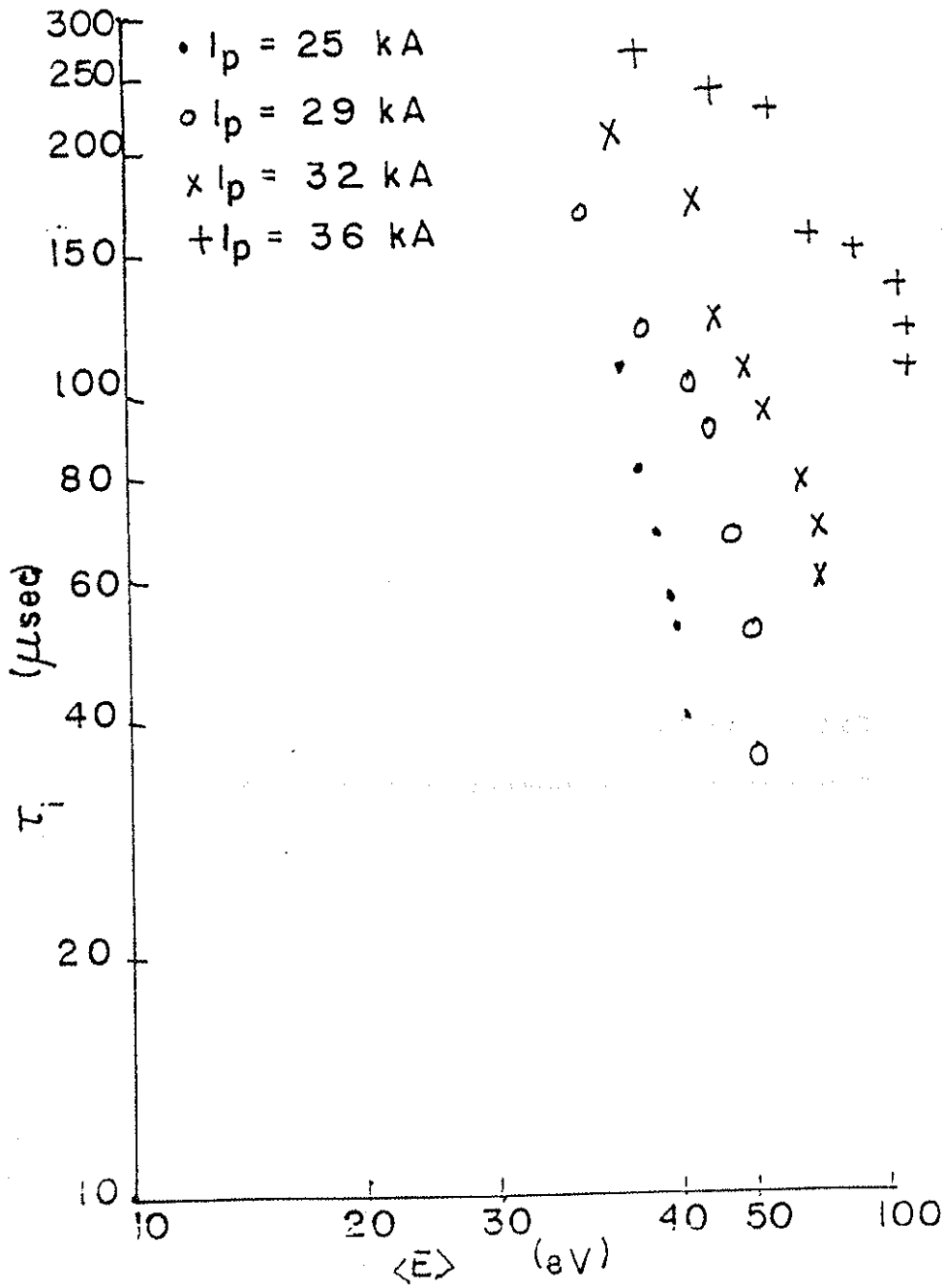
• I_p = 25 kA
o I_p = 29 kA
x I_p = 32 kA
+ I_p = 36 kA
300
250
200
150
100
80
60
40
20
10
τ_i (μsec)
10
20
30
40
50
100
⟨E⟩ (eV)

Figure 6-17.

Increase in ion temperature vs ICRF power.

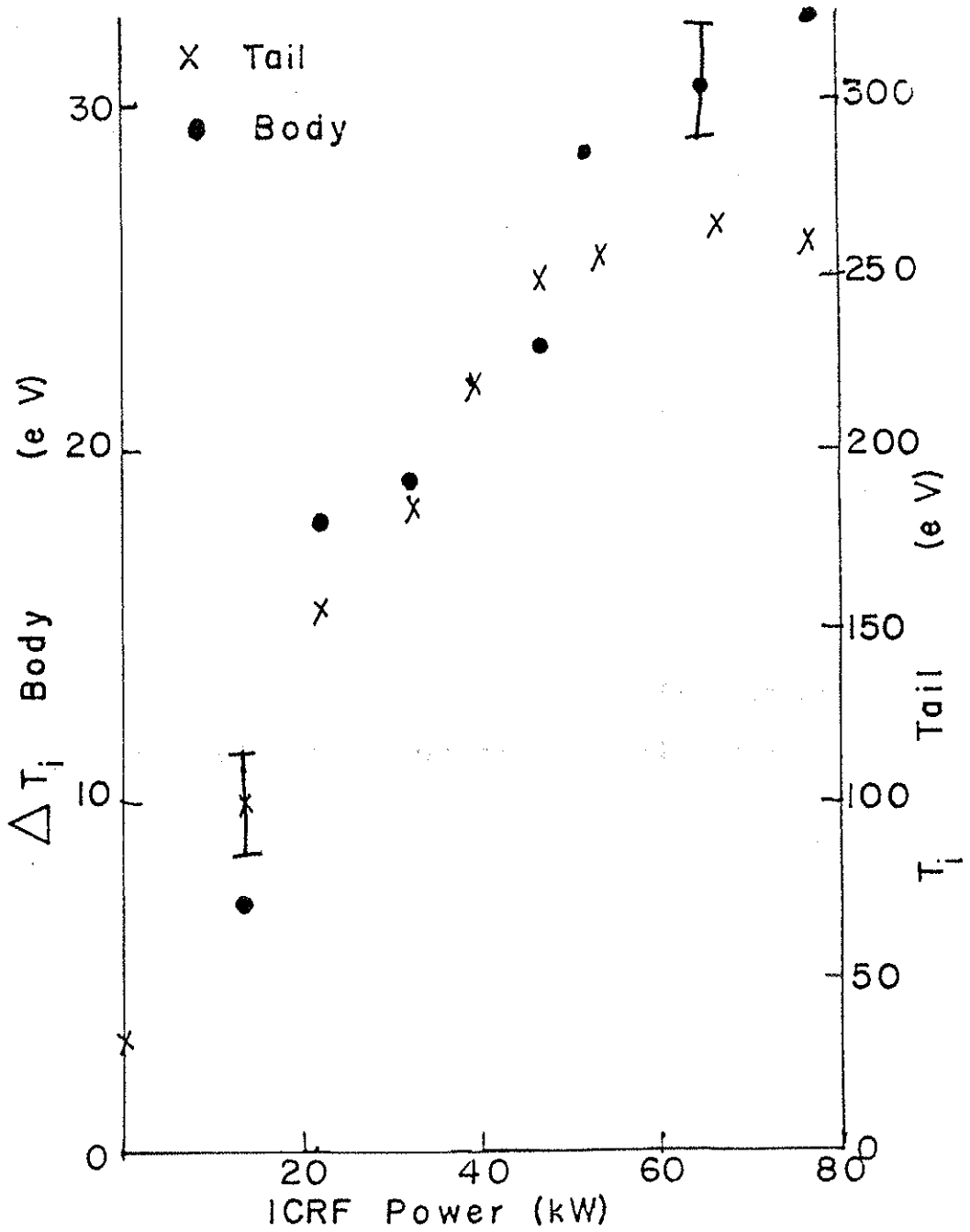
X Tail
Body
30
20
10
0
ΔT_i Body (e V)
300
250
200
150
100
50
0
T_i Tail (e V)
20
40
60
80
ICRF Power (kW)

holding the other parameters approximately constant it was observed that the attainable body temperature was essentially a linear function with negative slope of the filling pressure except where the filling pressure was too low to a form a good discharge (figure 6-18).

We can also examine the ICRF input power and the charge exchange power loss for correlation. The charge exchange losses for figure 6-19 represent a best guess in the absence of detailed profile knowledge but should be better than a factor of 2 in accuracy. One would expect that at low power levels the ohmic input power to the ions would be dominant, while at the highest power the rf input would dominate. The losses should result from the finite gyroradius effects. In the intervening regions, ion thermal conduction and charge exchange losses should dominate. Qualitatively this is observed, especially for the highest plasma current where loss cones should have the least effect. It is tempting to assign the region where the magnitude of the charge exchange and ICRF terms are equal as being dominated by the charge exchange loss. This scenario is very plausible in light of the high neutral density but is probably too simple to be accurate in detail. Detailed transport codes which are accurate in conventional tokamaks indicate no single dominant loss mechanism. The presence of internal rings, the absence of

Figure 6-18.

Maximum ion temperature vs filling pressure.

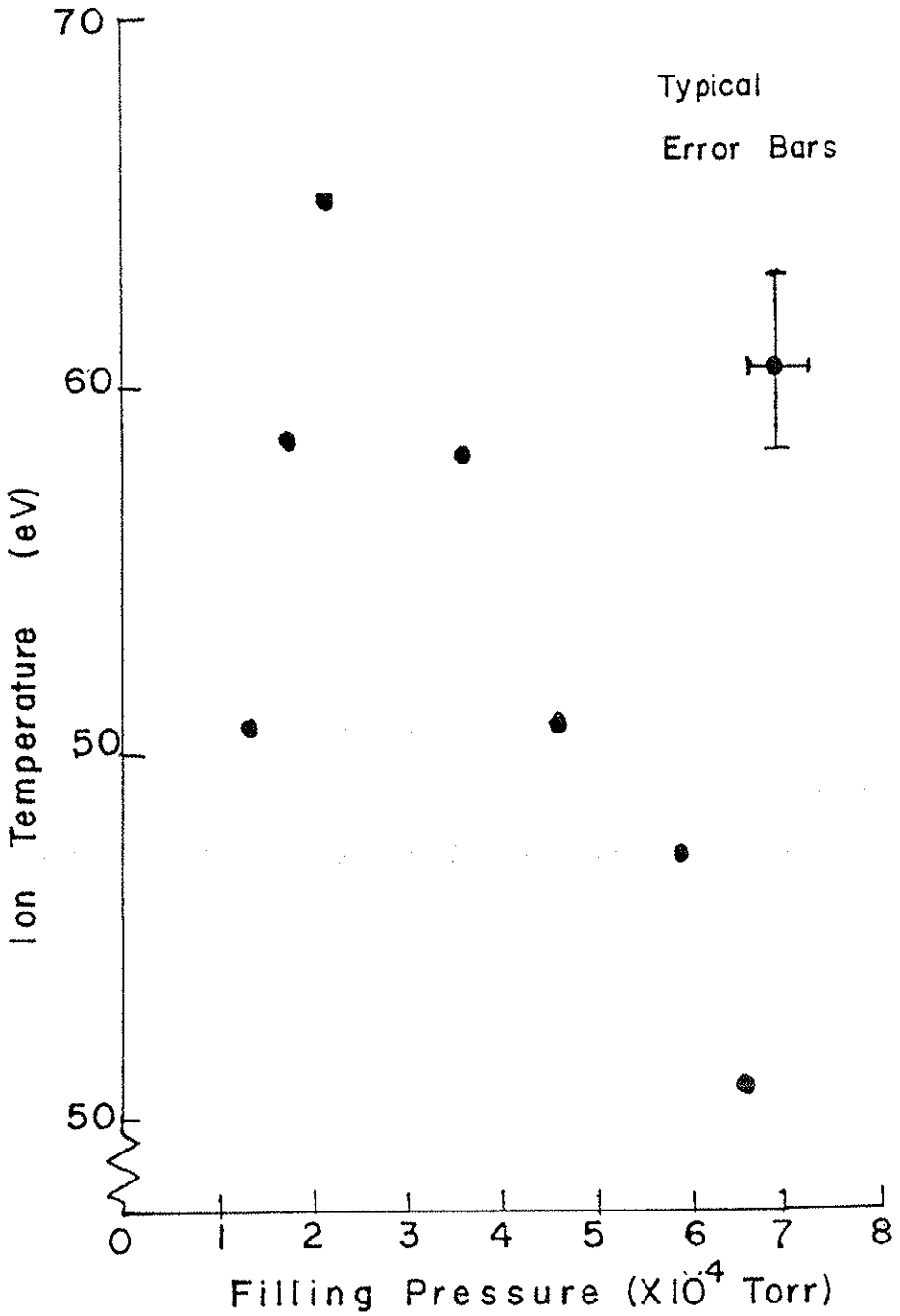
70
60
50
50
Typical
Error Bars
Ion Temperature (eV)
0
1
2
3
4
5
6
7
8
Filling Pressure (X10^4 Torr)

Figure 6-19.

Charge exchange power loss vs ICRF power input.

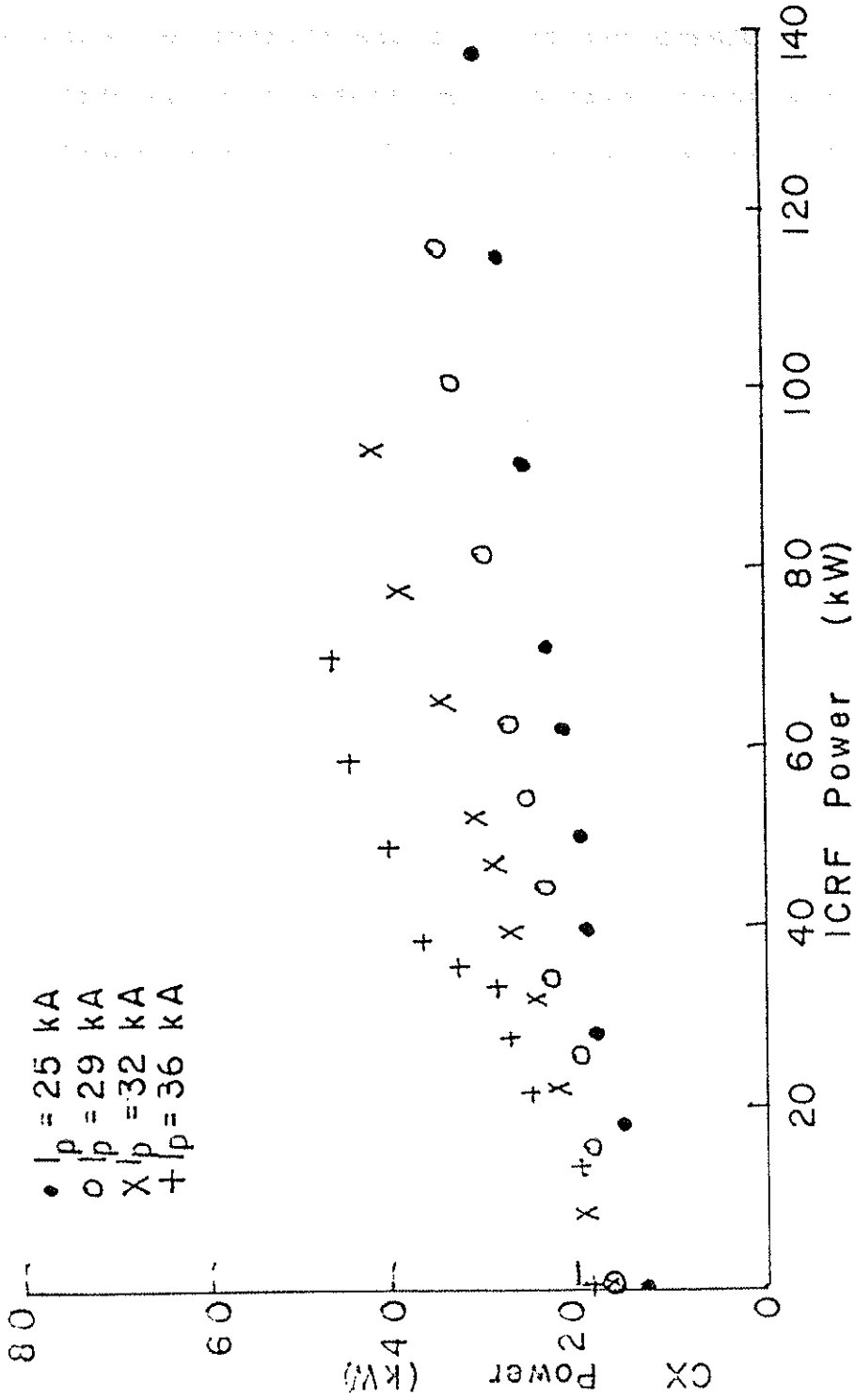
• I_p = 25 kA
o I_p = 29 kA
X I_p = 32 kA
+ I_p = 36 kA
CX Power (kW)
0
20
40
60
80
100
120
140
ICRF Power (kW)

detailed profile data, and the temperature range in which the plasma cannot be characterized as being mainly in one transport regime complicate the quantitative solution beyond the range of this experimental thesis.

VII. POWER FLOW

We are now in a position to make an approximate accounting for the power flow in this experiment (figure 7-1). The highest density and plasma current will be used as representative of the most relevant regime.

It must be explained that while the efficiency of the total rf system is relatively low, this should not be considered a fundamental limitation. The tubes used in the rf source will drive individually a parallel resistance ≃ 22Ø ohms, or collectively ≃ 44Ø ohms in the center tapped push-pull circuit used. Additionally the movable antenna has multiple connections which are purely mechanical, increasing the series resistance. As the available power was ample to saturate the ion temperature, and the total equivalent loading was well above the tube plate resistance, no further effort was made at optimization. Finally, the small antenna required by the hoops and retraction equipment subtends only 3Ø degrees in the poloidal direction and has a relatively flat Fourier spectrum with the $m = Ø, \pm 1$ mode coefficients ≃ .Ø8. Such factors will of course be much less severe in a large device optimized for rf heating. Figure 7-1 lumps all electrostatic and other loading effects identified as being unrelated to cyclotron heating as "parasitic."

Figure 7-1

Power flow for the complete ICRF heating system with Mark IIb antenna.

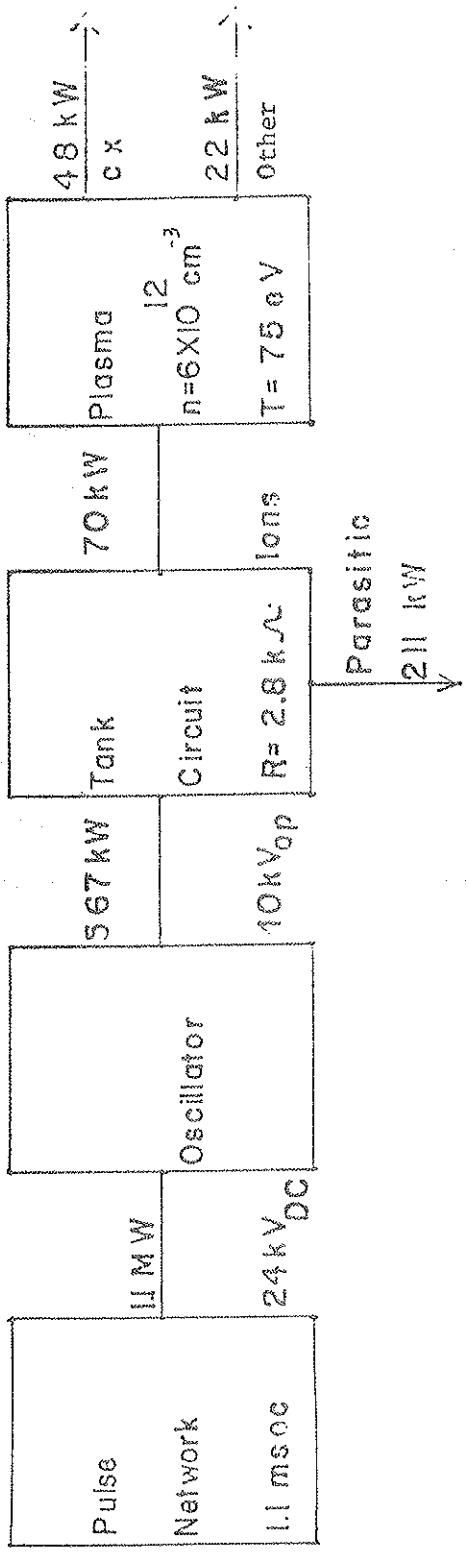
Pulse
Network
1.1 msec
11 MW
24 kV DC
Oscillator
567 kW
10 kV op
Tank
Circuit
R= 2.8 kΩ
70 kW
Ions
Parasitic
211 kW
Plasma
n=6X10 12 cm -3
T= 75 eV
48 kW
cx
22 kW
other

VIII. CONCLUSIONS

We have demonstrated that fast magnetosonic waves propagate well in a four node poloidal divertor device with a large surrounding vacuum blanket. The ion heating theory was tested by comparison of the actual measured power input with the heating calculated from the measured wave amplitude and is in excellent agreement.

Passive mode tracking is effective in increasing the power deposition during eigenmode passage and is in excellent agreement with theory.

While the ion temperature increases initially predicted[36] were not achieved, the ion temperatures have been increased from 35 to 75 eV with tails of 320 eV. The ion temperature limitation is qualitatively in agreement with loss mechanisms due to charge exchange loss and finite-gyro radius effects. The only deleterious effect is a 10% benign decrease in discharge length due to enhanced impurity influx.

REFERENCES

1. S.O. Dean, J.D. Callen, H.P. Furth, T. Ohkawa, P.H. Rutherford, S.C. Burnett, J.B. McBride and N.A. Davies, Status and Objectives of Tokamak Systems For Fusion Research, (WASH 1295, USERDA).

2. T.H. Stix, Nucl. Fusion, 15, 737 (1975).

3. J.C. Sprott, University of Wisconsin, Plasma Physics Studies PLP 744 (1978).

4. R.J. Groebner, Ph.D. Thesis, University of Wisconsin (1979).

5. D.J. Holly, J.C. Sprott, F.D. Witherspoon, University of Wisconsin, Plasma Physics Studies PLP 774 (1978).

6. J.D. Barter, Ph.D. Thesis, University of Wisconsin (1976).

7. J.C. Sprott, University of Wisconsin, Plasma Physics Studies PLP 354* (1977).

8. Signetics Linear Phase Locked Loop Applications Book, Signetics Corporation.

9. Equipe TFR, Nucl. Fusion 18, 647 (1978).

10. J.C. Sprott, University of Wisconsin, Plasma Physics Studies PLP 782 (1979).

11. L. Spitzer, Jr., Physics of Fully Ionized Gases, Interscience Publishers (1962).

12. C.B. Wharton, Cornell University, Laboratory of Plasma Studies, Review of Energetic Neutral Particle Plasma Diagnostics.

13. H.H. Fleischmann and R.G. Tuckfield, Jr., Nucl. Fusion 8, 81 (1968).

14. V.V. Afrosimov, I.P. Gladkowski, Yu. S. Gordev, I.F. Kalinkevich, and N.V. Fedorenko, Sov. Phys.-Tech. Phys., 5, 1378 (1961).

15. H.P. Eubank and T.P. Wilkerson, Rev. Sci. Instrum., 34, 12 (1963).

16. R.A. Breun, Ph.D. Thesis, University of Wisconsin (1975).

17. R.L. Freeman and E.M. Jones, Culham Laboratory, Report CLM-R-137 (1974).

18. C.F. Burnett and J.A. Ray, Nucl. Fusion 12, 65 (1972).

19. T.J. Kruzel, University of Wisconsin, Plasma Physics Studies PLP 840 (1980).

20. T.H. Stix, The Theory of Plasma Waves, McGraw-Hill, Inc. (1962).

21. W. Hooke, Selected Topics in Radio Frequency Heating of Toroidal Plasma, Princeton University (1975).

22. J. Adam, M. Chance, H. Eubank, W. Getty, E. Hinnov, W. Hooke, J. Hosea, F. Jones, E. Perkins, R. Sinclair, J. Sperling, and H. Takahashi, Princeton Plasma Physics Laboratory Report MATT-1094 (1974).

23. J.C. Hosea and R.M. Sinclair, Phys. Fluids 13, 701 (1970).

24. J. Adam and J. Jacquinot, Fontenay-aux-Roses, EUR-CEA-FC-886 (1977).

25. L.C. Woods, J. Fluid Mech. 13, 1570 (1962).

26. F.J. Paoloni, Phys. Fluids, 18, 640 (1975).

27. J.P. Klozenberg, M. McNamara, and P.C. Thonemann, J. Fluid Mech. 21, 545 (1965).

28. W.M. Hooke, J.C. Hosea, F.J. Paoloni, F.W. Perkins, T.H. Stix and H. Takahashi, Princeton Plasma Physics Laboratory Proposal (1976).

29. D.Q. Hwang and R.W. Gould, Phys. Fluids 23, 614 (1980).

30. H. Takahashi, Princeton Plasma Physics Laboratory Report PPPL-1545 (1979).

31. J.E. Scharer, B.P. McVey and T.K. Mau, Nuc. Fusion 15, 297 (1977).

32. K.J. Miller, University of Wisconsin, Plasma Physics Studies PLP 756 (1978).

33. D.J. Holly, D.A. Shepard, S.C. Prager, J.C. Sprott, submitted for publication (1980).

34. R.N. Dexter and R.J. Groebner, University of Wisconsin, Plasma Physics Studies PLP 770 (1978).

35. C.E. Kieras and D.A. Skinner, University of Wisconsin, Plasma Physics Studies PLP 813 (1979).

36. J.C. Sprott, University of Wisconsin, Plasma Physics Studies PLP 753 (1978).

PLP REPORTS

In this thesis, several references are made to internal reports of the University of Wisconsin plasma physics group. These reports are identified by PLP numbers and are available on request from:

Plasma Physics Office
University of Wisconsin
1150 University Avenue
Madison, WI, 53706